UNIVERSITÄT BERN

Multidisciplinary Investigation of Hydrothermal Fluids in the Janggun Zn-Pb Mineralization (South Korea): Mineralogy, Trace Elements, Pb and S Isotopic Compositions

Inaugural dissertation
of the Faculty of Science,
University of Bern

presented by
Jisuk Kang
South Korea

Supervisor of the doctoral thesis:
Prof. Dr. Igor Villa
Institute of Geological Sciences
University of Bern

Multidisciplinary Investigation of Hydrothermal Fluids in the Janggun Zn-Pb Mineralization (South Korea): Mineralogy, Trace Elements, Pb and S Isotopic Compositions

Inaugural dissertation
of the Faculty of Science,
University of Bern

presented by
Jisuk Kang
South Korea

Supervisor of the doctoral thesis:
Prof. Dr. Igor Villa
Institute of Geological Sciences
University of Bern

Accepted by the Faculty of Science.

Bern, 26 March 2021

The Dean

Prof. Dr. Zoltan Balogh

Table of Contents

Chapter 1: General Introduction

1.1. History, Properties, and Uses of Pb and Zn 2

1.1.1. Lead

1.1.2. Zinc

1.2. Types of Pb and Zn source deposits 3

1.2.1. Sediment-hosted deposits

1.2.2. Volcanic-hosted Massive Sulfide deposits

1.2.3. Skarn deposits

1.2.4. Porphyry deposits

1.2.5. Epithermal deposits

1.2.6. Manto deposits

1.3. General geology of South Korea 7

1.3.1. Gyeonggi and Yeongnam massifs

1.3.2. Okcheon metamorphic belt

1.3.2.1. Okcheon basin

1.3.2.2. Taebaeksan basin

1.3.3. Gyeongsang basin

1.3.4. Plutonic activities during the Phanerozoic in South Korea

1.3.5. Distribution of mines for Pb and Zn in South Korea

1.4. Outlines of the thesis 15

Chapter 2: Study of Pb and S isotopic compositions of sulfides from the Janggun deposit in South Korea

2.1. Introduction ……..……..…….. 18

2.1.1. General background of Pb isotopic compositions

2.1.1.1. Decay series of U and Th

2.1.1.2. Isotopic U, Th-Pb methods of dating

2.1.1.3. Common Pb

2.1.2. General background of S isotopic compositions

2.1.2.1. Factors for S Isotope fractionation

2.1.2.2. Processes for S Isotopic variations

2.1.2.3. Geochemical environments for S stable isotopes

2.1.3. Motivation work: Study of Andes (Mondillo et al., 2018)

2.1.3.1. Introduction

2.1.3.2. Materials and Methods

2.1.3.3. Result and Discussion

2.1.3.4. Motivation for the Main Project

2.2. Geological setting …….. 48

2.2.1. Location and Geology of the study area—Janggun mine

2.2.2. Characteristics of Janggun Mine

2.2.1.1. Manganese deposit

2.2.1.2. Vanadium-bearing quartzite deposit

2.2.1.3. Iron deposit

2.2.1.4. Lead-Zinc (-Silver) deposit (study area)

2.3. Samples and analytical methods 54

2.3.1. Sample collection

2.3.2. Microscopy and mineral chemical study

2.3.3. Sample preparation for Pb Isotope analysis

2.3.3.1. Sulfide extraction by micro-drilling on thick sections

2.3.3.2. Resin chromatography

2.3.3.3. MC-ICP-MS

2.3.4. Sample preparation for S isotope analysis

2.4. Results and Discussion 61

2.4.1. Mineralogy

2.4.2. Mineral chemistry

2.4.2.1. Sphalerite

2.4.2.2. Pyrite

2.4.2.3. Galena

2.4.3. Pb isotopic compositions

2.4.3.1. Pb isotopic compositions of samples from the North orebody

2.4.3.2. Comparison between the North orebody and the South A orebody

2.4.3.3. Comparison with literature data

2.4.4. S isotopic compositions

2.5. Conclusions 92

Chapter 3: Study of Pb isotopic compositions and Whole-rock trace element geochemistry of the country rocks from the Janggun deposit in South Korea

3.1. Samples and analytical Methods 95

3.1.1. Sample collection

3.1.2. Sample preparation: Leachate fractions of country rocks

3.1.3. Pb isotope analysis

3.1.4. Trace element analysis

3.2. Results and Discussion 97

3.3.1. Pb isotopic compositions

3.3.2. Trace elements

3.4. Conclusions 106

References 107

List of Figures

Chapter 1: General Introduction

Figure 1.1. Simplified map of South Korea 8

Chapter 2: Study of Lead isotopic composition of sulfides from the Janggun deposit in South Korea

Figure 2.1. Decays of U-Th-Pb 19

Figure 2.2. Location of the study area in Peru 39

Figure 2.3. Geological map of the study area 39

Figure 2.4. Pb isotope correlation diagrams for dolomite samples 41

Figure 2.5. Pb isotope correlation diagrams for sulfide and smithsonite samples 44

Figure 2.6. Pb isotope correlation diagrams for the samples from the CR18 drill core of sulfides and smithsonite at different depths 45

Figure 2.7. Pb isotope correlation diagrams plotted in the Pb evolution model 46

Figure 2.8. Simplified map of South Korea and Geologic map of the Janggun mine with the cross section 48

Figure 2.9. Simplified cross-section of the geology of five Pb-Zn orebodies and magnetite orebody in Janggun mine area 53

Figure 2.10. Underground geological map of the main adit level (591 m) of the North orebody with sampling locations 55

Figure 2.11. Neptune components and functions of each module 58

Figure 2.12. Representative reflected-light photomicrographs 64

Figure 2.13. Underground map of the sampling locations based on the mineral assemblages 66

Figure 2.14. Paragenetic sequence of all sulphide phases 67

Figure 2.15. Element concentrations and ratios in sphalerite and galena 70

Figure 2.16. Histograms of element concentrations in sphalerite, pyrite, and galena 71

Figure 2.17. Pb isotope correlation diagrams for the samples of the North orebody. Symbols highlight different sulfide phases 78

Figure 2.18. Pb isotope correlation diagrams for the samples of the North orebody. Symbols highlight different samples 80

Figure 2.19. Pb isotope correlation diagrams for the samples of the North orebody. Symbols highlight the different mineral assemblages 80

Figure 2.20. Comparison of Pb isotopic compositions between the North and South orebodies analyzed here, and from literature 86

Figure 2.21. Pb isotope correlation diagrams for sulfides from the two orebodies plotted in Pb evolution model 88

Figure 2.22. Sulfur isotopic composition of Janggun sulfides 90

Figure 2.23. Comparison of S and Pb isotopic compositions 92

Chapter 3: Study of Pb isotopic compositions and Whole-rock trace element geochemistry of country rocks of the Janggun deposit in South Korea

Figure 3.1. Results of leaching experiments on country rocks 98

Figure 3.2. Pb isotope correlation diagrams for some country rocks near the Janggun mine …….. 100

Figure 3.3. Correlations between the Pb isotopic composition and selected trace element ratios in the granite leachate-residue pairs …….. 103

List of Tables

Chapter 2: Study of Lead isotopic composition of sulfides from the Janggun deposit in South Korea

Table 2.1. Sample description with the depth of sample collection from cores and the type of samples analyzed in the study 42

Table 2.2. Pb isotopic composition of sulfides, dolomite, and smithsonite from the Cristal mineralisation and Mina Grande deposit 43

Table 2.3. Mineral assemblages of the sample based on the mineral observation collected from the North orebody in the Janggun mine 65

Table 2.4. Electron microprobe analyses of sphalerite, pyrite, galena, arsenopyrite, chalcopyrite, and pyrrhotite 73

Table 2.5. Lead isotopic composition of sulfides from the North and South orebodies 83

Table 2.6. Sulfur isotope composition of pyrite and sphalerite from the North orebody 89

Chapter 3: Study of Pb isotopic compositions and Whole-rock trace element geochemistry of country rocks of the Janggun deposit in South Korea

Table 3.1. Lead isotopic composition of country rocks of the Janggun mine 101

Table 3.2. Chemical compositions of country rock samples 104

Chapter 1

General Introduction

1.1. History, properties, and uses of Pb and Zn

1.1.1. Lead

Lead (Pb, from the Latin word *Plumbum*), an element in group 14 of the periodic table with an atomic number 82 and atomic weight 207.19, is a soft and malleable, greyish or blueish coloured, ductile, and dense metal. Galena (PbS) is a major sulfide mineral (major form in Pb mining), which often contains silver (Ag), and is associated with zinc sulfide (i.e. sphalerite; ZnS). In addition, cerrusite ($PbCO_3$) and anglesite ($PbSO_4$) are principally observed as oxidised minerals. The oxidation states of Pb are generally +2 or +4 and Pb are rarely found free in nature.

Pb has been mined since several millennia (Sinclair, 2009) for a wide range of purposes, and alchemists believe that it is the oldest metal. The properties of Pb, such as high durability, poor conductivity of electricity, absorption of gamma radiation and X-radiation, ease of welding, and resistance to corrosion and heat, make it suitable for several purposes. Because of its chemical resistance, Pb has been widely used in roofing, pipes, and Pb-acid batteries for storing electrical energy, and as covering for electric cables. It is also used in the shielding around nuclear reactors, equipment, and containers of radioactive materials and to block harmful radiation from televisions and screens as it absorbs the short wavelength electromagnetic radiation (Sinclair, 2009; Mudd et al., 2017; Encyclopaedia Britannica).

Since the 1960s, Pb and its compounds have been recognized as toxic for certain applications and to generate cumulative poisoning. Thus, the use of Pb, wherein it is directly exposed to people, such as paint pigments, petrol, insecticides, or other protective devices, has been reduced. In addition, more than 50% of the global demand is met through recycled Pb (UNEP, 2013), making it one of the most recycled metals globally. In particular, more than 90% of Pb-acid storage batteries are recycled.

1.1.2. Zinc

Zinc (Zn), an element in group 12 of the periodic table, with an atomic number 30 and atomic weight 65.39, is a brittle and transitional metal. It is crystalline and bluish- and silver-grey in colour. Zn is a fundamental trace element found in humans (i.e. in red blood cells) and is slightly more abundant than copper (Cu). It is one of the most used non-ferrous metals along with aluminium (Al) and Cu. Sphalerite (Zn blende) is the principal sulfide ore mineral in nature and

often includes trace elements such as cadmium, gallium, germanium, and indium, apart from other oxidised ore minerals such as willemite (Zn_2SiO_4), smithsonite ($ZnCO_3$), and hemimorphite ($Zn_4Si_2O_7(OH)_2H_2O$). Zn mostly exhibits a +2 oxidation state; even though native Zn and compounds of Zn with +1 oxidation state exist, they are rarely observed. Zn compounds with an oxidation state of +3 or higher have not been observed (Encyclopaedia Britannica, n.d.).

Zn has been used since the past two millennia, which is a much shorter period than other common metals, such as alloys like brass (copper and Zn), bronze (copper, tin, and Zn), and nickel silver (copper, nickel, and Zn) (Mudd et al., 2017; Energymining, n.d.). Recently, almost half of the Zn is used in galvanising a wide range of alloys (particularly steel) to protect against corrosion as Zn is more resistant to the atmosphere than iron, which is easily corroded. In addition, Zn compounds are used in various areas such as cosmetics, rubber, medicine, paints, fertiliser, and batteries.

1.2. Types of Pb and Zn source deposits

An ore deposit is defined as any natural mineral or aggregate that is anomalously concentrated and provides economic profit after extraction of the commodity (Robb, 2005). The ore minerals are precipitated through a variety of processes such as igneous, hydrothermal, sedimentary, and surficial processes, and/or by a combination of these processes. I will briefly introduce six types of deposits that are sources of Pb and Zn, including sediment-hosted, volcanogenic massive sulfide, skarn, porphyry, epithermal, and manto (or carbonate-hosted replacement) deposits.

1.2.1. Sediment-hosted deposits

Sediment-hosted deposits, primarily categorised as sedimentary exhalative (SEDEX) deposits and Mississippi Valley-Type (MVT) deposits, are the most dominant sources of Pb and Zn (Mudd et al., 2017). These two types of deposits form at low temperatures and have no genetic relationship with igneous activity, and the ores of both types primarily include sphalerite and galena, with minor quantities of iron sulfide. Generally, Ag is also a common commodity in such deposits, though the concentration of Cu is small (Leach et al., 2010a). However, they have distinct characteristics. The most distinguishable characteristic is that they form in different environments,

corresponding to SEDEX and MVT deposits. SEDEX deposits result from the hydrothermal fluid activity on seafloor venting with extensive replacement processes of pre-existing minerals by secondary minerals. MVT deposits form in the sedimentary basin in the passive margin, which is related to highly selective carbonate replacement by the high salinity basinal or connate fluids (Mudd et al., 2017; Leach et al., 2010b). These different settings lead to differences in the attribute that can be used to further classify them as host rocks, ore textures, and temporal relations. Clastic-dominant sedimentary rocks mainly host SEDEX deposits, whereas carbonate-dominant rocks, such as dolostone and limestone, primarily host MVT deposits (Leach et al., 2010a). In addition, they are distinguishable from the temporal relationship between host rocks and ore formation. Normally, MVT deposits are epigenetic, denoting that the ore deposit formed after its host rock, and SEDEX deposits are characterised as syngenetic, referring to ore deposits that formed concurrently with the host rock as well as with the early diagenetic stage of the sediment host rock (Robb, 2005; Leach et al., 2010b).

1.2.2. Volcanic-hosted Massive Sulfide deposits

Volcanogenic massive sulfide (VMS) deposits are another source of Pb and Zn. These deposits are associated with volcanic-hosted or volcano-sedimentary-hosted and typically occurs as lenses of polymetallic massive sulfides (Galley et al., 2007). VMS deposits form at or near the seafloor through hydrothermal fluid convections, which are hot and enriched in various metals. Even though VMS deposits develop in submarine volcanic environments in a wide range of settings, the depositional environments to contain high concentrations of Pb (Zn is commonly enriched in all types of VMS deposits) are restricted to the settings that are governed by continent-derived sedimentary and volcaniclastic rocks (Franklin et al., 2005). As mentioned in the previous paragraph, the SEDEX deposit is also associated with hydrothermal fluids on seafloor venting, similar to the VMS deposits; however, SEDEX deposit is not immediately associated with volcanism, unlike the VMS deposits. The VMS deposits can be explained by "black smokers" (i.e. hot, metal-enriched, reduced hydrothermal fluids that vent onto the seafloor) in the active volcanism environments along the mid-ocean ridge during the ore-forming processes (Robb, 2005). The fluids involved are derived from seawater, which is cold, oxidising, and metal-poor; these fluids percolate to and circulate in the seafloor basalt rocks by leaching the metals to form

hydrothermal fluids in the environment. As the metals originate from igneous rocks, the variation in metal concentrations among Zn, Pb, and Cu in the subdivision of the VMS family can be explained by the associated rock types (i.e. mafic and felsic) (Pirajno 1992; Franklin, 1993).

1.2.3. Skarn deposits

The term skarn originates from Swedish, meaning very hard rocks which are composed of calc-silicate minerals. Therefore, various calc-silicate minerals (i.e. calcium-rich garnet, epidote, pyroxene, and amphibole) occur in skarn deposits as a result of the metasomatic replacement of carbonate rocks. The deposits form as magmato-hydrothermal fluids (i.e., a variety of types of fluids can be involved) from the interaction of intrusion with the surrounding country rocks (i.e. carbonate rocks) during contact metamorphism and metasomatism (Mudd et al., 2017; Robb, 2005). Skarn deposits are sources of a wide range of metals, depending on the properties of the intrusion. For example, Cu, Pb, Zn, and tungsten (W) skarn deposits are generally associated with oxidising, calc-alkaline, and magnetite-bearing granitic intrusion (called I-type granite), whereas molybdenum (Mo) and tin (Sn) skarn deposits are linked with more differentiated, reduced (called S-type granite), and ilmenite-bearing granite intrusions (Robb, 2005). The deposit forms through the following three processes (Meinert, 1992): two prograde processes, contact metamorphism and metasomatism, and one last retrograde process. The first prograde process includes contact metamorphism (largely a thermal effect) in the early stages of pluton emplacement and crystallisation. No sulfide mineralisation occurs, and hornfelsic textures form at this stage. The second prograde process involves metasomatism and alteration stages. This stage does not involve sulfide mineralisation, as in the previous process, even though elements such silicon (Si), aluminium (Al), and iron (Fe), are introduced into the carbonate rocks by fluids derived from intrusion. Cooling of the intrusion takes place during the retrograde stage. During this stage, the high temperature of magmatic fluids decreases, and shallow meteoric waters are involved in the system. Therefore, retrograde reactions occur and entail sulfide mineralisation (Einaudi et al., 1981; Robb, 2005).

1.2.4. Porphyry deposits

Typically, porphyry deposits are the main sources of Cu, gold (Au), and Mo, rather than Pb and Zn. These deposits are, however, generally linked with the important source deposits of Pb and Zn, such as skarn, manto-type, or epithermal deposits, as the porphyry deposit is associated with intrusive magmatism. The porphyry deposit forms in the environment of magmatic arcs and backarcs at convergent plate margins and above active subduction zones. The host rocks of the porphyry deposit are diverse (i.e. igneous, sedimentary, and metamorphic rocks), even though the lithology type may influence the grade of the deposit, which is generally low to medium and has huge volumes (10–100 km^3) (Sillitoe, 2010). Porphyry intrusion underlies the centre of the deposit and emplaces multiple phases. Earlier porphyries are highly mineralised near the host rocks, whereas later porphyries are less mineralised and are normally barren (Sillitoe, 2010).

1.2.5. Epithermal deposits

Epithermal deposits form at the shallow region compared to the porphyry or skarn systems and are genetically related to these two deposit systems as they are associated with magmatic heat sources and fluids. These deposits are an important source of precious metals such as Au and Ag, apart from being sources of base metals such as Pb, Zn, Cu, As, antimony (Sb), and tin (Sn) (Simmon et al., 2005). Ore minerals in the deposits generally precipitate at < 300 °C and at depths < 1.5 km, indicating that the deposits are defined by the physical conditions of pressure and temperature gradients (Mudd et al., 2017; Simmon et al., 2005). The ores in the epithermal deposits are hosted by volcanic rocks or basement rocks and occur generally in veins of the highest grade and minor fault structures (second- or third-order) than in major faults; they rarely occur in breccias and clastic rocks (Simmon et al., 2005). Many authors have proposed the classification of epithermal deposits based on different criteria such as metal species, sulfide contents, sulfide mineral assemblages, gangue mineral assemblages, and alteration. In particular, the use of gangue minerals is useful in categorising the deposits into two assemblage types (quartz ± calcite ± adularia ± illite and quartz ± alunite ± pyrophyllite ± dickite ± kaolinite), as the sulfide minerals are easily weathered in these environments (Simmon et al., 2005). Generally, low- to intermediate-sulfidation condition in epithermal deposits is most common for Pb and Zn ores (sulfidation: stability of sulfur-bearing minerals in terms of sulfur fugacity).

1.2.6. Manto deposits

Manto deposits (lenses or elongated-tabular or blanket-like deposits) or carbonate-hosted replacement deposits are also important sources of Pb and Zn. Carbonate, limestone, dolostone, or dolomitised limestone host this type of deposit by the intrusion of granite or other intermediate to felsic and porphyritic lithology (Carrasco, 2006_doctoral dissertation). This deposit is characterised by the multi-phase intrusion and is epigenetic. Sillitoe and Bonham (1990) suggested that this type of deposit is related to the base metal skarn deposits and porphyry Cu deposits. The large difference between the skarn deposit and this deposit is the occurrence of calc-silicate minerals. Calc-silicate minerals, which are commonly observed in skarn deposits with sulfide mineralisation, are scarce in the carbonate replacement deposits. The size of this manto deposit is generally smaller than that of VMS or SEDEX, which are huge syngenetic polymetallic deposits. The deposits are characterised by the zonation of ore minerals as well as gangue minerals along the stratigraphic and structural fluid flows (Carrasco, 2006). The Cu-rich zone is centred in the deposit and extends outwards to the Pb-Ag zone, Zn-rich zone, and finally to the Mn zone fringe (Morris and Cox, 1986). Typically, alterations such as dolomitization, silicification, and calcite mineralisation or small amounts of calcic- and ferroan-silicate minerals are observed in the deposits.

1.3. General geology of South Korea

The Korean peninsula is located on the eastern Asian mainland, southeast of China and northeast of Japan. The Korean peninsula has been divided almost in half by the demilitarized zone, which is roughly situated at 38° N and is 250 km long and approximately 4 km wide. The southern part of the peninsula is South Korea, officially called the Republic of Korea, and the northern part is North Korea, officially called the Democratic People's Republic of Korea.

The study area was situated in South Korea. The geology of South Korea is characterised by four major units: the Gyeonggi massif, Okcheon belt, which can be subdivided into the Okcheon basin (or the Okcheon metamorphic belt) and Taebaeksan basin, Yeongnam massif, and Gyeongsang basin, respectively from top to bottom (Fig. 1.1; Reedman and Um, 1975; Chough et al., 2000).

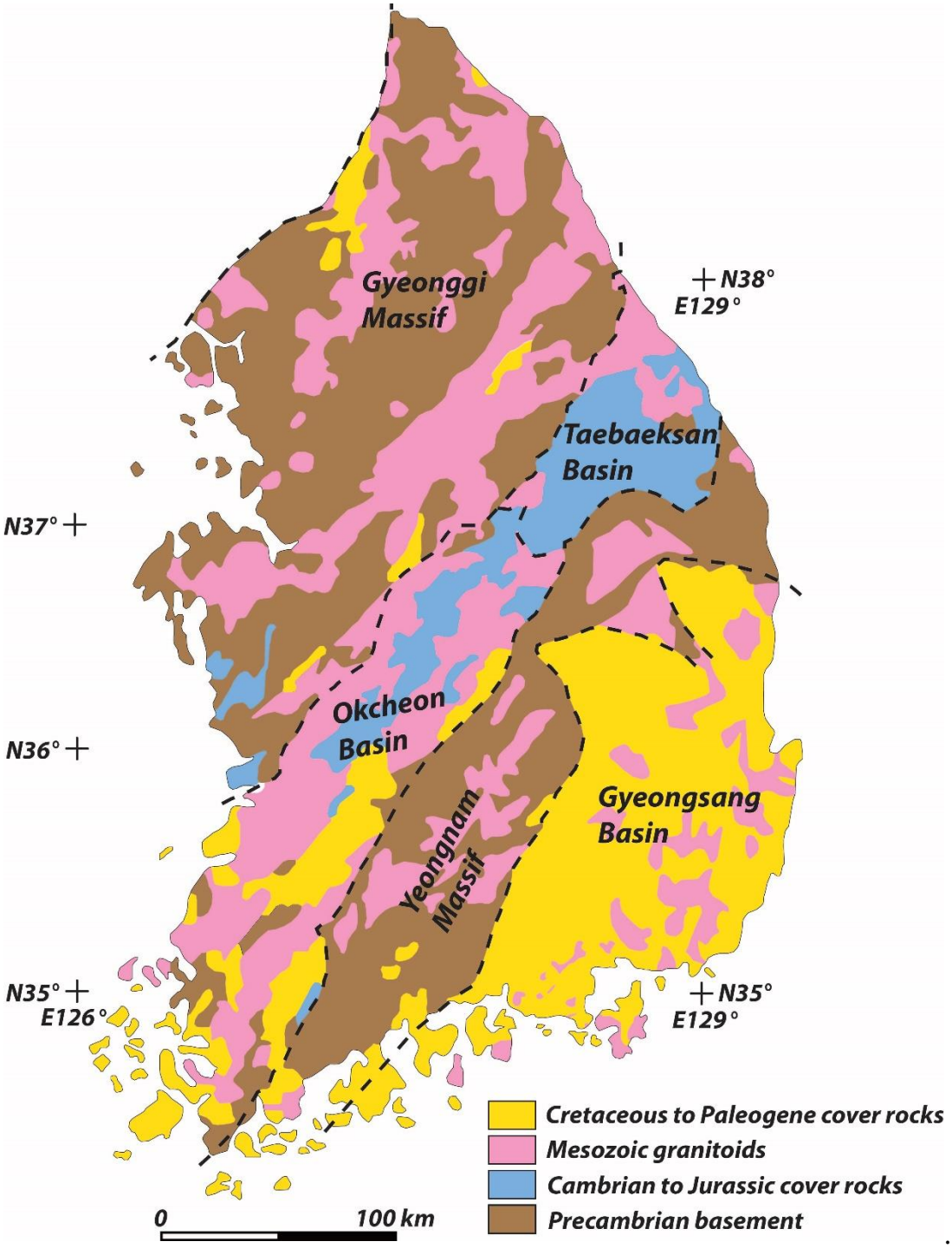

Figure 1.1. Simplified map of South Korea (modified after Jeong et al., 2012), showing the boundaries of four major provinces with the different cover rocks.

1.3.1. Gyeonggi and Yeongnam massifs

The Gyeonggi and Yeongnam massifs are separated by the Okcheon belt, from north to south, and form the basement of South Korea. In particular, the two massifs generally comprise of gneiss and schist complexes of Precambrian age, which experienced moderate to high-grade metamorphism and was exposed extensively due to erosion during the Cenozoic period. In addition, quartzite, interbedded limestone, and extensive intrusions of Mesozoic plutons (which is explained in detail in section 1.3.2.) are observed in both massifs (Hurley et al., 1973; Gaudette and Hurley, 1973; Lee, 1987b; Reedman and Kim, 1997; Chang, 1997).

The origins of both massifs have been widely debated (i.e. whether they are part of the North China Block or the South China Block); recently, it was suggested that the Gyeonggi massif is correlated with the South China Block and not with the North China Block (i.e. an eastern extension of the South China Block), whereas the Yeongnam massif is part of the North China Block. The Yeongnam massif moved to the present position along the NE–SW trending Honam Shear Zone (ductile shearing and trans-current faulting), which is currently located between the Yeongnam massif and the Okcheon Belt, formed by the continuous collision of two massifs during the middle Jurassic period (Reedman and Um, 1975; Cluzel, Cadet and Lapierre, 1990; Cluzel et al., 1991b; Reedman and Kim, 1997; Kwon and Ree, 1997; Choi et al., 2005).

There are several studies on the metamorphic events in these massifs based on radiometric age dating, indicating that at least three major events occurred during the Archean and Proterozoic periods (Kim et al., 2000; Reedman and Kim, 1997). Hurley et al. (1973) reported the Rb-Sr whole-rock isochron age of 2925 Ma from a sample from the Gyeonggi massif, implying that the oldest metamorphic event among the events occurred in South Korea and the rocks of the Archean are present in the Korean peninsula. Dating of the Precambrian gneiss samples from South Korea including by Hurley et al. (1973) and Gaudette and Hurley (1973) suggested occurrence of Sangni Revolution, which is a great metamorphic event at around 2.1–2.0 Ga (the Paleoproterozoic), along with several agreements of other studies (e.g. the Punchon Granite Gneiss, Wonnam Group, and Pyonghae Group) in the Yeongnam massif by Chang (1985) and Hong (1992).

In addition, the ages of granites (e.g. the Hongjesa Granite) that intruded in the Taebaeksan Group (Yuli Group) towards the northeast of the Yeongnam massif were found to be approximately 1.8–1.7 Ga, indicating igneous activity during the Paleoproterozoic (Hong, 1992;

Lee et al., 1992). The rocks of the Mesoproterozoic are irregularly scattered in South Korea, without any evidence of the presence of Neoproterozoic rocks (Chang, 1997).

1.3.2. Okcheon metamorphic belt

The Okcheon belt is further subdivided into two, the Okcheon basin (southwest of the belt) and the Taebaeksan basin (northeast of the belt), based on lithology and metamorphism (Chough et al., 2000). The belt is situated between two massifs (Gyeonggi and Yeongnam) (Fig. 1). Palaeozoic rocks are mostly constrained in this area; the Okcheon Supergroup is distributed in the central part of the Okcheon Metamorphic belt, and the Joseon and Pyeongan Supergroups are distributed in the northeast. In addition, the Late Triassic to Early Jurassic rocks and the Taedong Supergroup are present in the Palaeozoic formations in this belt.

The boundary between the Okcheon and Taebaeksan basins is along a thrust, indicating that the metasedimentary rocks of deeper facies of the Okcheon Supergroup (i.e. Palaeozoic marine sedimentation in an intracratonic rift) were emplaced over the Joseon Supergroup (i.e. shallow marine origin such as shelf and platform environments) by contractional metamorphism during the Middle Palaeozoic (Cluzel et al., 1990; 1991a; Reedman and Kim, 1997). Consequently, both sequences were coevally deposited in different sediment environments.

1.3.2.1. Okcheon basin

The Okcheon basin, situated southwest of the Okcheon metamorphic belt, is primarily composed of the Okcheon Supergroup with a small portion of the Pyeongan Supergroup (this unit mainly occurs in the Taebaksan basin). The Taedong Supergroup is exposed at the margin of the Okcheon basin.

The Okcheon Supergroup consists of a thick sequence of nonfossiliferous and siliciclastic sedimentary rocks and volcanic rocks that originated from low- to medium-grade metamorphic events. The Okcheon Supergroup is divided into roughly 10 formations; however, the ages and relationships among these formations are still uncertain because of the lack availability of fossils in the Okcheon Supergroup (Reedman et al., 1973; Lee, 1987b; Cluzel et al., 1991b). Kwon and Lan (1991), Lee and Chang (1996), Cattel et al. (1984), and Lee et al. (1998a) measured the protolithic age of the Okcheon Supergroup and found that the rocks in the Okcheon Supergroup

are from the Late Precambrian to Palaeozoic and were impacted by a strong metamorphic event during the Mesozoic period.

In particular, the Okcheon Supergroup experienced a few orogeny events that resulted in the folding and thrusting of the sequence. Kim (1987), Cluzel (1991a) and Cluzel et al. (1990) proposed three major orogeny events, the Okcheon orogeny (coeval with the Caledonian orogeny in China), Songrim orogeny (coeval with the Indosinian orogeny in China), and Daebo orogeny, which developed during the Silurian-Devonian, Late Permian-Triassic, and Middle Jurassic-Early Cretaceous, respectively. However, Kim (1996) suggested that the first orogeny in the Korean peninsula is the Songrim orogeny, as there is no clear evidence for the Okcheon orogeny.

The Late Triassic to Early Jurassic rocks of the Taedong Supergroup are composed of non-marine sediments (siliciclastic and lacustrine deposits) with abundant plant fossils located at the margin of the Okcheon basin (Chough et al., 2000; Reedman and Kim, 1997). This supergroup represents the greatest crustal movement in South Korea and is subsequently followed by extensive granite (called Daebo Granite).

Several researchers have attempted to correlate these orogeny events with plate tectonics in South Korea. The Songrim orogeny occurred as a result of two continents colliding between the North China block (with Yeongnam massif) and the South China block (with Gyeonggi massif), whereas the Daebo orogeny events occurred as the paleo-Pacific Plate was subducted north-westwards beneath the Asian continent, forming the Honam Shear zone (Maruyama et al., 1997). The Honam Shear zone, which is a dextral ductile shearing associated with thrusting and folding, occurred as a result of the Daebo orogeny. The Honam Shear zone is accompanied by NE- to NNE-striking thrusts, likely resulting from convergent wrenching in the Okcheon metamorphic belt (Cluzel et al., 1991b; Chough et al., 2000).

Through the Daebo orogeny event, the granitoid rocks were emplaced in the basin at around 10–15 km depth with no volcanic activity, suggesting that the granitoid rocks are the remnants of the old magmatic arc of the Daebo orogeny caused by the erosion of the surface (Oh et al., 1997). Around the Jurassic period (ca. 180 Ma), the Korean peninsula developed into its present shape. Through these events, the Okcheon basin structurally resulted in a NE striking belt, approximately 50 km wide and 300 km long (Reedman et al., 1973; Reedman and Kim, 1997; Cluzel et al., 1990).

1.3.2.2. Taebaeksan basin

The Taebaeksan basin is situated northeast of the Okcheon metamorphic belt and consists of fossiliferous and less deformed sedimentary rocks (Joseon and Pyeongan Supergroups) of the Palaeozoic to early Mesozoic. In addition, the rocks of the Mesozoic (Taedong Supergroup) occur in the mid-western Taebaeksan basin.

The Lower–Palaeozoic Joseon Supergroup unconformably overlies the Precambrian gneiss and metasedimentary rocks of the Yeongnam massif and is composed of five groups. Of these, only two groups, the Taebaek Group (to the east) and the Yeongwol Group (to the west), commonly occur in the Taebaeksan basin and have more abundant occurrences of fossils than the other three groups (Kobayashi, 1966; Chough et al., 2000). In addition, even though this supergroup originated from the sedimentary rocks, which were deposited in the shallow siliciclastic systems, sedimentation environments progressively changed from east to west of the Joseon Supergroup (i.e. to the deeper seafloor in the western Yeongwol) with varying lithology characteristics among the groups (Chough et al., 2000).

As Silurian and Devonian sedimentary rocks are not present (or not observed) in South Korea, the Pyeongan Supergroup overlies the Joseon Supergroup unconformably, indicating that the absence of sedimentary rocks between the Middle Palaeozoic period corresponds to the North-China Block (Reedman and Kim, 1997; Chough et al., 2000). The Pyeongan Supergroup comprises the Late Carboniferous to Triassic (?) sedimentary rocks and is largely distributed in the Taebaeksan basin, with much less occurrence in the Okcheon basin. The types of sedimentary rocks in the Pyeongan Supergroup predominantly include sandstone and shale with small concentrations of conglomerate, limestone, and coal, and primarily consists of four units based on distinct lithologies. Cheong (1969) and Lee (1992) proposed that the thick sequence of the sedimentary rocks in the Pyeongan Supergroup has been deposited in different environments, starting from a marginal marine environment during the Middle Carboniferous to the non-marine sequences in the Permian.

The Taedong Supergroup in the Taebaeksan basin consists of non-marine deposits, as explained above, and occurs in the syn-orogenic thrust belt corresponding to the Daebo orogeny (Chough et al., 2000).

The Taebaeksan basin has been impacted by four major events: the NE-trending ductile shear zone between the Yeongnam massif and the Early Palaeozoic formations in a reversed direction of slip (Kim and Kee, 1991; Kim, 1994; Kim et al., 1994); the Second orogeny (Songrim); the third orogeny (Daebo; described in section 1.3.2.1); and the final deformation (Bulguksa) event that occurred during the Late Cretaceous to Early Tertiary (Kim et al., 1994).

The accurate age of the first event between the Precambrian massif and the early Palaeozoic formations has not been revealed, and this orogeny mostly generated strike-slip shearing rather than thrusting activity (Kwon et al., 1995a). The last deformation, the Bulguksa orogeny, occurred as a result of the continuation of the oblique subduction of the paleo-Pacific Plate, i.e. continuation of the subduction that caused the Daebo orogeny during the Early to Late Jurassic (Kim et al., 1994). The Bulguksa granitoids are subvolcanic magmatic bodies which generally have miarolitic, porphyritic, and micrographic textures and belong to the oxidising magnetite-series rocks (Chang et al., 1990; Park and Park, 1990; Choi et al., 2005). The Daebo and Bulguksa orogeny events deformed and intruded or extruded (Bulguksan magmatism: both volcanism and subvolcanism) into all presented rocks such as the Precambrian Gyeonggi and Yeongnam massifs.

1.3.3. Gyeongsang basin

After the Daebo Orogeny event, the Gyeongsang basin was developed at the southernmost (or southeast) part of South Korea. Because of the northward subduction of the paleo-Pacific Plate (or the Izanagi Plate) beneath the Eurasian Plate, NE-trending fault systems developed in the left-lateral wrenching and the non-marine sedimentary sequence (consisting various fossils such as molluscs, plants, and dinosaur and bird tracks). In addition, the Gyeongsang basin was developed with a series of small basins (e.g. Kongju and Kwangju) in these fault systems (Chun and Chough, 1992; Yang, 1982; Chough et al., 2000). The fault systems are related to an extensional crustal condition that led to extensive volcanic activities in arc platform and backarc settings. Sedimentation of the basins occurred from the Early Cretaceous and continued until the mid-Cretaceous (i.e. before the Bulguksa orogeny) (Chough et al., 2000).

The Gyeongsang basin consists of a thick sequence of sedimentary rocks, called the Gyeongsang Supergroup, and is located in shallow and temporary reservoir/swamp environments (Reedman and Kim, 1997; Chough et al., 2000). This sequence is composed of three groups,

Shindong, Hayang, and Yucheon (chronologically ordered), and represents the sediments of the basin derived from alluvial fan, fluvial, flood-plain, and lacustrine environments (Reedman and Kim, 1997). In particular, the uppermost group, the Yucheon group, principally contains volcanic rocks with volcanogenic pyroclastic sediments and flows overlying the sequences of the Early Cretaceous non-marine sediments, which are caused by episodic volcanic activities corresponding to the Bulguksa orogeny event in the Late Cretaceous to Early Tertiary periods (Reedman et al., 1989). Ooids, stromatolites, and rhizoliths were observed, suggesting that the environment of the basin is a saline lake (Chang et al. 1990; Woo et al., 1991; Paik an Chun, 1993).

1.3.4. Plutonic activities during the Phanerozoic in South Korea

As mentioned in this chapter, several orogenic events have occurred in the Korean peninsula. Thus, plutonic rocks, including dominant granitoid rocks rather than mafic rocks, are commonly observed in South Korea and occupy approximately more than 30% of the entire rocks in South Korea (Chough et al., 2000). In particular, a trimodal distribution of Mesozoic granitoid rocks, such as the Songrim granite (Triassic), Daebo (Jurassic), and Bulguksa (Cretaceous) events, are abundant in South Korea. Additionally, the granitoid rocks from the Bulguksa event mostly intruded the Gyeongsang sedimentary rocks, whereas other granitoids were exclusively distributed in the other provinces (i.e. Gyeonggi massif, Okcheon metamorphic belt, and Yeongnam massif) (Choi et al., 2005).

During the Cenozoic period, minor sedimentation occurred along the coastal areas of the Korean Peninsula. A major NNE-fault system (i.e. the Yangsan Fault) was activated with a dextral displacement in the eastern Gyeongsang basin, which caused the initiation of the opening of the East Sea back-arc basin with small fault-controlled basins at the east margin of the Korean Peninsula (Reedman and Kim, 1997).

During the Quaternary period, volcanism and erosion actively occurred. The volcanic Jeju island with the Halla Mountain (approximately 1950 m above sea level), formed by the alkaline basaltic magma (Lee, 1982), primarily comprises basaltic lava and minor pyroclastic rocks. The volcanic activity was active until around 1000 years ago. The Ulleung Island, formed in the deep marine setting of the East Sea, is located 140 km away from the eastern Korean mainland. It

comprises the Pleistocene volcano (Tomita, 1967), alkaline basalts flows, and trachytic lava (Reedman and Kim, 1997).

1.3.5. Distribution of mines for Pb and Zn in South Korea

In South Korea, there are around 60 mines that have now been abandoned after gaining profits from Pb and Zn mining. The mines are distributed across the country. However, more than half of the mines are concentrated in the Taebaeksan mineralised province located in the Taebaeksan basin, which has accounted for approximately 90% of the gross production of Pb and Zn in South Korea since 1994 (Lee et al., 2007; Lee, 2015). In addition, some of the Pb-Zn mines are located in the Jecheon-Hwanggangri metallogenic region, Gyeongsangbuk-do, and Gyeonggi-do in South Korea. The diverse types of Pb-Zn deposits in South Korea are mostly classified as skarn, hydrothermal-replacement, fissure-filling, or vein-breccia deposits. Generally, large-scale deposits for Pb-Zn are primarily either skarn or hydrothermal replacement types, which are hosted in carbonate rocks and associated with magmatism during the Mesozoic period (Jeong et al., 2012; Lee, 2015).

In particular, the Taebaeksan metallogenic belt, a key province enriched in various metals (e.g. Zn, Pb, W, Fe, Cu, Mo, Ag, and Au) in South Korea, comprises of the Precambrian gneiss and schist basement (the Yeongnam massif), the sequence of Palaeozoic sedimentary rocks (Joseon Supergroup: the Cambrian-Ordovician and Pyeongan Supergroup: the Middle Carboniferous-Early Triassic), and several subvolcanic rocks aged mostly between the Late Cretaceous and Early Palaeogene, corresponding to the Bulguksa magmatism (ca. 50–110 Ma) caused by the north-westward subduction of the paleo-Pacific Plate (Cheong, 1969; Lee, 1987a; Park et al., 1988; Lee et al., 1996b; Maruyama et al., 1997; Jeong et al., 2012). The spatial proximity to a magmatic source could have caused the deposition of different metals in the polymetallic systems, based on the cooling path, which changed the sulfidation state (Choi et al., 2005; 2009).

1.4. Outline of the thesis

Chapter 2: Study of Pb and S isotopic compositions of sulfides from the Janggun deposit in South Korea.

This chapter describes the ore-forming processes in the Janggun Pb-Zn deposit by measuring the Pb and S isotopic compositions of ore minerals (galena, sphalerite, pyrite, pyrrhotite, arsenopyrite, and chalcopyrite). This chapter was published in Ore Geology Reviews, 122, Kang, J., Wille, M., Hofmann, B. A., Strauss, H., & Villa, I. M., Heterogeneous lead isotopic compositions of sulfide minerals from a hydrothermal replacement deposit (Janggun mine, South Korea), 103527, Copyright Elsevier (2020).

Chapter 3: Study of Pb isotopic compositions and whole-rock trace element geochemistry of country rocks from the Janggun deposit in South Korea

This chapter describes the characteristics of Pb isotopic compositions of country rocks with trace element geochemistry. The relationships between Pb isotopic composition and trace elements are also presented in this chapter. This chapter was published in Ore Geology Reviews, 122, Kang, J., Wille, M., Hofmann, B. A., Strauss, H., & Villa, I. M., Heterogeneous lead isotopic compositions of sulfide minerals from a hydrothermal replacement deposit (Janggun mine, South Korea), 103527, Copyright Elsevier (2020).

Chapter 2

Study of Pb and S isotopic compositions of sulfides from the Janggun deposit in South Korea

2.1. Introduction

2.1.1. General background of Pb isotopic compositions

Pb is the 82nd element in the periodic table and has four stable isotopes: ^{204}Pb, ^{206}Pb, ^{207}Pb, and ^{208}Pb. The whole ^{204}Pb is primordial nuclide, i.e. it has no long-lived radioactive parent, whereas the other three isotopes, ^{206}Pb, ^{207}Pb, and ^{208}Pb, are radiogenic nuclides resulting from the radioactive decay of two isotopes of uranium (U) and one isotope of thorium (Th) (^{238}U, ^{235}U, and ^{232}Th, respectively).

2.1.1.1. Decay series of U and Th

Uranium (atomic number, Z, is 92) and thorium (Z = 90) are members of the actinide series of elements, which includes atomic numbers from 89 to 103, mostly corresponding to the filling of the 5f electron shell and characterised by their high diversity in oxidation numbers and radioactivity. In particular, the chemical properties of U and Th are similar because of their similar electron configurations, as they both occur in the tetravalent oxidation state in nature with similar radii (U^{4+} = 1.05 Å, Th^{+4} = 1.10 Å); this implies that they can substitute each other. U behaves differently from Th under oxidising conditions as U forms uranyl ion (UO_2^{+2}), which is soluble with a valency of +6, causing U to be mobile, unlike Th that has a valency of +4 and is insoluble in water. Concentrations of both elements are low in common silicate minerals (a few ppm or less). However, these elements are primarily concentrated in certain accessory minerals (e.g. uraninite, zircon, monazite, sphene, etc.) as either major or minor constituents that replace the other elements.

Three naturally occurring isotopes of U, including ^{238}U, ^{235}U, and ^{234}U, are present, whereas only one isotope of Th, ^{232}Th, primarily exists. These are all radioactive isotopes. In particular, three isotopes (^{238}U, ^{235}U, and ^{232}Th) produce three Pb isotopes (^{206}Pb, ^{207}Pb, and ^{208}Pb) through radioactive chain reactions rather than a single direct decay reaction, i.e. ^{238}U, ^{235}U, and ^{232}Th decay into new radioactive elements, which again decay to form radioactive elements; this process continues until ^{206}Pb, ^{207}Pb, and ^{208}Pb are formed. As the intermediate elements are unstable and short-lived daughters in nature, the decays continue until stable ^{206}Pb, ^{207}Pb, and ^{208}Pb are formed.

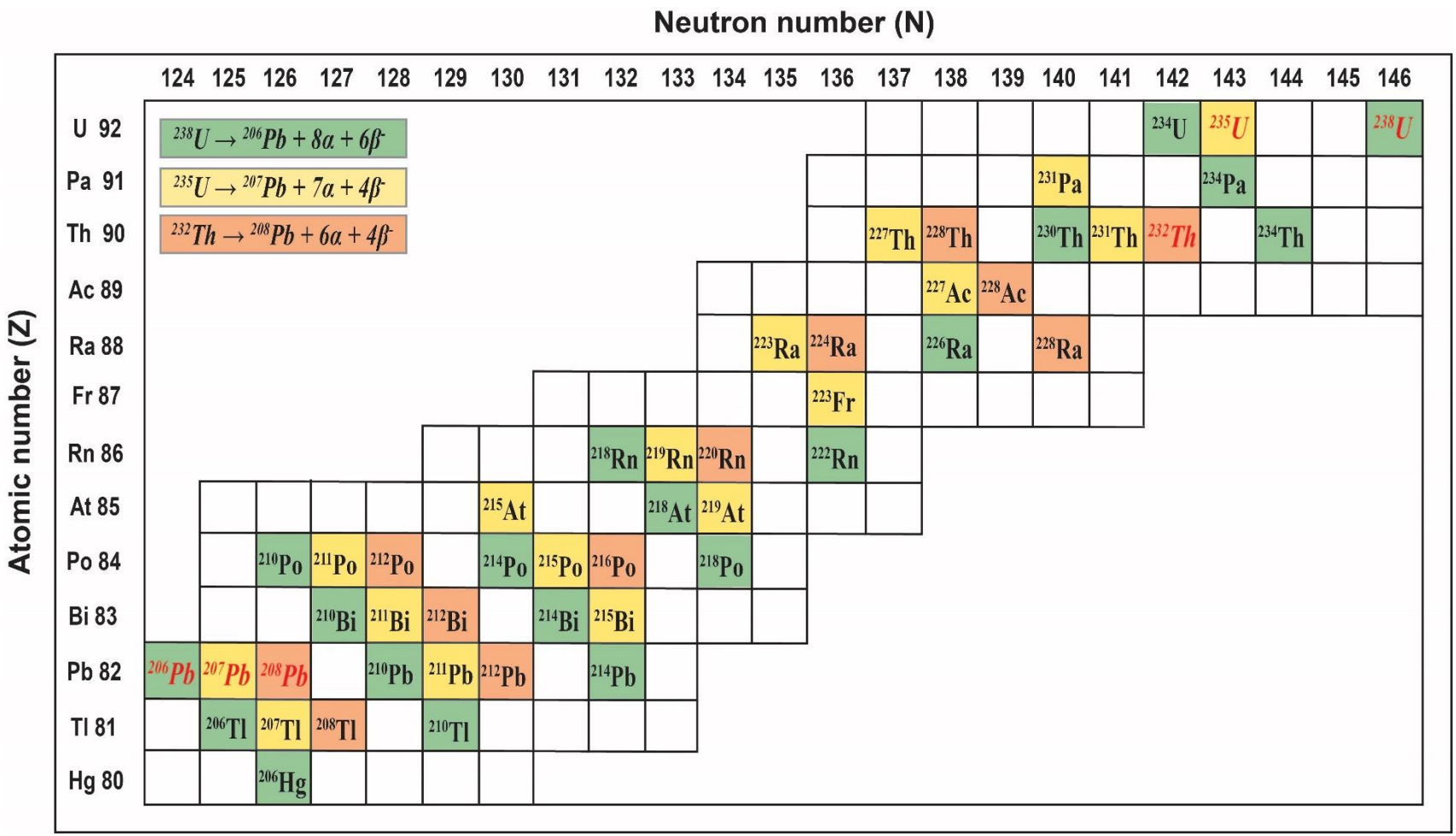

Figure 2.1. Decay chains of U-Th-Pb. Decays of ^{238}U to stable ^{206}Pb (green), ^{235}U to stable ^{207}Pb (yellow), and ^{232}Th to stable ^{208}Pb (orange) are illustrated (modified from Schoene, 2014). α is an alpha particle and β is a beta particle released during the decay.

As shown in Figure 2.1, ^{238}U decays into ^{206}Pb with the emission of eight alpha and six beta particles, even though intermediate products are brunched and decayed separately. This ^{235}U decays into the actinium series and forms ^{207}Pb, releasing seven alpha and four beta particles. ^{232}Th decay into ^{208}Pb, emitting six alpha and four beta particles.

A total of 43 isotopes of 12 elements are involved in the three chain reactions as intermediate elements. The daughters in one reaction series are not produced in another chain reaction, indicating that each chain results in the formation of stable Pb isotopes. Even though this is not a direct single reaction, I suppose that the secular equilibrium is established for the U and Th chain reactions. As ^{238}U, ^{235}U, and ^{232}Th isotopes have much longer half-lives compared to their intermediate daughters, which are very short-lived isotopes, at a geological time scale, the natural radioactive chains of these systems quickly reach equilibrium. Thus, it is believed that the respective Pb isotopes form directly from the initial isotopes, provided that the systems are closed with respect to Pb, U, Th, and all intermediate isotopes.

The difference in the chemistry of U and Th (parent elements) from that of Pb (daughter element) reflects on the large variations in Pb isotopic compositions (White et al., 2000). The Pb isotope ratios are rarely affected by physiochemical fractionation; however, the ratios of the parent radioactive isotope to the non-radiogenic isotope of the daughter element (i.e. $^{238}U/^{204}Pb$, $^{235}U/^{204}Pb$, and $^{232}Th/^{204}Pb$) are subjected to this fractionation. Thus, variations in the $^{238}U/^{204}Pb$, $^{235}U/^{204}Pb$, and $^{232}Th/^{204}Pb$ ratios result in different values of Pb isotope ratios. In fact, ^{204}Pb is weakly radioactive and produces ^{200}Hg with alpha emission, but has a very long half-life (1.4×10^{17} years, Holden and Walker, 1972), considering that ^{204}Pb is the stable isotope.

2.1.1.2. Isotopic U, Th-Pb methods of dating

To use the isotopic U and Th-Pb methods for dating, suitable minerals are required that retain U, Th, and Pb and which are widely present in different types of rocks. The most appropriate mineral is zircon as concentrations of U and Th in zircon, which replace Zr^{4+} (0.87 Å), are at least a few hundred ppm, and Pb^{2+}, which has a larger ionic radius (1.32 Å) than that of U^{4+} (1.05 Å) and Th^{4+} (1.10 Å), cannot be incorporated into zircon to replace Zr^{4+} due to the differences in its charge and ionic radius.

The following assumptions were made to obtain valid dates, including the assumptions that the minerals stayed closed, particularly to U, Th, and Pb (and all intermediate daughter elements), after the minerals were formed, and suitable initial Pb isotopic ratios and accurate decay constants of ^{238}U, ^{235}U, and ^{232}Th are required. The following equations based on the three different decay series were solved independently for ***t***.

$$(^{206}Pb/^{204}Pb) = (^{206}Pb/^{204}Pb)_0 + (^{238}U/^{204}Pb)(e^{\lambda 1 t} - 1)$$
$$(^{207}Pb/^{204}Pb) = (^{207}Pb/^{204}Pb)_0 + (^{235}U/^{204}Pb)(e^{\lambda 2 t} - 1)$$
$$(^{208}Pb/^{204}Pb) = (^{208}Pb/^{204}Pb)_0 + (^{232}Th/^{204}Pb)(e^{\lambda 3 t} - 1)$$

where $(^{206}Pb/^{204}Pb)$, $(^{207}Pb/^{204}Pb)$, and $(^{208}Pb/^{204}Pb)$ are the Pb isotope ratios in the mineral from the analysis; $(^{206}Pb/^{204}Pb)_0$, $(^{207}Pb/^{204}Pb)_0$, and $(^{208}Pb/^{204}Pb)_0$ are the initial Pb isotope ratios incorporated when it was crystalized; $(^{238}U/^{204}Pb)$, $(^{235}U/^{204}Pb)$, and $(^{232}Th/^{204}Pb)$ are the isotopic ratios in the mineral from the analysis; λ_1, λ_2, and λ_3 are the decay constants of ^{238}U, ^{235}U, and ^{232}Th, respectively; and t is the elapsed time after the minerals were crystallised (or the elapsed time from the closure of the mineral to U, Th, Pb, and all other intermediate daughters).

Complying with all the assumptions, the independent dates were found to be identical, which is known as concordant. Thus, this common age represents the time of mineral crystallisation, i.e. the age of the mineral. We can obtain these ages from the equations above that are not different, known as discordant. As most of the minerals did not remain closed to U, Th, and Pb or even the intermediate daughters after the mineral was formed, the system would gain or lose these elements, reflecting the age when using the U and Th-Pb methods.

The problem if most of U and Th bearing minerals yielding discordant ages was overcome by Wetherill (1956; 1963) and Ahrens (1955). From the equations above, they calculated the compatible sets of $^{206}Pb^*/^{238}U$ (equal to $e^{\lambda 1 t}-1$) and $^{207}Pb^*/^{235}U$ (equal to $e^{\lambda 2 t}-1$) ratios (the * symbol means radiogenic Pb isotope ratios, i.e. the analysed value subtracted from the initial values***)*** based on the different values of t. These values form the curve called 'Concordia' (Wetherill, 1956) on the coordinates of $^{206}Pb^*/^{238}U$ (x-coordinate) and $^{207}Pb^*/^{235}U$ (y-coordinate) in the U-Pb system.

Generally, the U-bearing phases lose fractions of its radiogenic Pb through metamorphism or chemical weathering. The values that lose its radiogenic Pb (or gain U) in various proportions would generate a straight line (called 'Discordia') with two points of intersection with the Concordia curve through extrapolation, forming the chord. From the Discordia, we can define these two points on the Concordia curve as the age of the event and the age of the mineral. Cautions are taken in the interpretations and it should be confirmed by other evidence when the systems lose Pb by either a continuous diffusion or one geological event. Thus, these Concordia diagrams allow us to interpret the history of the mineral as experienced from the different dates of the mineral.

In addition, the Concordia concept was applied to the U-Th-Pb system (Wasserburg, 1963; Allegre, 1967). Unlike the U-Pb Concordia curve, the Concordia curve for $^{208}Pb/^{232}Th$ and $^{206}Pb/^{238}U$ ratios is fairly straight due to the similar half-lives of ^{232}Th and ^{238}U. This resulted in the intersections of Discordia with the Concordia curve to have a large error, indicating that the systems are unsuitable for geochronometry, whereas the Concordia curve on $^{208}Pb/^{232}Th$ and $^{207}Pb/^{235}U$ ratios was analogous to the U-Pb Concordia curve. As U and Th have different chemical properties, the Th/U ratios change during geological episodes with a continuous gain or loss of U and Th. In addition, fractionations can occur among ^{206}Pb, ^{207}Pb, and ^{208}Pb. When these alterations occur, it prevents the Discordia from passing the origin, and thus the lower intersections on U-Th-Pb Concordia curves do not indicate a meaningful age that reflects the changes in the Th/U ratio or Pb isotope ratios.

The three equations above can be used to plot three independent isochrones in coordinates of $^{206}Pb/^{204}Pb$ and $^{238}U/^{204}Pb$ or $^{207}Pb/^{204}Pb$ and $^{235}U/^{204}Pb$ in the U-Pb system as well as in the coordinates of $^{208}Pb/^{204}Pb$ and $^{232}Th/^{204}Pb$ in the Th-Pb system. The slopes in these coordinates indicate the age of the samples. Two U-Pb isochrons often fail to acquire a reasonable age as loss of a significant fraction of U often occurs in the samples due to chemical weathering, whereas Th-Pb isochron is useful as both elements are retained well (i.e. both elements are not mobile under the oxidising environment) as compared to U from chemical weathering (e.g. Rosholt and Bartel, 1969). For the U-Pb system, the two equations can be combined [$(^{207}Pb/^{204}Pb)^*/(^{206}Pb/^{204}Pb)^* = 1/137.8 \times ((e^{\lambda 2t}-1)/(e^{\lambda 1t}-1))$] using 1/137.8 as the $^{235}U/^{238}U$ ratio, which is considered as a constant value for the Earth, moon, and meteorites assuming that the isotope fractionation between them

does not occur. Thus, the co-genetic rocks or minerals lie along a straight line whose slope is $1/137.8 \times ((e^{\lambda 2t}-1)/(e^{\lambda 1t}-1))$ when all the following conditions are satisfied: all samples should have the same age, same initial Pb isotope ratios, and remain closed before they are exposed to chemical weathering. As the dates obtained through radiogenic $^{207}Pb/^{206}Pb$ ratio are not influenced by losses of U or Pb, the dates generally indicate the most suitable time for mineralisation.

2.1.1.3. Common Pb

Common Pb refers to the condition wherein the Pb isotopic composition in the minerals whose U/Pb and Th/Pb ratios are very low or zero, indicating that the parent isotopes of the three radiogenic Pb isotopes are not incorporated in these phases after the mineral formed. Thus, no radiogenic Pb was generated after the minerals were crystallised, i.e. the initial Pb isotopic compositions in the phases were constant with time. The major phases for common Pb studies are generally composed of sulfide minerals of base metals (principally galena) and K-feldspar in which the potassium ion (K^{+1}) is replaced by lead (Pb^{+2}). The secondary Pb phases of Cerussite ($PbCO_3$) and anglesite ($PbSO_4$), secondary lead phases, are rarely studied. Thus, it is unlikely that the U-Th-Pb systems, where the Pb isotopes are produced by radioactive decay of U and Th, are present in a phase whereas it emphases on the initial Pb isotopic composition of a phase.

Pb isotope analysis was first conducted by Aston (1927), who found that the atomic weights of the elements are based on the abundances of their natural isotopes. From the Pb isotope analysis, they observed that the atomic weight of common Pb is constant, indicating that the isotopic compositions are constant, whereas the atomic weight of Pb occurring with U was considerably less than that of common Pb due to the presence of radiogenic ^{206}Pb. Pb isotopic compositions are commonly expressed by the ratios of a radiogenic isotope to the non-radiogenic isotope for the mathematical interpretation, such as $^{206}Pb/^{204}Pb$, $^{207}Pb/^{204}Pb$, and $^{208}Pb/^{204}Pb$.

Nier (1938; 1941) first reported the Pb isotope variations in galenas from different sources and different ore deposits. He observed that the weights of Pb in galenas samples were almost constant even though they have different Pb isotopic compositions. The increase in $^{206}Pb/^{204}Pb$ ratio with the increase in $^{208}Pb/^{204}Pb$ ratio indicates the constancy of the atomic weight of common Pb. We believe that the Earth starts with some primeval Pb, and the Pb isotopic composition of the troilite phase in meteorites are used for determining the values of primeval Pb isotopes, which are

the least radiogenic Pb (Doe and Stacey, 1974). Nier (1941) suggested that the mixing of primeval Pb and radiogenic Pb prior to the deposition of the galena causes variable Pb isotopic compositions in galena from different ore deposits. This has resulted in the direction of the quantitative treatment of the isotopic composition of common Pb as well as the calculations of the age of Earth.

The fact that the sulfide minerals retain the constant initial Pb isotopic compositions with time has become an important aspect in fingerprinting for tracing the sources of Pb, as Pb isotopic compositions are not fractionated (or not measurably fractionated) depending on the redox condition in solution or fluid-mineral interactions (Macfarlane and Petersen, 1990), indicating the usefulness of this tool in tracing sources of Pb. It is also useful in understanding the ore-formation and evolving processes as well as constraining the timing of the deposit (i.e. an estimate of the age of mineralisation).

Models for the isotopic evolution of Pb in the Earth

The isotopic evolution of Pb over the history of Earth has been studied for almost a century. The first quantitative model that accurately matched the age of Earth and average isotopic composition was proposed by Holmes (1946) and Houtermans (1946), respectively, known as the Holmes and Houtermans model, even though the age of Earth (3940 million years) was first calculated by Gerling (1942). This evolutionary model was significantly simplified as several assumptions were made for this model, such as the Earth evolved from a single closed reservoir. Thus, this model explained that the isotopic composition of common Pb in any given sample experienced a single-stage history, indicating that the radiogenic Pb resulted from only the radioactive decay of U and Th in the source areas, i.e. the changes in $^{238}U/^{204}Pb$, $^{235}U/^{204}Pb$, and $^{232}Th/^{204}Pb$ ratios are only due to the decay of U and Th. Then, the mixture of primeval Pb with this radiogenic Pb was withdrawn from the sources and separated to be incorporated into ore mineralisation.

This single-stage age (or model age) as per the Holmes and Houtermans model can begin from the same equation presented in section 2.1.1.2. For example, the equation for $^{206}Pb/^{204}Pb$ ratio of U-bearing systems of age **T** that has remained closed to U, Pb, and all intermediate daughters is

$$(^{206}Pb/^{204}Pb) = (^{206}Pb/^{204}Pb)_0 + (^{238}U/^{204}Pb)(e^{\lambda T} - 1).$$

If Pb was extracted from this system ***t*** years ago, the $^{206}Pb/^{204}Pb$ ratio of Pb would

$(^{206}Pb/^{204}Pb)_t = (^{206}Pb/^{204}Pb)_0 + (^{238}U/^{204}Pb)(e^{\lambda T} - 1) - (^{238}U/^{204}Pb)(e^{\lambda t} - 1)$

$= (^{206}Pb/^{204}Pb)_0 + (^{238}U/^{204}Pb)(e^{\lambda T} - e^{\lambda t})$

where

T: age of the Earth

t: elapsed time since the withdrawal of a common Pb sample from the source

$(^{206}Pb/^{204}Pb)_0$: isotope ratio of primeval Pb **T** years ago on Earth

$(^{206}Pb/^{204}Pb)_t$: isotope ratio of common Pb of age ***t***

$(^{238}U/^{204}Pb)$: isotope ratio in the source region of common Pb at present.

Two more equations can be written in a similar way for the other two decay systems (i.e. ^{207}Pb from ^{235}U and ^{208}Pb from ^{232}Th) as well as a combined equation for the two U-Pb decay equations by using the 1/137.8 ratio instead of the $^{235}U/^{238}U$ ratio. In particular, the $^{238}U/^{204}Pb$ ratio was omitted in the combined equation and, thus, fewer constants are required to date samples of common Pb. The three equations are

$(^{207}Pb/^{204}Pb)_t = (^{207}Pb/^{204}Pb)_0 + ^{238}U/^{204}Pb \times 1/137.8\ (e^{\lambda 2T} - e^{\lambda 2t})$

$(^{208}Pb/^{204}Pb)_t = (^{208}Pb/^{204}Pb)_0 + ^{238}U/^{204}Pb \times ^{232}Th/^{238}U\ (e^{\lambda 3T} - e^{\lambda 3t})$

$[(^{207}Pb/^{204}Pb)_t - (^{207}Pb/^{204}Pb)_0] / [(^{206}Pb/^{204}Pb)_t - (^{206}Pb/^{204}Pb)_0] = 1/137.8[(e^{\lambda 2T} - e^{\lambda 2t}) / (e^{\lambda 1T} - e^{\lambda 1t})]$.

As mentioned further up, this single-stage model age assumes that common Pb from all the samples is a mixture of primeval Pb with radiogenic Pb, which formed in the source areas with different ratios of $^{238}U/^{204}Pb$ and $^{232}Th/^{238}U$. The growth curves on the coordinates of $^{206}Pb/^{204}Pb$ (x-coordinate) and $^{207}Pb/^{204}Pb$ (y-coordinate) extend from the point of primeval Pb (representative primeval Pb value) and indicate that common Pb in various ore deposits has evolved with various $^{238}U/^{204}Pb$ values between 8 and 10 depending on their source regions (Faure, 1977). Thus, the point on the growth curves of $^{206}Pb/^{204}Pb$ and $^{207}Pb/^{204}Pb$ coordinates can imply the time (called the model date) at which Pb was withdrawn from the source area and subsequently incorporated into the ore as a common Pb phase, i.e. sulfide minerals and K-feldspar.

Therefore, if common Pb (or ordinary Pb) was extracted from different source regions at the same time ***t*** (***t*** is constant), these Pb should lie on the straight lines called isochrones (isochrones have specific ratios of $^{238}U/^{204}Pb$ depending on their respective source areas). Thus, the isochrones intersected with the growth curves corresponding to the ages. The slope of the isochrones is given by $1/137.8 \times [(e^{\lambda 2T} - e^{\lambda 2t}) / (e^{\lambda 1T} - e^{\lambda 1t})]$, which is a function of only the model age, ***t*** (if the age of the Earth, **T**, is known).

However, a relatively small number of ore deposits yielded useful model ages (single-stage Pb ages) (e.g. Doe and Stacey, 1974), whereas a large number of ore deposits rarely agreed with the single-stage model ages as common Pb in most ore deposits had more complicated histories (stages) than those provided by the Holmes-Houtermans model. The Pb that does not follow the single-stage history is called the anomalous Pb, whose ordinary model ages (i.e. single-stage history Pb age) are meaningless. This anomalous Pb can be explained in terms of the mixing model having different ratios of $^{238}U/^{204}Pb$ or multistage growth. The mixing model (including the instantaneous-growth and the continuous-growth models) indicates that variable amounts of radiogenic Pb contaminant were added to the ordinary Pb and produced an array (a straight line) of anomalous Pb (Faure, 1977). The mixing occurs among several sources of materials whose isotopic compositions are heterogeneous.

The vast number of regionally distinct differentiation events that occurred on Earth was taken into account by Kramers and Tolstikhin (1997), who greatly improved the Stacey and Kramers' model (1975), which they admitted as being grossly inaccurate. The basic concept of the two-stage model by Stacey and Kramers (1975) is that Pb has passed two systems that have U with different ratios of $^{238}U/^{204}Pb$. The Pb was removed from the first system and, then, transferred to the second system (i.e. Pb isotope composition evolved by a single-stage history until the later event or episode occurred, causing the $^{238}U/^{204}Pb$ ratio to change to values different from those in the first system). The second system is either a different region within the first source region (i.e. transferred physically) or the second environment, which has a different $^{238}U/^{204}Pb$ ratio than that of the former system without movement.

The equation of $^{206}Pb/^{204}Pb$ ratio for the two-stage dates is

$$^{206}Pb/^{204}Pb = (^{206}Pb/^{204}Pb)_0 + (^{238}U/^{204}Pb)_1 \times (e^{\lambda 1T} - e^{\lambda 1t1}) + (^{238}U/^{204}Pb)_2 \times (e^{\lambda 1t1} - e^{\lambda 1t2})$$

where

t1 = time when Pb was withdrawn from the first system and transferred to the second system

t2 = time when Pb was removed from the second system and its isotopic composition stopped changing.

The other symbols are the same as in the previous equations.

The other equation (i.e. ^{207}Pb from ^{235}U) is written similarly and the combined equation of two U-Pb decay equations is written using the 1/137.8 ratio instead of the $^{235}U/^{238}U$ ratio. The two equations are

$$^{207}Pb/^{204}Pb = (^{207}Pb/^{204}Pb)_0 + (^{235}U/^{204}Pb)_1 \times (e^{\lambda 1T} - e^{\lambda 1t1}) + (^{235}U/^{204}Pb)_2 \times (e^{\lambda 1t1} - e^{\lambda 1t2})$$

$$[(^{207}Pb/^{204}Pb)_{t2} - (^{207}Pb/^{204}Pb)_0 + (^{235}U/^{204}Pb)_1 \times (e^{\lambda 1T} - e^{\lambda 1t1})] / [(^{206}Pb/^{204}Pb)_{t2} - (^{206}Pb/^{204}Pb)_0 + (^{238}U/^{204}Pb)_1 \times (e^{\lambda 1T} - e^{\lambda 1t1})] = 1/137.8 \times [(e^{\lambda 2t1} - e^{\lambda 2t2}) / (e^{\lambda 1t1} - e^{\lambda 1t2})$$

On the coordinates of $^{206}Pb/^{204}Pb$ and $^{207}Pb/^{204}Pb$, the Pb isotopic data show straight lines called secondary isochrones. As shown in the equations for the two-stage processes, this form of secondary isochrones is similar to the isochrones in the one-stage process, substituting an evolved Pb with the primeval Pb and substituting the age of the Earth with the age of the beginning of the second stage. Thus, if one of the ages, i.e. either the age of mineralisation or the age of the source material of Pb is known (or can be reasonably estimated), we can calculate the other age in the two-stage histories (Stacey et al., 1967; Kanasewich, 1962). The secondary isochron is also suitable for tracing the Pb source in the deposits (e.g. Doe and Delevaux, 1972), matching the secondary isochrones.

Three or more stages can be extrapolated based on the two-stage history; however, equations of these stages are not suitable to date or interpret the history directly as many values, such as $^{238}U/^{204}Pb$, and/or residence times for each system are unknown. The growth of Pb with these multiple stages, however, produces specific patterns on the Pb diagrams and, thus, is useful in quantitative interpretation.

2.1.2. General background of S isotopic compositions

Sulfur (S) is the 16th element (the number of protons of sulphur is 16) in the periodic table and has four stable isotopes, ^{32}S, ^{33}S, ^{34}S, and ^{36}S, with abundances of 95.05%, 0.75%, 4.21%, and 0.02%, respectively (Macnamara and Thode, 1950). Since S is 14th most abundant element in the Earth's crust and the 10th most abundant element in the universe (Seal, 2006), S isotope geochemistry has been broadly studied for the origins of the S-bearing phases.

The fractionation of S isotopes, i.e. the preferential partitioning among sulfide, sulfate, and aqueous S species, results in variations in the S isotopic composition of those phases. Generally, stable isotopes are not expressed in the absolute abundance of isotopes; however, the relative partitioning of isotopes among the different phases with a principal ratio of $^{34}S/^{32}S$, as the most abundant of these two S isotopes, thus, it enables the analysis. Additionally, different isotopic ratios are systematically fractionated based on mass differences. However, most fractionations of stable isotopes of S are relatively small, showing variations in the 5th or 6th decimal place. Thus, the delta (δ) notation, which is relative to reference material, is widely employed. The $\delta^{34}S$ (per mil; ‰) is defined as

$$\delta^{34}S = [\{(^{34}S/^{32}S)_{sample} - (^{34}S/^{32}S)_{reference}\}/(^{34}S/^{32}S)_{reference}] \times 1000$$

As meteorite sulfide minerals represent the primordial S isotopic composition of the Earth (Nielsen et al., 1991) and reflect isotopic differentiation since the formation of the Earth, the Vienna Canyon Diablo Troilite (VCDT) has been broadly used as the reference material; more recently, a silver sulfide reference material, IAEA-S-1, has been accepted for use due to a shortage of VCDT. The $\delta^{34}S$ of VCDT is 0‰ by definition and the assigned value of IAEA-S-1 is −0.3‰ (Krouse and Coplen, 1997).

The isotopic fractionation factor ($\alpha_{A\text{-}B}$) between two substances (A and B) is defined as R_A/R_B, where R is $^{34}S/^{32}S$. The value of $\alpha_{A\text{-}B}$ is $(1000 + \delta_A) / (1000 + \delta_B)$ in terms of the δ value. In addition, $\Delta_{A\text{-}B}$ for the fractionation factor is utilised by defining $\Delta_{A\text{-}B} = \delta_A - \delta_B$, which is nearly equal to $1000\ln\alpha_{A\text{-}B}$ (Seal, 2006).

2.1.2.1. Factors for S isotope fractionation

In terrestrial systems, two main reference reservoirs for S isotopic compositions on Earth are present, including meteoric S, which presumably represents the bulk composition of the Earth and seawater S. These two reference reservoirs have $\delta^{34}S$ of 0.2 ± 0.2‰ (Kaplan and Hulston,

1966) for Canyon Diablo Troilite and 21.0 ± 0.2‰ for dissolved sulfate in modern oceans (Rees et al., 1978).

S isotope fractionation mostly results from kinetic or equilibrium reactions. The kinetic processes are caused by the thermodynamic properties of molecules, i.e. heavier isotopes have lower translational and vibrational velocities, indicating that the bonds with heavier isotopes are difficult to break. Typically, chemical reactions such as bacterial reduction and physical processes such as diffusion or evaporation (O'Neil, 1986) are involved in the kinetic processes.

The equilibrium fractionation is also based on the thermodynamic properties of the molecule, which is the effect of atomic mass on bonding. The strength of bonding with a heavier isotope is stronger than that with a lighter isotope. The isotopic exchange reaction is included in the equilibrium process, causing the rearrangement of the isotopes in different substances.

Various factors such as temperature, chemical variables, crystal structure, and pressure control the magnitude of equilibrium fractionation. The temperature and chemical composition are the most significant factors, whereas pressure is generally the least important factor in the upper crustal system (O'Neil, 1986). The chemical composition, such as atomic mass, electronic configuration of the isotopic element, ionic charge, oxidation state, and the element in which S isotopes are bound, are important factors that influence the equilibrium fractionation (O'Neil, 1986). For S systems, the oxidation state of S is very significant due to the ^{34}S-enrichment in higher oxidation states (i.e. SO_4^{2-}) and ^{34}S-depletion in the lower oxidation states (i.e. S^{2-}) (Sakai 1968; Bachinski 1969). This trend clearly shows that sulfide phases have lower $\delta^{34}S$ values than co-genetic sulfate phases. In addition, the cations bound to the S species can affect the fractionation because lighter S isotopes are likely to bond with heavier elements than lighter elements. Thus, sphalerite (ZnS) is more enriched in ^{34}S than galena (PbS) as Pb is heavier than Zn, indicating that Pb forms a stronger bond with lighter isotopes (O'Neil et al., 1969).

The relative effect related to the temperature (T) causes the difference in vibrational energies between two different substances (i.e. A and B), forming the basis of S isotope geothermometry. Thus, the dependence of S isotope fractionation on temperature can be described by the following equation:

$$1000 \ln\alpha_{A\text{-}B} = a / T^2 + b / T + c$$

where a, b, and c are the empirically determined constants.

For example, the fractionation of two sulfide minerals, sphalerite, and galena, which were cogenetic at a single temperature (T), i.e. in equilibrium with each other, can be derived as $\Delta_{Sph\text{-}Gn} = 1000\ \ln\alpha_{Sph\text{-}H2S} - 1000\ln\alpha_{Gn\text{-}H2S}$. The constant 'a' for sphalerite is 0.10 and that for galena is −0.63 (Ohmoto and Rye, 1979). Thus, we can calculate T by substituting the value of 'a' with uncertainties in S isotopic T that ranges between ± 10 and 40 °C (Ohmoto and Rye 1979).

2.1.2.2. Processes for S isotopic variations

As mentioned above, S isotopic variations result from various kinetic and equilibrium processes, which are categorised as mass-dependent fractionation and mass-independent fractionation.

Mass-dependent fractionation

In geological systems, variations in the thermodynamic properties of molecules depend on mass, resulting in isotopic fractionation. This is called mass-dependent fractionation, and as mentioned above, this isotopic fractionation results in the systematic correlations of S stable isotopes in proportion to mass differences among isotopes.

Rayleigh distillation processes can describe the various equilibrium and kinetic processes in a mass-dependent system. The equations of the Rayleigh distillation processes and recast by δ for S isotopes are as follows:

$$R = R_0\, f^{(\alpha-1)}$$

$$\delta^{34}S + 1000 = (\delta^{34}S_0 + 1000)\, f^{(\alpha-1)}$$

where R is the isotopic ratio when a fraction (*f*) of the starting amount remains, R_0 is the initial isotopic ratio, and α is the fractionation factor.

For example, this model explains the bacterial reduction of seawater sulfate to sulfide phases using the equation. If α (1.0408) and $\delta^{34}S_0$ (21.0‰) are known and the precipitation of sulfides, such as pyrite from H_2S, produced from the bacterial reduction of sulfate starts to preferentially include the lighter isotope, (^{32}S), showing the first precipitation of pyrite has a $\delta^{34}S$ value of approximately −20‰. If the preferential removal of ^{32}S by bacterial reduction of seawater sulfate continuously occurs, $\delta^{34}S$ value of the residual aqueous sulfate increases, causing an increase in $\delta^{34}S$ value of subsequent pyrite precipitation (Ohmoto and Goldhaber, 1997; Seal et al.,

2000; Seal, 2006). Thus, based on the timing of the precipitation of pyrite, i.e. the reaction progress, the $\delta^{34}S$ values of individual pyrites vary.

In addition, the mixing process is another factor that leads to isotopic fractionation. Based on the mass-balance equations, we can calculate the mole fraction of the mixed components.

The most common and significant processes of kinetic and equilibrium processes resulting in fractionation, such as isotopic exchange, sulfate reduction, sulfide oxidation, precipitation mechanisms of sulfide minerals, and disproportionation of SO_2, are introduced below in detail.

1) Isotope exchange reactions

The exchange rates of isotopes between dissolved SO_4^{2-} and H_2S were investigated by Ohmoto and Lasaga (1982) as a function of pH. They reported that the exchange rates decreased with increasing pH at a pH < 3, and the rates remained constant between pH 4 and 7. Above pH 7, the rates decreased due to the abundance of pH-dependent S species, thiosulfate ($S_2O_3^{2-}$). In addition, at elevated temperature (350 °C) and low pH (≈2), the equilibrium rate is higher, attaining 90% equilibrium between aqueous sulfate and sulfide within approximately 4 h, whereas at low temperature (25 °C) and neutral pH (between 4 and 7), 90% equilibrium was attained at 9×10^9 years (Ohmoto and Lasaga, 1982).

2) Sulfate reduction

Sulfate reduction, which is controlled by non-equilibrium and kinetic processes, can occur in both biotic and abiotic environments. First, sulfate reduction in the biotic environment is performed by sulfate-reducing bacteria such as *Desulfovibrio desulfuricans*. The bacteria are generally active in anoxic environments at neutral pH with temperatures between 20 and 40 °C; however, it can also exist at temperatures ranging from 0 to 110 °C and pH of 5 to 9 (Postgate 1984; Canfield 2001; Berner 1985). The bacterial sulfate reduction causes higher enrichment of ^{34}S in the sulfate relative to the sulfide, indicating that the bacteria easily metabolise ^{32}S as compared to ^{34}S.

The fractionation from sulfate bacterial reduction ranges from 15 to 71‰ in marine environments, indicating that the magnitude of this fractionation depends on the rate of sulfate reduction associated with the sedimentary rates, i.e. rapid sulfate reduction and sedimentation result in smaller fractionations whereas sluggish sulfate reduction and sedimentation result in the

larger fractionations (Goldhaber and Kaplan 1975; Canfield and Teske 1996; Canfield, 2001). Additionally, these authors have suggested that partial oxidation and the effect of disproportionation of intermediate S species can cause greater fractionation in marine environments characterised by resultant sulphide.

Furthermore, the isotopic composition of the resultant sulfide may depend on the condition of the system in which bacterial reduction occurs. An open system indicates that the source of sulfate is not limited and is transported rapidly to the place where reduction occurs. If the system is closed, the source of sulfate is finite and becomes exhausted at the end. Thus, the isotopic compositions of sulfides from the bacterial reduction are distinctive between the open and closed systems. The spectrum of the distribution pattern by a model by Seal and Wandless (2003) shows that the system is closed, and a flat distribution is observed as the sulfate reservoir is continuously depleted; if the system is open, the model shows a sharp mode.

Another type of reduction of aqueous sulfate is the abiotic reduction, i.e. thermochemical reduction. This process is based on the interaction of aqueous sulfate with Fe^{2+}, which is probably derived from magnetite or olivine at high temperatures (Shanks et al., 1981). The isotopic composition of aqueous sulfates becomes enriched in ^{34}S as the thermochemical reduction continues (Ohmoto and Lasaga, 1982). If the reduction occurs at 400 °C with olivine, the isotopic fractionation is consistent with the fractionation of the equilibrium exchange between sulfides and sulfates (Sakai et al., 1980).

3) Sulfide oxidation, mechanism of sulfide precipitation, and disproportionation of SO_2

First, sulfide oxidation processes, such as oxidative weathering of sulfide minerals, rarely produce isotopic fractionation in the resultant sulfate minerals (or aqueous sulfate). Thus, the $\delta^{34}S$ values of the parent sulfide minerals and those of the various associated supergene sulfate minerals are similar (Taylor and Wheeler, 1994; Seal, 2003).

Second, various mechanisms to precipitate sulfide minerals also influence the S isotopic fractionation (Ohmoto and Goldhaber, 1997). For example, the relative proportions of metals (Zn, Pb, Fe, etc.) and H_2S is significant for simple sulfide phases such as sphalerite, pyrrhotite, and galena. Thus, disequilibrium fractionations, which are less than those expected under equilibrium conditions, occur when the molar concentrations of the dissolved metals surpass that of H_2S,

whereas equilibrium fractionations occur when the concentration of H_2S exceeds that of the metals due to their precipitation (Ohmoto and Goldhaber, 1997).

Finally, disproportionation of SO_2, which involves the most significantly oxidised S species, can affect the S isotope fractionation (Holland 1965; Burnham and Ohmoto 1980), indicating that SO_2 in a high oxygen fugacity system produces H_2S (the most dominant reduced S species) and SO_4^{2-} through cooling below approximately 400 °C.

Mass-independent fractionation

All the processes mentioned above cause mass-dependent fractionation, of which, variations in $^{34}S/^{32}S$ should be approximately half of the $^{36}S/^{32}S$ ratio and twice that of $^{33}S/^{32}S$, whereas the mass-independent fractionation does not follow any such systematic variations (Hulston and Thode 1965). Thus, samples that underwent mass-dependent fractionation processes form a mass fractionation line on a graph between two isotopic ratios, and the slope of the line depends on the relative mass difference between the two ratios. Thus, the slopes are approximately 0.515 on the $\delta^{33}S$ vs. $\delta^{34}S$ plot and 1.91 on the $\delta^{36}S$ vs. $\delta^{34}S$ plot, representing the deviations from the terrestrial fractionation lines. Deviations from the lines (or isotope anomalies) indicate mass-independent fractionation processes. That is, mass-independent fractionation processes are defined when $\Delta^{33}S$ ($= \delta^{33}S - 1000[(1 - \delta^{34}S/1000)^{0.515} - 1]$) and $\Delta^{36}S$ ($= \delta^{36}S - 1000[(1 - \delta^{34}S/1000)^{1.91} - 1]$) values are not zero.

The mass-independent fractionation of S results from the photochemical processes in the upper atmosphere (Farquhar and wing, 2003), which has been observed in sulfide and sulfate minerals of the Archean period (Farquhar et al., 2000a). The $\Delta^{33}S$ values range from −2.5‰ to 8.1‰ for samples prior to 2.4 Ga, and from −0.5‰ to 0.7‰ for samples since 2.4 Ga (Farquhar et al., 2000a; Ono et al., 2003; Rumble, 2005; Savarino et al., 2003; Bekker et al., 2004). The abrupt end of mass-independent fractionation in S probably results from the development of an oxygenised atmosphere, and an ozone layer shielded the atmosphere from photochemical processes induced by ultraviolet radiation (Farquhar et al. 2000a; Pavlov and Kasting 2002; Farquhar and Wing 2003; Bekker et al. 2004).

2.1.2.3. Geochemical environments for S stable isotopes

We can briefly introduce various geochemical environments such as meteorites, marine sediments, coal, mantle, and igneous rocks and magmatic sulfide deposits for S isotopes as follows (Seal, 2006).

The S isotopic compositions of a variety of S species obtained from meteorites, such as sulfide, sulfate, and S in solid solution in native Fe, can indicate the origin of the Earth and the solar system. As meteorite, i.e., Vienna Canyon Diablo Troilite (VCDT) has been used as reference material for S isotopic composition, the S isotopic variations ($\delta^{34}S$) in meteorites are homogeneous and limited, mostly ranging from −2.5‰ to 2.5‰ (Hulston and Thode 1965a; Monster et al. 1965; Kaplan and Hulston 1966). Secondary alterations that occurred in the parent bodies were observed in some meteorites. For example, pyrite from the Martian meteorites (SNC type) shows Martian hydrothermal alteration with $\delta^{34}S$ values ranging from 4.8‰ to 7.8‰ (Shearer et al. 1996). The mass-independent isotope fractionation observed in meteorites was caused by photochemical reactions (Farquhar et al., 2000b), cosmic-ray induced reactions (Hulston and Thode, 1965), or S mixing from different reservoirs (Clayton and Ramadurai 1977).

Marine environments are also geochemically significant for S stable isotopes. The $\delta^{34}S$ value of modern seawater sulfate is 21.0 ± 0.2‰, indicating global homogeneity (Rees et al. 1978), whereas the $\delta^{34}S$ values of modern sedimentary sulfide minerals (pyrite) vary, even though negative values are dominant, between −50‰ and 20‰ (Chamber 1982; Strauss 1997). Marine sulfates from evaporate deposits or those disseminated in marine sediments indicate past S isotopic variations in sulfate in the oceans, suggesting secular variations in S isotopic compositions of sedimentary sulfide minerals (Holser et al. 1979; Claypool et al. 1980). The shift towards an oxygenated atmosphere at approximately 2.4 Ga was a significant event for the S cycle in the Earth. Before the atmosphere was oxygenated, the $\delta^{34}S$ of sedimentary sulfate and sulfide minerals were near 0‰ because of the lack of mechanisms to fractionate the S isotopes of the sulfate. However, as oxygen increased in the upper atmosphere around 2.4 Ga, the $\delta^{34}S$ values between sulfate (negative) and sulfide (positive) minerals in sediments became distinctively diverse, and mass-independent fractionation in S isotopes disappeared as the ozone layer prevented photochemical reactions in the atmosphere from the photochemical reaction, resulting in S isotope anomalies (Farquhar et al., 2000a). At approximately 0.7 Ga, a change in the $\delta^{34}S$ values between sedimentary sulfate and sulfide minerals were observed, i.e. more negative values of $\delta^{34}S$ for sulfate and higher

variability in sulfide values, probably resulting from a greater level of oxygenation of the oceanic water column (Canfield and Teske, 1996; Canfield, 2004).

The S isotopic composition of coal has also been studied, collectively showing a broad range of $\delta^{34}S$ for sphalerite, pyrite (and marcasite), and organic S from −14.6‰ to 18.7‰, −52.6‰ to 43.1‰, and −18.7‰ to 30.6‰, respectively (Seal, 2006). Most of the S in coal is derived from S in plant material (particularly in low-S coal) or bacterial reduction of aqueous sulfate (Price and Shieh 1979). The $\delta^{34}S$ of primary plant S is analogous to the $\delta^{34}S$ value of dissolved sulfate (its source), reflecting negligible S isotopic fractionations between them during the assimilation of S by plants (Chamber and Trudinger 1979). The $\delta^{34}S$ values of associated pyrite and organic S are correlated, indicating that the post-depositional mineralisation of organic matter was caused by sulfate-reducing bacteria (Price and Shieh, 1979). This explains the presence of S isotopes of sulfides and organic matter in coal globally. The $\delta^{34}S$ values of sulfides help identify seawater into coal-forming systems, i.e. the relative comparison of the two rates of bacterial sulfate reduction and downward sulfate supply shows varying trends of $\delta^{34}S$ from the top of the coal bed to the bottom (Simth and Batts, 1974).

S geochemical studies of the mantle and igneous rocks are less in number than those on sulfide deposits. However, the S isotopic composition of igneous rocks may describe the processes of partial melting and assimilation of country rocks. The $\delta^{34}S$ values of mantle obtained from mantle xenoliths and primitive igneous rocks are traditionally around 0 ± 2‰ (Thode et al., 1961), as well as the $\delta^{34}S$ values of melt inclusions in mantle xenoliths, sulfide in mid-ocean ridge basalts, and oceanic basalts. In basalts, the isotopic exchange between sulfide and sulfate minerals as well as their variable ratios can cause variability in the $\delta^{34}S$ values of sulfides (Sakai et al., 1984). The $\delta^{34}S$ values of sulfide inclusions in a variety of diamonds ranged from −11‰ to 14‰, with an average $\delta^{34}S$ of 1.2 ± 5.6‰, indicating that $\delta^{34}S$ values vary based on the type of diamonds. In the case of peridotitic diamonds, which directly indicate mantle provenance, the $\delta^{34}S$ of sulfide inclusion clusters is between −5‰ and +5‰, whereas in eclogitic diamonds, which show the subduction of S into the mantle, the $\delta^{34}S$ of sulfide inclusion range between −11‰ and 14‰ (Chaussidon et al. 1987; Eldridge et al. 1991). The S isotopic variations in both primitive and evolved igneous rocks globally reflect the S cycle of the Earth, including the bacterial sulfate reduction and oxidation reactions, as the concentration of oxygen in the atmosphere increases (Seal,

2006). The average $\delta^{34}S$ values in arc basalt (and gabbro), andesites, and granitoids are $1.0 \pm 3.2‰$, $2.6 \pm 2.3‰$, and $1.0 \pm 6.1‰$, respectively.

Lastly, several studies have been conducted on the S geochemistry on the magmatic sulfide deposits such as porphyry deposits, epithermal deposits, seafloor hydrothermal deposits, and Mississippi valley-type deposits. The S isotopic composition of sulfide minerals can identify the S contamination of magma that interacts with country rocks. In S-poor systems, the $\delta^{34}S$ of sulfide minerals is clustered near 0‰ as S conforms to the solubility of S in mafic magmas, whereas in the S-rich system, the $\delta^{34}S$ of sulfide minerals is positive and varies widely because of the contamination of crustal material (Zientek and Ripley, 1990; Ripley and Li, 2003). The S geochemistry of a variety of sulfide deposits is described below.

Porphyry deposits are associated with hydrothermal fluids from granitic magmas, which can be classified as I-type (more oxidised magma) and S-type (more reduced magmas), and is also involved in meteoric waters. Variations in S isotopes from the porphyry deposits associated with more oxidised magmatic fluids than other deposits are more variable due to the presence of both SO_2 and H_2S in the fluids, whereas S isotopic compositions in the deposits related to the I-type are less variable due to the dominant presence of H_2S in the fluids (Burnham and Ohmoto 1980). Based on the different magmatic hydrothermal settings, different classes of porphyry deposits are precipitated, such as Cu, Mo, W, Sn, Pb, Zn, and Au. The $\delta^{34}S$ values of the coexisting sulfide and sulfate minerals (e.g. pair of pyrite with anhydrite) in porphyry deposits may suggest a general approach to equilibrium at high temperatures. Thus, the approach of hydrothermal systems towards equilibrium conditions can be estimated using the T ranges of the hydrothermal systems (Rye, 2005). Compared to the porphyry deposits, epithermal deposits, which can be classified into acid-sulfate and adularia-sericite types (Heald et al. 1987), form at shallow levels of crust, indicating a low temperature of precipitation and are considered as the apical part of the porphyry deposits (Hedenquist et al. 1998). The $\delta^{34}S$ values of the sulfide and sulfate minerals from the epithermal deposits are more variable as compared to the $\delta^{34}S$ values from the porphyry deposits. However, the $\delta^{34}S$ values from the epithermal deposits indicate that the hydrothermal systems were in equilibrium conditions (Seal, 2006).

For S geochemistry in seafloor hydrothermal environments, modern systems such as the mid-ocean ridge (MOR) hydrothermal system and vent fluids and ancient systems such as volcanic-associated massive sulfide (VMS) deposits and sedimentary exhalative (SEDEX)

massive sulfide deposits can be used. For MOR hydrothermal systems, the three main sources of S, which have different S isotope signatures, are leaching from country rocks, thermochemical reduction of seawater sulfate, and leaching of sulfide minerals in sediments that were formed by bacterial reduction (Seal, 2006). Thus, in modern seafloor sulfide minerals and vent fluids, S isotopic variations are determined by the mixture of these sources through processes such as simple adiabatic mixing and dissolution of sulfide minerals.

In the case of ancient systems, S isotopic compositions of sulfides are determined by processes similar to those in modern systems, but with additional processes such as secular variations in S isotope composition of seawater and global occurrence of anoxic waters. Ancient systems are represented as VMS deposits that formed at active MOR spreading centres, in addition to arc and rift systems and SEDEX deposits that formed in failed rift systems (Leggett, 1980; Seal, 2006). Secular variations in the S isotope composition of pyrite and marine sulfates in the deposits were noticeable and indicate the primary role of oxygen in the atmosphere in the S cycle (Huston, 1999). Prior to 2.4 Ga, the $\delta^{34}S$ values of hydrothermal sulfides and sulfates from the two types of deposits were clustered near 0‰, whereas since 2.4 Ga, their $\delta^{34}S$ values have increased with a wider range; at 0.7 Ga, the $\delta^{34}S$ values rapidly increased due to the higher oxygen levels in the atmosphere (Canfield and Teske, 1996). The correlations of $\delta^{34}S$ values between the deposits and coeval seawater show approximately 17.5‰ difference for VMS deposits and 11.7‰ for SEDEX (Sangster, 1968), which were modelled to identify the processes of fractionation between sulfides from the deposits and seawater. The model showed that the quantification of simple adiabatic mixing and thermochemical reduction as two end-members with secular variations in the $\delta^{34}S$ values of seawater sulfate can explain the fractionation as well as the S isotopic disequilibrium (Janecky and Shanks, 1988).

The MVT deposits form in low-temperature and near-neutral continental settings in which S isotopic disequilibrium is dominant (Ohmoto and Lasaga, 1982), suggesting that the S stable isotopes of sulfide minerals from MVT deposits may indicate the source of the minerals and histories. S sources in MVT deposits include organic S, evaporates, connate seawater, and diagenetic sulfides, all of which originate from seawater sulfate through different geochemical processes, reflecting distinctive S isotopic signatures. The sulfate–sulfide fractionation by the bacterial reduction in MVT deposits ranges from 15‰ to 60‰ (Goldhaber and Kaplan 1975), with optimum temperature for bacterial activity between 30 and 40 °C (Jørgensen et al. 1992); the

fractionation by thermochemical reactions ranges from 0‰ to 10‰, which may occur away from the place of MVT sulfide deposits, i.e. in higher temperature environments, for effective kinetic reactions (Orr, 1974; Kiyosu, 1980; Ohomoto and Goldhaber, 1997). Two reservoirs of sulfide minerals were observed, one with $\delta^{34}S$ values between −5‰ to 15‰ and another with $\delta^{34}S$ values larger than 20‰ (Seal, 2006), suggesting the formation of H_2S from the open-system bacterial sulfate reduction for the lower values and the small fractionation by a thermochemical reduction for higher values of sulfides (Kesler 1996). Regardless of the different reduction processes, H_2S remains in S isotopic disequilibrium with associated sulfate minerals.

2.1.3. Motivation work: Study of Andes (Mondillo et al., 2018)

2.1.3.1. Introduction

The study area, Cristal Zn mineralisation, is located in the Bongara province, Peru (Fig. 2.2). The Zn mineralisation occurs as both sulfide and non-sulfide phases hosted in carbonate rocks of the Pucara Group, which is a Mesozoic sedimentary rock. The Pucara sedimentary sequence and one of its three main Formation, the Condorsinga Formation (Fig. 2.3), hosts several Zn-Pb deposits, including MVT and polymetallic Zn-Pb-Ag-Cu-Bi deposits. Based on the sedimentary and diagenetic characteristics, the Condorsinga Formation can be divided into Lower (approximately 100 m thick), Middle (approximately 120 m thick), and Upper (approximately 80 m thick) units (Peruana, 2005). The Middle unit, which consists of wacke- and packstones with pervasive dolomitisation, mostly hosts the Zn-Pb mineralisation. However, the MVT deposits for Zn sulfide mineralisation have been primarily studied in this province, such as the Florida Canyon, located 20–30 km south of the Cristal mineralisation.

The Cristal mineralisation covers an area approximately 1.5 km long and 500 m wide (Brophy, 2012), consisting of both sulfide and non-sulfide phases. The sulfides are mainly composed of sphalerite and pyrite with smaller amounts of galena. The sulfides were intergrown within the sparry dolomite. Two extensive ore bodies were found and explored in the centre of the Cristal mineralisation: Esperanza, from where, samples were collected for this study, covering an

area approximately 150 m long and 90 m wide, and Yolanda area, covering an area approximately 50 m long and 10 m wide.

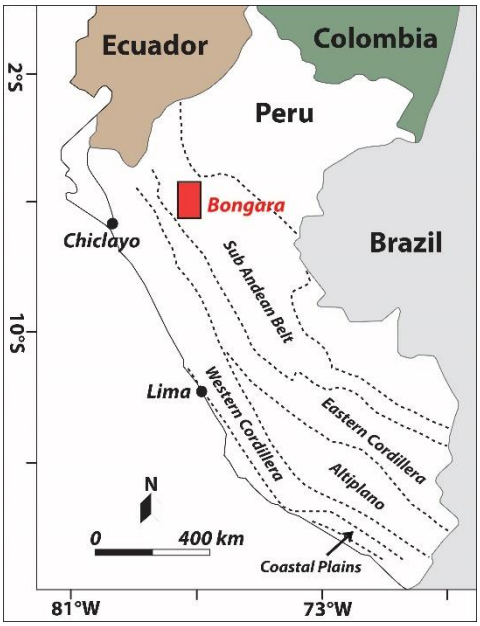

Figure 2.2. Location of the study area in Peru (modified from Mondillo et al., 2018)

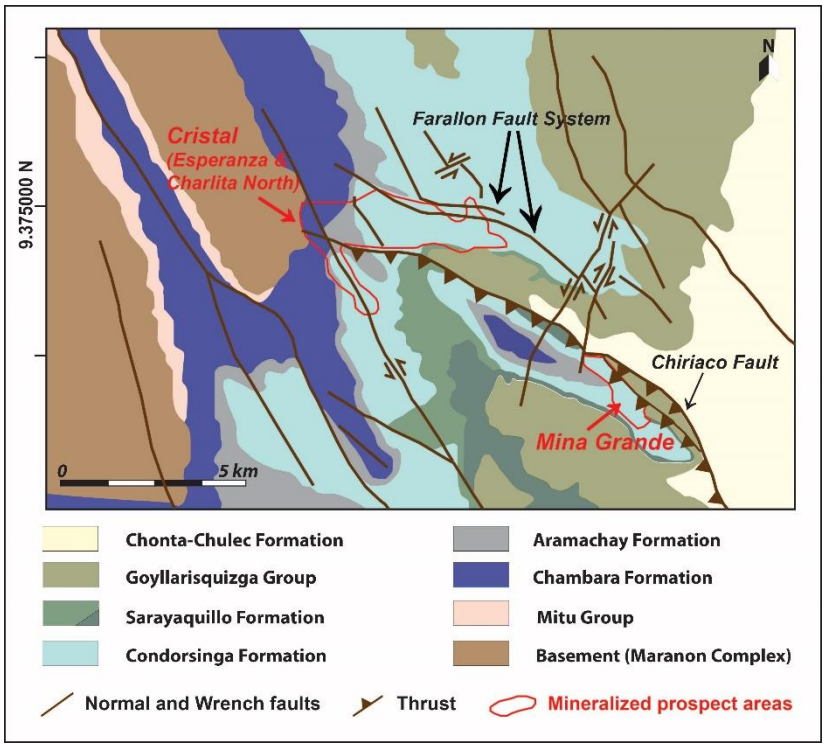

Figure 2.3. Geological map of the study area, Cristal mineralisation, and Mina Grande (modified from Mondillo et al., 2018).

2.1.3.2. Materials and Methods

As shown in Table 2.1, a total of 29 measurements were conducted for Pb isotope compositions (PbIC) using a multi-collector inductively coupled plasma mass spectrometer (MC-ICP-MS).

A total of 14 samples were collected from three drill cores with different depths (CR07: 16.90 to 28.08 m, three samples; CR13: 18.00 to 27.40 m, two samples; CR18: 08.90 to 38.30 m, nine samples) in the Esperanza area, located in the centre of the Cristal property. The distances between the three drill cores were between 16 and 60 m. A total of 19 analyses of smithsonite ($ZnCO_3$), pyrite, sphalerite, and dolostones were conducted from 14 samples.

Five analyses of pyrite, sphalerite, and galena using three outcrop specimens from the Charlita North area, located in the northern part of the Cristal mineralisation and approximately 2 km away from the Esperanza area, were carried out. Five smithsonite samples from the Mina Grande deposit (Fig. 2.3), which is a Zn non-sulfide deposit derived from the weathering of an MVT deposit (Arfè et al., 2017), approximately 8 km away from the Esperanza area, were also analysed to compare the PbIC of the Cristal mineralisation.

The samples were dissolved and eluted Pb using the Sr • Spec™ cation exchange resin (Villa, 2009). Pb isotope analyses were conducted with Nu Instruments™ and Neptune Plus™ MC-ICP-MS in the Laboratory of Isotope Geology at the University of Bern. The detailed procedure is explained in section 2.3.3.2 (ion chromatography) and section 2.3.3.3 (MC-ICP-MS).

2.1.3.3. Result and Discussion

1) Dolomite

The Pb isotopic compositions of six dolostone samples from two areas of the Cristal mineralisation were analysed. These six samples were divided based on the mineralogical study into the earliest dolostone with a fine-grained texture (DST), the second fine dolomite (first hydrothermal dolomite; Dol 1), and the third dolomite with coarse-grained sparry to saddle dolomite (second hydrothermal dolomite; Dol 2). The mineral textures of Dol 1 and Dol 2 indicate that these are typical hydrothermal dolomites, similar to the hydrothermal dolomites in the Florida Canyon sulfide deposit (Basuki et al., 2008; Reid, 2001; Mondillo et al., 2018). Particularly, Dol 2 is present in the veins and open spaces in addition to a host of the sulfide mineralisation in the

study area. The DST and Dol 1 were relatively pure as compared to Dol 2, which has alternating bands of high Fe and Mn contents, even with Zn-rich rims.

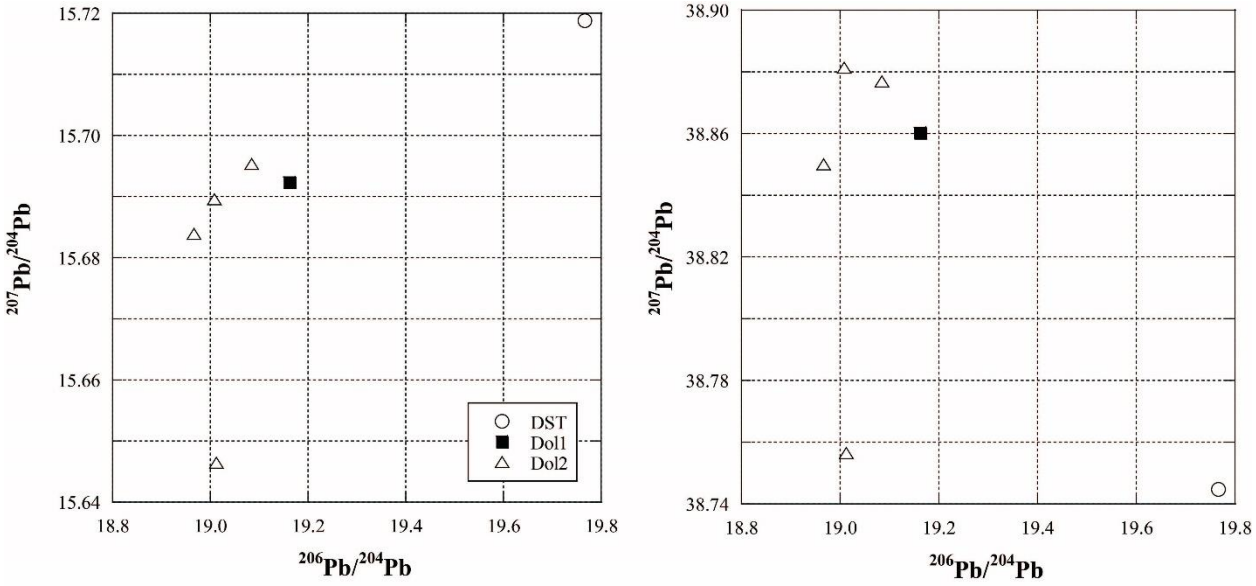

Figure 2.4. Pb isotope correlation diagrams for dolomite samples. (A) $^{207}Pb/^{204}Pb$ vs. $^{206}Pb/^{204}Pb$; (B) $^{208}Pb/^{204}Pb$ vs. $^{206}Pb/^{204}Pb$.

Figure 2.4 shows that the earliest dolostone (DST) has the most radiogenic ratios of $^{206}Pb/^{204}Pb$ and $^{207}Pb/^{204}Pb$; however, it has the least radiogenic ratio of $^{208}Pb/^{204}Pb$. The PbIC of DST is different from those of Dol 1 and Dol 2. The PbIC of Dol 1 and Dol 2 have less radiogenic to uranogenic ratios but more radiogenic to thorogenic ratios than that of DST. The PbIC of Dol 2 is slightly lower than that of Dol 1.

In particular, the Dol 2 in Figure 2.4 has lower $^{207}Pb/^{204}Pb$ and $^{208}Pb/^{204}Pb$ ratios compared to the other three Dol 2. Therefore, the PbIC of this sample can be separated from the PbIC ratios of the other three Dol 2, indicating that the PbIC of Dol 2 is not binary mixing and at least three components of sources are required.

Table 2.1. Sample description with the depth of sample collection from cores and the type of samples analysed in the study (modified from Mondillo et al., 2018).

	Sample No.	Depth	Sample Description	Phases
	Esperanza			
1	CR07-1	16-90-18.55m	(Smithsonite-rich interval hosted in siltsone)	Smithsonite
2	CR07-3	20.20-22.05m	(Smithsonite-rich interval hosted in siltsone)	Smithsonite
3	CR07-7	26.45-28.08m	(Dolostone-limestone, with siltstone interlayers and calcite veins)	Dol2
4	CR13-2	18.00-18.95m	(Smithsonite-rich interval replacing dolomite and sphalerite)	Dol2
5	CR13-9	26.40-27.40m	(Hemimorphite-rich interval, at the boundary between dolomite and siltstone)	DST
6	CR18-4	8.90-10.00m	(Dolostone hosting sphalerite veins partly replaced by smithsonite)	Sphalerite
7		10.00-10.95m	(Dolostone hosting sphalerite and pyrite veins)	Dol2
8	CR18-5	10.00-10.95m	(Dolostone hosting sphalerite and pyrite veins)	Sphalerite A
9		10.00-10.95m	(Dolostone hosting sphalerite and pyrite veins)	Sphalerite B
10	CR18-9	14.70-16.20m	(Smithsonite-goethite-rich horizon)	Pyrite
11	CR18-11	17.65-18.65m	(Smithsonite-goethite-rich horizon)	Smithsonite
12	CR18-12	18.65-19.65m	(Smithsonite-goethite-rich horizon)	Smithsonite
13		21.50-22.70m	(Dolostone hosting sphalerite veins partly replaced by smithsonite)	Dol2
14	CR18-15	21.50-22.70m	(Dolostone hosting sphalerite veins partly replaced by smithsonite)	Sphalerite A
15		21.50-22.70m	(Dolostone hosting sphalerite veins partly replaced by smithsonite)	Sphalerite B
16		21.50-22.70m	(Dolostone hosting sphalerite veins partly replaced by smithsonite)	Pyrite
17	CR18-17	24.00-25.30m	(Dolostone hosting sphalerite veins partly replaced by smithsonite and minor hemimorphite)	Pyrite
18	CR18-18	25.30-26.30m	(Dolostone hosting sphalerite veins partly replaced by smithsonite and minor hemimorphite)	Sphalerite
19	CR18-23	36.70-38.30m	(Oxidized dolomite)	Dol1
	Charlita North			
1	CNBZ	Outcrop	(Dolostone containing sphalerite veins)	Sphalerite A
2		Outcrop	(Dolostone containing sphalerite veins)	Sphalerite B
3	CN	Outcrop	(Dolostone containing sphalerite veins)	Sphalerite A
4		Outcrop	(Dolostone containing sphalerite veins)	Galena
5	ACR	Outcrop	(Dolostone containing pyrite-sphalerite veins)	Pyrite
	Mina Grade			
1	ZA-5			Smithsonite
2	ZA-3			Smithsonite A
3				Smithsonite B
4	ZB-3			Smithsonite A
5				Smithsonite B

*Dol 1 = early hydrothermal dolomite; Dol 2 = late hydrothermal dolomite; DST = diagenetic dolomite.

Table 2.2. Pb isotopic composition of sulfides, dolomite, and smithsonite from the Cristal mineralisation and Mina Grande deposit. Individual error represents run uncertainties at the 95% confidence level (Mondillo et al., 2018).

	Sample No.	Phases	$^{206}Pb/^{204}Pb$	2σ	$^{207}Pb/^{204}Pb$	2σ	$^{208}Pb/^{204}Pb$	2σ	$^{207}Pb/^{206}Pb$	2σ	$^{208}Pb/^{206}Pb$	2σ
	Esperanza											
1	CR07-1	Smithsonite	18.9163	0.0010	15.6709	0.0011	38.8605	0.0040	0.82843	0.00003	2.05429	0.00013
2	CR07-3	Smithsonite	18.9946	0.0016	15.6871	0.0016	38.9361	0.0052	0.82588	0.00003	2.04995	0.00012
3	CR07-7	Dol2	19.0083	0.0005	15.6896	0.0005	38.8814	0.0015	0.82541	0.00001	2.04550	0.00004
4	CR13-2	Dol2	19.0126	0.0203	15.6465	0.0175	38.7565	0.0458	0.82296	0.00020	2.03847	0.00096
5	CR13-9	DST	19.7667	0.0026	15.7188	0.0013	38.7446	0.0062	0.79519	0.00008	1.96013	0.00021
6	CR18-4	Sphalerite	18.9735	0.0006	15.6895	0.0006	38.9267	0.0021	0.82691	0.00001	2.05159	0.00005
7	CR18-5	Dol2	18.9665	0.0015	15.6839	0.0015	38.8500	0.0044	0.82693	0.00003	2.04835	0.00011
8		Sphalerite A	19.2611	0.0011	15.7945	0.0009	39.8142	0.0064	0.82002	0.00003	2.06725	0.00008
9		Sphalerite B	19.0043	0.0039	15.6970	0.0035	38.8827	0.0101	0.82596	0.00005	2.04596	0.00020
10	CR18-9	Pyrite	18.9537	0.0089	15.6690	0.0069	38.8622	0.0228	0.82668	0.00002	2.05055	0.00008
11	CR18-11	Smithsonite	18.9639	0.0027	15.6904	0.0022	38.9386	0.0056	0.82736	0.00002	2.05332	0.00009
12	CR18-12	Smithsonite	19.1209	0.0050	15.7540	0.0040	39.2392	0.0112	0.82397	0.00007	2.05225	0.00023
13	CR18-15	Dol2	19.0848	0.0015	15.6953	0.0010	38.8769	0.0077	0.82238	0.00002	2.03718	0.00007
14		Sphalerite A	18.9754	0.0006	15.6908	0.0006	38.9223	0.0018	0.82690	0.00001	2.05120	0.00004
15		Sphalerite B	19.0282	0.0033	15.7089	0.0029	39.0195	0.0116	0.82556	0.00005	2.05082	0.00015
16		Pyrite	18.9841	0.0010	15.6870	0.0011	38.9232	0.0039	0.82632	0.00002	2.05036	0.00008
17	CR18-17	Pyrite	19.2234	0.0006	15.9862	0.0007	39.9156	0.0021	0.83161	0.00001	2.07640	0.00006
18	CR18-18	Sphalerite	19.0143	0.0037	15.6911	0.0039	38.9139	0.0118	0.82523	0.00006	2.04656	0.00029
19	CR18-23	Dol1	19.1633	0.0014	15.6924	0.0014	38.8602	0.0048	0.81888	0.00002	2.02791	0.00009
	Charlita North											
1	CNBZ	Sphalerite A	18.8279	0.0009	15.6868	0.0008	38.7403	0.0047	0.83317	0.00002	2.05768	0.00011
2		Sphalerite B	18.9175	0.0012	15.6995	0.0010	38.8867	0.0030	0.82991	0.00002	2.05558	0.00008
3	CN	Sphalerite A	18.8034	0.0009	15.6696	0.0008	38.6298	0.0027	0.83333	0.00001	2.05445	0.00006
4		Galena	18.7531	0.0012	15.6604	0.0011	38.5409	0.0033	0.83509	0.00002	2.05519	0.00008
5	ACR	Pyrite	18.8166	0.0027	15.6696	0.0025	38.7005	0.0062	0.83273	0.00003	2.05677	0.00008
	Mina Grade											
1	ZA-5	Smithsonite	18.9160	0.0012	15.6799	0.0014	38.8530	0.0088	0.82891	0.00004	2.05395	0.00022
2	ZA-3	Smithsonite A	18.9071	0.0017	15.6779	0.0019	38.8423	0.0116	0.82920	0.00010	2.05440	0.00034
3		Smithsonite B	18.9360	0.0010	15.6785	0.0011	38.8482	0.0070	0.82796	0.00004	2.05154	0.00014
4	ZB-3	Smithsonite A	18.9600	0.0012	15.6821	0.0011	38.8571	0.0072	0.82713	0.00004	2.04949	0.00018
5		Smithsonite B	18.9373	0.0014	15.6783	0.0016	38.8477	0.0092	0.82791	0.00006	2.05145	0.00018

*Dol 1 = early hydrothermal dolomite; Dol 2 = late hydrothermal dolomite; DST = diagenetic dolomite.

2) Sulfides and Smithsonite

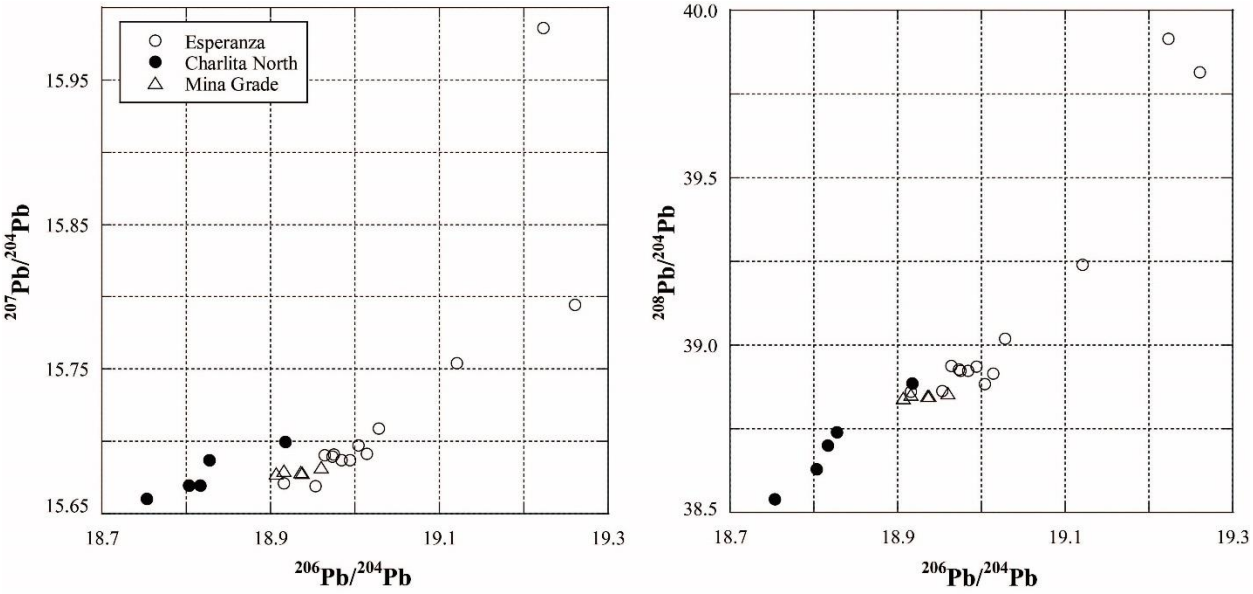

Figure 2.5. Pb isotope correlation diagrams for sulfide and smithsonite samples. (A) $^{207}Pb/^{204}Pb$ vs. $^{206}Pb/^{204}Pb$; (B) $^{208}Pb/^{204}Pb$ vs. $^{206}Pb/^{204}Pb$.

As Pb isotopic composition is not fractionated by redox reactions in solution or by fluid-mineral interactions (Macfarlane and Petersen, 1990), the Pb isotopic compositions of smithsonite are similar to its sources such as other sulfides (Fig. 2.5). The Pb isotope compositions of sphalerite and pyrite from the drill cores of the Esperanza area are similar to those of Dol 2, indicating the association between Dol 2 and sulfide mineralisation and corresponding mineral observation, where the sphalerite in open spaces and geodes within Dol 2 postdate the Dol 2 dolomite. In addition, the Pb isotopic compositions of DST show different ratios as compared to those of sulfides, indicating that the DST is not related to the hydrothermal sulfide mineralisation in the study area.

As shown in Figure 2.5, the Pb isotopic compositions of sulfides from the three different areas (Esperanza and Charlita North from the Cristal property and the Mina Grande deposits) indicate that the Pb isotopic ratios of the five sulfides from the Charlita North area are less radiogenic than those from the Esperanza drill cores. In particular, they do not form one cluster, thus requiring at least two distinct hydrothermal pluses in the broader Cristal mineralisation.

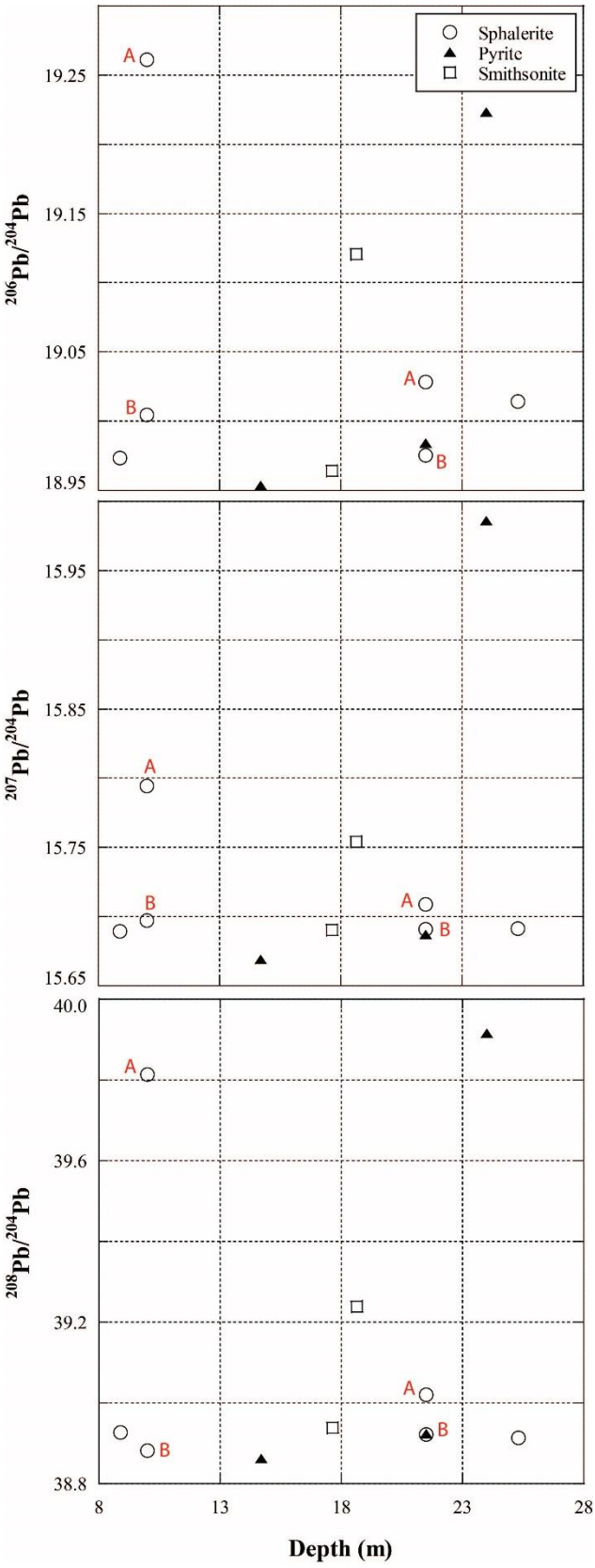

Figure 2.6. Pb isotope correlation diagrams for the samples from the CR18 drill core of sulfides and smithsonite at different depths. (A) $^{206}Pb/^{204}Pb$; (B) $^{207}Pb/^{204}Pb$; and (C) $^{208}Pb/^{204}Pb$ vs. depths.

The Pb isotopic compositions of the five smithsonite samples from the Mina Grande deposit are located in the middle of the entire range of sulfide Pb isotope compositions in the Cristal mineralisation, between the Esperanza and Charlita areas (Fig. 2.5).

The average Pb isotope compositions of smithsonite from the Cristal mineralisation are similar to those of sphalerites as well as to those of smithsonite from the Mina Grande deposit.

In particular, the sulfide samples from two drill cores (CR07 and CR18) are heterogeneous, approximately 20 times greater than the uncertainties of each analysis, suggesting that they are not the results of only binary mixing, and require three or four sources, as shown in both Pb isotope plots. Importantly, each area has a different linear trend of binary or ternary (or quaternary) mixing.

The PbIC of the samples from different depths in the same drill core (e.g. CR18; Fig. 2.6) shows the spatial correlation of the depths. Interestingly, PbIC variations were observed in two sphalerite sample sets (Fig. 2.6: Sph A and Sph B) collected from the drill cores at 10–10.95 m and 21.5–22.7 m depths, respectively,

and an even outcrop specimen (CNBZ) (Table 2.1; Fig. 2.6). In addition, there is no correlation based on the mineral phases (Sph, Py, smithsonite), showing the same PbIC between Py and Sph in the CR18-15 sample.

The Pb isotopic compositions of the samples and literature on the Pb evolution model (Kramers and Tolstikhin, 1997) suggest that the variation in Pb is a mixture of an old upper crust (OUC)-like sources such as the crustal basement and old uranium (U)-bearing rocks in Peru and a young upper crust (YUC)-like source such as the Middle to Late Triassic rift-related volcanic rocks that occurred in the Pucara Group. The Pb isotopic composition of one pyrite sample shows more radiogenic values than the OUC curve in the Pb evolution model (Fig. 2.7), indicating that there is an additional source in the system.

From observations of Pb isotope compositions in the samples from the Cristal mineralisation, we can conclude that the sources of Pb (and/or metals) are not well defined, indicating that complicated processes lead to the formation the Cristal mineralisation in space and time.

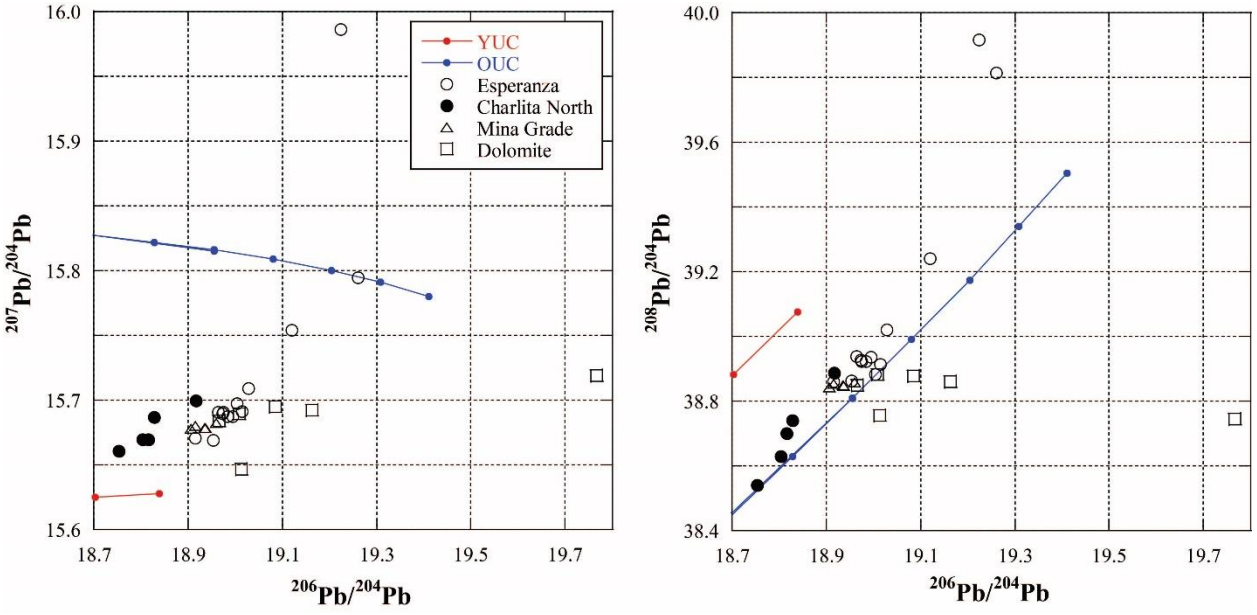

Figure 2.7. Pb isotope correlation diagrams plotted in the Pb evolution model (Kramers and Tolstikhin, 1997). (A) $^{207}Pb/^{204}Pb$ vs. 206Pb/204Pb; (B) $^{208}Pb/^{204}Pb$ vs. $^{206}Pb/^{204}Pb$ (*YUC = Young Upper Crust; OUC = Old Upper Crust; UM = Upper Mantle).

2.1.3.4. Motivation for the Main Project

The isotopic evolution of Pb over the history of Earth has been studied for almost a century. The first quantitative model that accurately matched the age of the Earth and average isotopic composition was proposed by Holmes (1946), Houtermans (1946; 1953). This evolutionary model was strongly simplified, as it assumed that Earth evolved from a single closed reservoir. The vast number of regionally distinct differentiation events that occurred on Earth was considered by Kramers and Tolstikhin (1997), who greatly improved Stacey and Kramers' (1975) single-differentiation model, which they admitted as incorrect.

A common feature of all terrestrial Pb models is that the hundreds of supposedly "conformable lead" points (mostly galena) scatter unsystematically around any of the best-fit curves of the models. This should not happen in models of terrestrial evolution based only on magmatic differentiation, as Pb in sulfide minerals (devoid of U and Th) should freeze in the Pb isotopic composition of the crustal segment, from which the ore deposits are formed to which no radiogenic Pb was added after the sulfide phases crystallised. However, even when the samples pertain to a limited range in space and time (such as minerals of the same mining district), they display resolvable Pb isotopic variations (see Mondillo et al., 2018, and references therein). It is possible to discover Pb heterogeneity in the restricted area because we can accurately measure PbIC with very low uncertainties.

These variations are second-order effect, superimposed on the first-order global trajectory (Kramers and Tolstikhin, 1997) and can be qualitatively explained by noting that crustal orebodies are not formed instantly (Weis et al., 2012) as hydrothermal systems are driven by thermal anomalies (e.g. of a cooling pluton). The time scale for cooling the fluid-saturated aureole around a shallow pluton can range from a few tens of ka (Krumrei et al., 2006) to a few Ma when there are multiple intrusive phases (Villa et al. 2006, Farina et al. 2018). During this time, redox conditions may change (Mondillo et al., 2014) or fluids from various sources may interact with the wall rocks. It might be expected that the isotope record of various ore minerals in a given orebody could be detectably different based on divergent interactions with country rocks, as oxidising and reducing fluids have different histories.

The purpose of our study was to explore the Pb isotopic homogeneity in a deposit in which the genetic conditions were as uniform as possible. We chose the Janggun Pb-Zn-(Ag) mine (South

Korea), in which sulfides are the main ore minerals. In the region of the Janggun mine that we sampled, there is no record of transition to oxidising conditions, unlike ore deposits (e.g. Mondillo et al., 2018) in which heterogeneous Pb isotopic compositions may be linked to large redox variations.

At the regional scale, the Pb isotopic compositions of a large number of deposits in South Korea have been reported by several researchers (Jeong et al., 2012; So et al., 1991; Park and Chang, 2005; Chung and Park, 2006; Chang et al., 1995a; Chang et al., 1995b; Mabuchi et al., 1985; Sasaki, 1987). Most of these Pb isotopic studies focused on first-order discrimination of fluid provenances and source fingerprinting and analysed only a few samples from each mine without an ad-hoc search for second-order effects. The present study focusses on ore-forming processes by using closely spaced sampling and by comparing Pb and S isotopic compositions of sulfide phases.

2.2. Geological Setting

2.2.1. Location and Geology of the study area—Janggun mine

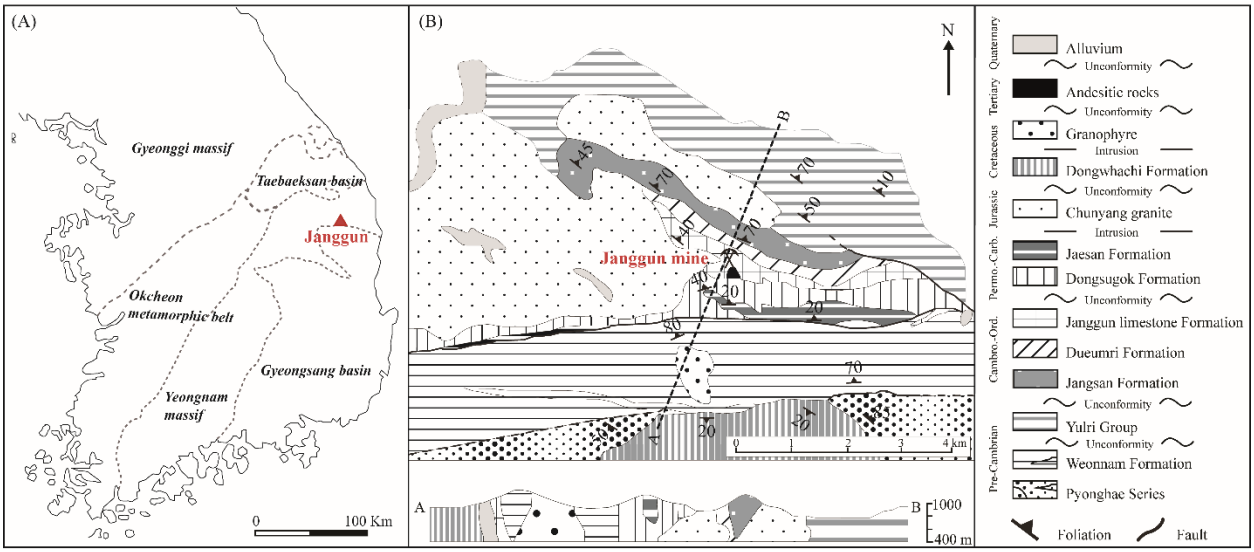

Figure 2.8. (A) Simplified map of South Korea, showing the location of the study area, Janggun mine, and four major provinces in South Korea; (B) Geological map of the Janggun mine with the cross-section from A to B (modified after Lee et al., 1990; Yoo, 2012; Jeong et al., 2012).

As the geology of South Korea has been explained in detail in Chapter 1, Figure 2.8(A) shows the country divided into four provinces: Gyeonggi massif (Neoarchean to Paleoproterozoic

massif), Okcheon belt (further subdivided into the Okcheon metamorphic belt and Taebaeksan basin; Neoproterozoic to Palaeozoic fold belt), Yeongnam massif (Neoarchean to Paleoproterozoic massif), and Gyeongsang basin (Cretaceous to Palaeogene arc system) (Jeong et al., 2012, Chough and Sohn, 2010).

The Janggun mine is located in the Socheon-myeon, Bonghwa-gun, Gyeongsangbuk-do, South Korea, at approximately 36°51' N and 129°04' E, which corresponds to the southern part of the Taebaeksan metallogenic belt (the north-eastern margin of the Yeongnam massif) (Imai et al., 1980). Even though most of the economically significant Pb-Zn mines in South Korea have been mined out or are closed since 1994, the Janggun mine produces small amounts of Pb-Zn ores (Lee, 2015). Figure 2.8(B) shows the regional geology of the Janggun mine area, which consists of basement rocks, a sequence of metasedimentary rocks, Dongsugok Schist Formation, and the Jaesan Coal-bearing Formation (Imai and Lee, 1980; Lee et al., 1990).

The Precambrian Weonnam and Yuli groups, which comprise gneiss and schist complexes, (metasedimentary rocks) are basement rocks in the Janggun mine. It underlies the Cambro-Ordovician sequence of approximately 2500 m thick sedimentary rocks, primarily representing the Jangsan Quartzite Formation, Dueum-Ri Schist Formation, and Janggun Limestone Formation in ascending order. The Cambrian Jangsan Quartzite Formation is a basal unit of this sedimentary sequence that corresponds to the Joseon Supergroup in Taebaksan Basin province (Hwang and Reedman, 1975; Imai et al., 1980; Imai and Lee, 1980; Lee et al., 1990).

The Janggun mine has been emplaced into the 100–800 m thick Janggun Limestone Formation, which consists of dolomitic limestone and calcareous limestone in the southern and northern parts of the mine, respectively. The Permo-Carboniferous Dongsugok Schist Formation and the Jaesan coal-bearing Formation, which corresponds to the Pyeongan Supergroup, unconformably rests on the Cambro-Ordovician sequence (Imai and Lee, 1980; Lee et al., 1990; Lee et. al., 1998). These rocks have been subjected to the Chunyang Granite (or apophyses of the Chunyang Granite), which spreads out in the mine area (widely exposed in the west of the mine). This was caused by the Daebo orogeny event of the late Jurassic period and resulted in the folding and faulting of the sequences with the metamorphic grade of low greenschist to lower amphibolite facies (Lee et al., 1990; Lee et al., 1998). Dyke swarms of andesitic rocks are scattered in the mine area along with granophyre, intruding into the Precambrian Weonnam group (Lee et al., 1990; Lee

et al., 1996b). These rocks are probably genetically associated with the Cretaceous subvolcanism corresponding to the Bulguksa orogeny event (approximately 110–50 Ma).

In particular, the Janggun mine is hosted at the contact between the Janggun Limestone Formation and the Chunyang Granite plutons. The orebodies in the Janggun mine are distributed in the fractures in carbonate rocks and irregular intrusive contracts of the granitic rocks (Imai and Lee, 1980). The Chunyang Granite, therefore, played an important role by acting as sites of emplacement of the orebodies in the Janggun mine, although it is not the related igneous rock (source rock) of the Janggun mine.

2.2.2. Characteristics of Janggun Mine

Four distinct deposits are present in the Janggun mine and they have been studied by several researchers (Kim 1970; 1979; Imai et al. 1980; Ahn and Lee 1995; Imai and Lee 1980; Lee et al. 1990; Lee et al. 1996a, b): supergene manganese oxides, vanadium-bearing quartzite, Pb-Zn-(Ag) deposits, and skarn-type iron deposits. This strongly suggests that various types of ore mineralization occurred in this restricted space due to changes in the genetic conditions (including redox variations). The details of each deposit are described below.

2.2.1.1. Manganese deposit

The manganese (Mn) oxides on the surface were the first to be mined in 1941. The mining lasted for around 30 years, and Janggun mine was the largest producer of Mn ores in South Korea, with a yearly production of 3000 tons of Mn crude ores (30%–35% of Mn) (Imai and Lee, 1980). Janggunite ($Mn_{5-x}(Mn, Fe)_{1+x}O_8(OH)_6$), which is a rare Mn oxide mineral, was first observed in the Janggun mine and, hence, was named after the mine (Kim, 1970; 1979). The Janggun Limestone Formation hosted the Mn deposits along the dolomite bedding and was adjacent to the Chuyaing Granite. Manganese ore deposits in the Janggun mine are categorised into two types based on different genesis and mineralogy characteristics: hypogene and supergene (Kim, 1970; Imai and Lee, 1980). The hypogene Mn deposit primarily consists of Mn carbonates with small amounts of Mn silicates and sulfide minerals. This hydrothermal ore is rarely observed on the surface and includes a Mn-breccia pipe with carbonate fragments and cementing rhodochrosite ($MnCO_3$), indicating an increase in Mn in the system (Kim, 1970). The supergene Mn deposit is

mainly composed of Mn oxides with small concentrations of manganoan calcite, quartz, and sericite. Since these Mn oxides result from the supergene oxidation and enrichment of the former rhodochrosites and other manganiferous carbonates, the Mn oxide ores are generally placed on or in the hypogene minerals (Kim, 1970; Imai and Lee, 1980).

2.2.1.2. Vanadium-bearing quartzite deposit

As mentioned in section 2.2.1, a basal unit of the Cambro-Ordovician sequence of sedimentary rocks in the Janggun mine area is the Jangsan Quartzite Formation with a thickness of 50–200 m, consisting of compact cliff-forming white grey or brown micaceous quartzite (Imai et al., 1980). The Jangsan Quartzite Formation is dominantly exposed on the northern ridge of the Janggun Valley, striking nearly EW with a steep dip of 80° to 85° and unconformably underlying and occurring adjacent to the Precambrian Yuli Group (Imai et al., 1980; Lee et al., 1998).

Two modes of muscovite occurrence have been observed in the Formation, comprising of deep-green and pale-green muscovites. The former, containing around 5%–8% of V_2O_3, are present in the bottom part of the Jangsan Quartzite Formation and are absent in other Formations, suggesting that vanadium and chromium are the primary constituents and originate from the basement meta-sediments during the initial stage of Cambro-Ordovician marine-transgression, whereas the latter contains around 1%–3% of V_2O_3 (Imai et al., 1980; Ahn and Lee, 1995). In addition, the V_2O_3 content in muscovite decreases with increasing Al (Al^{6+}), suggesting the substitution of vanadium and octahedral Al in the muscovite (Imai et al., 1980; Ahn and Lee, 1995).

2.2.1.3. Iron deposit

The iron (magnetite) deposit was most recently discovered in the Janggun mine and is embedded in the Janggun Limestone Formation, between the dolomitic limestone of the Janggun Limestone Formation and the Dongsugok Formation, which are in contact with the Chunyang Granite (Lee et al., 1996a; 1996b; Lee et al., 1998). These massive orebodies with a layered structure consist of two main lens-shaped bodies (approximately 300 m long and 30 m wide), striking N70°W, dipping 50° NE, and having small parallel bodies (Lee et al., 1998).

The magnetite deposit was formed by two distinct mineralisation stages based on the mineralogy, genetic ages, and textural relations: skarn stage and hydrothermal replacement stage.

The orebody from the earlier skarn stage is situated in the deeper part, approximately 320–410 m below the surface, whereas the hydrothermal orebody of the later stage occurs in the shallow part, approximately 96–160 m below the surface of the mine (Lee et al., 1996a; 1996b; Lee et al., 1998). The alteration products (i.e. sericite) of the two stages were dated, indicating two distinct Cretaceous ages of 107 and 70 Ma for the skarn and hydrothermal stages, respectively (Lee et al., 1998). The minerals resulting from the hydrothermal replacement process is restricted to the shallow level of orebodies, implying the paragenetic time of the mineralisation (Lee et al., 1996a; 1996b; Lee et al., 1998).

The minerals of the skarn stage are composed of magnetite, Mg-Fe carbonates, and Mg- and Ca-skarn minerals, with a small concentration of base-metal sulfides. This stage is characterised by the abundant occurrence of magnetite ores with haematite and pyrrhotite, which occurred in massive, banded, and mixed textures. In addition, the skarn stage minerals are divided into two groups: early-stage massive magnesian skarn and late-stage intermediate to calcic vein skarn. The former skarn mainly comprises of forsterite, chlorite, chondrodite, apatite, and ferro-magnesian carbonates, and indicates that the fluid compositions were progressively changed by reactions with dolomitic limestone and host rock. The intermediate to calcic skarn occurred during the hydrous destruction of the former skarn anhydrous assemblage and consists of diopside, calcic-amphibole, and grandite, with small amounts of wollastonite (Lee et al., 1996a; 1996b; Lee et al., 1998).

The minerals of the hydrothermal stage are characterised by productive Pb-Zn mineralisation, consisting primarily of galena, pyrite, arsenopyrite, and sphalerite, which form massive replacement bands within the dolomitic limestone, as well as minor amounts of stannite, tetrahedrite, boulangerite, and bournonite (Lee et al., 1996a; 1996b; Lee et al., 1998).

2.2.1.4. Lead-Zinc (-Silver) deposit (study area)

As various types of ore mineralisation occur in the Janggun mine, we intentionally limited our study to one of the four genetic environments, the Pb-Zn-(Ag) deposit, which was found in 1976 under the Mn deposit in the Janggun mine. This Janggun Pb-Zn-(Ag) deposit has been one of the main producers of Pb and Zn ores in Korea. The cumulative production from 1977 to 2001 was 251759 tons of Zn, 137731 tons of Pb, and 134 tons of Ag (Choi et al., 2009). A small part of

the mine was recently reopened to produce Pb and Zn; however, most parts remain closed. The average grade was 5.5% Pb, 5.0% Zn, 0.2% Cu, 100 g/ton Ag, and 1 g/ton Au (Imai and Lee, 1980).

The Pb-Zn-(Ag) deposit is a hydrothermal carbonate replacement deposit in origin, which is characterised by hydrothermal metasomatic alteration, including Mn enrichment of carbonate rocks, dolomitization, sericitization, silicification, chloritization, and argillic alteration (Imai and Lee, 1980).

This deposit in the Janggun Limestone Formation consists of massive limestone, dolomitic limestone, and dolomite rocks with some intercalation of siliceous and muddy carbonate rocks, especially along the immediate contact with the Chunyang Granite. Granite played a significant role in structurally restricting and controlling the site for mineralisation by fractures and fissure in the host rock and irregular contacts of the granites (apophyses of the Chunyang Granite. In addition, breccia ores occur in places that experience brecciation by faults. The polymetallic mineralisation in the Pb-Zn-(Ag) Janggun deposit yields massive and disseminated breccia, and vein types of ores, primarily including sphalerite, galena, pyrrhotite, pyrite, and arsenopyrite with minor amounts of chalcopyrite, bournonite, boulangerite, minerals of tetrahedrite-freibergite series, and gangue minerals such as manganese carbonate (i.e. rhodochrosite and magnesian kutnohorite) and quartz.

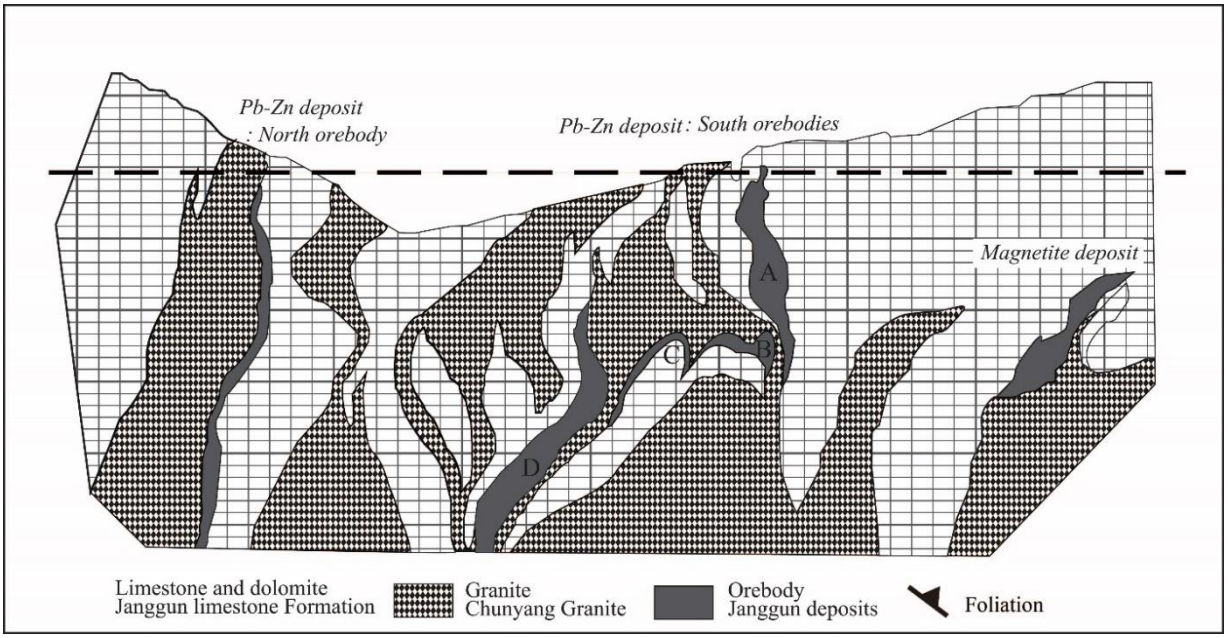

Figure 2.9. Simplified cross-section of the geology of five Pb-Zn orebodies and magnetite orebody in Janggun mine area, indicating the 591 m level, from where the samples were collected (modified after Lee et al., 1990).

The Pb-Zn-(Ag) deposit in the Janggun mine consists of five orebodies, the South orebodies (four orebodies: A, B, C, and D) and the North orebody, based on the spatial distribution in the mine area (Fig. 2.9). The chimney-shaped South A orebody is located in the southernmost part of the deposit and was first developed in the Pb-Zn(-Ag) Janggun deposit, suggesting that it is a principal deposit as the top of the orebody is exposed on the surface. Its diameter is approximately 30 m (maximum) and extends approximately 150 m under the main adit level, which is 591 m above the sea level. The South B and C orebodies are separated by the A orebody and they occur 60 m below (i.e. concealed orebody) the main adit level. The lens-shaped South D orebody is also separated from the other orebodies and extends approximately 150 m. The columnar-shaped North orebody is steeply dipped and separated from the South orebodies by approximately 400 m (Imai and Lee 1980; Lee et al. 1990).

The country rocks near the Pb-Zn-Ag orebody and the sericite mineral, which is a product of hydrothermal alteration assuming that the age of the sericite indicates the Pb-Zn(-Ag) mineralisation, were dated. The sericites date back to 71.0 Ma and 73.6 Ma (Lee et al., 1998); Chunyang granite dates to 133 Ma (Kim, 1971) and 148.5 Ma (Lee et al., 1998); granophyre corresponds to 77.9 Ma (Lee et al., 1998); and andesitic dyke corresponds to 58.9 Ma (Lee et al., 1998), indicating that it was the youngest rock in the mine. This suggests that the granophyre is probably the related igneous rock for the Pb-Zn(-Ag) deposit with the most similar age. However, the related intrusion and sources of these metals are still not clear.

2.3. Samples and analytical methods

2.3.1. Sample collection

A total of 13 ore rock samples were collected from two different orebodies (North orebody and South A orebody) among the five orebodies of the Pb-Zn-(Ag) deposit at the 591-m level adit in the Janggun mine (Fig. 2.9). We mostly focus on the 12 samples from the North orebody. One sample from the South A orebody was collected to compare microscopic and chemical characteristics of samples between the North and South A orebodies. As shown in the underground map of the 591-m level of the North orebody (Fig. 2.10), we systematically collected 12 samples

from every 10 to 20 m to account the (possible) spatial heterogeneities in the Pb isotopic compositions.

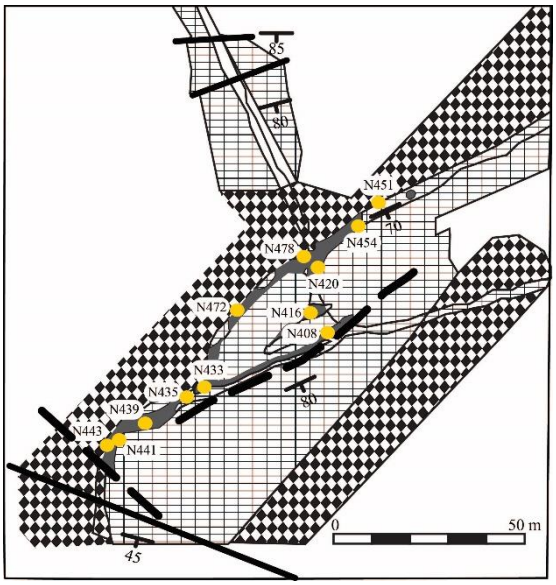

Figure 2.10. Underground geological map of the main adit level (591 m) of the North orebody with sampling locations marked with filled yellow circles (modified after Lee et al., 1990).

2.3.2. Microscopy and mineral chemical study

The collected ore samples were cut into two specimens: a thin section and a thick section. Polished thin sections (approximately 30 μm thick) were prepared for optical microscopy under reflected light to observe the textures of sulfide phases and gangue minerals as well as to use in an electron probe X-ray microanalyzer (EPMA). Detailed ore microscopy observations of the thin sections were conducted prior to other analyses.

We conducted EPMA on the thin sections on a JEOL 8200 at the Institut für Geologie, University of Bern. The operating conditions of the EPMA were 15 kV, 10 nA, and 10 μm beam diameter. Twelve elements (S, Cu, Fe, Zn, Mn, As, Pb, Cd, Ag, Ni, Co, and Sb) were chosen for the analysis of sulfide phases. The standard phase and the type of crystal used are as follows: arsenopyrite (As: TAP), pyrite (S: PETL and Fe: LIFH), galena (Pb: PETL), covellite (Cu: LIFH), sphalerite (Zn: LIFH), albite (Mn: PETL), greenockite (Cd: PETH), pyrargyrite (Ag: PETH and Sb: PETH), skutterudite (Co: LIFH), and bunsenite (Ni: LIFH). The crystals were selected based on the X-ray intensity and diffraction efficiency.

2.3.3. Sample preparation for Pb isotope analysis

2.3.3.1. Sulfide extraction by micro-drilling on thick sections

The polished thick sections (approximately 0.5 cm thick) were prepared to collect individual mineral powders by micro-drilling, using an ESI New wave Micromill at Institut für Geologie, University of Bern. First, we identified the areas of interest under a reflected-light microscope to avoid visible inclusions of extraneous phases or to identify the involvement of the inevitable inclusions in the interest area. The thick sections were not used for EPMA as carbon-coating, which is necessary for EPMA, can possibly contaminate samples as a collecting powder for Pb and S isotope analyses.

The most important step of the micro-drilling method is avoiding Pb contamination during each step of the drilling. The contamination mostly arises from drill bits of the machine and includes a mixture of both the drill bit material and the remaining sample powder (cross-contamination between all sulfide extractions). The following rinsing step was followed to avoid the contamination. After extraction of sulfide powder from the thick sections, the drill bits were repeatedly cleaned with Milli-Q (ultrapure water; obtained from Millipore Corporation, characterised in terms of resistivity; 18.2 MΩ·cm at 25 °C) for 5 min in an ultrasonic bath and dried in the air before the next sample collection. This micro-sampling allows the in-situ extraction of the sample with a resolution of 200 μm to 1 mm, and this resolution of sampling was based on the Pb contents of different phases (e.g. in situ resolution of pyrite is approximately 1 mm, whereas that of PbS is less than 200 μm). In this experiment, the minimum amount of Pb required by MC-ICP-MS to analyse Pb isotope composition was approximately 40 ng. Thus, we collected PbS, ZnS, pyrite, arsenopyrite, and pyrrhotite between 0.3 mg and 2.5 mg.

2.3.3.2. Resin chromatography

Horwitz et al. (1992) reported that the strontium-selective resin, which is comprised of a macrocyclic polyether in 1-octanol, is useful for eluting pure Pb fractions. In addition, a wide range of solution conditions, from diluted nitric acid (0.01 M) to high nitric acid, can retain Pb. Horwitz et al. (1992; 1994) indicated that a variety of reagents can be used for Pb stripping. Villa (2009) developed a procedure for Pb purification using Eichrom's Sr-Spec^{TM} cation exchange resin (100–150 μm) based on the study of Horwitz et al. (1992). The solid resin was supplied in bottles by

TRISKEM International. We followed the procedure of Villa (2009) for sulfide samples, according to which small amounts of powder samples (between 1 and 2 mg) were collected. The customised PTFE mini-columns with a 3-mm diameter, developed at the Institute of Geological Sciences, University of Bern, were used for Pb separation. The height/width ratio of the columns was approximately 4 and the reservoir volume of the column was 1 mL.

Because sulfide phases are highly soluble in nitric acid solution, 2 mL of 14 M HNO_3 solution was used for the complete dissolution of the micro-drilled sulfide powders in closed Savillex PFA vials placed overnight on a hotplate at 100 °C. After digestion of the sulfide powder, we dried them on a hot plate. The dried dissolution samples were mixed with 0.5 mL of 1 M HNO_3 for chromatography. It was not required to conduct resin chromatography on galena (PbS) for Pb elution. Thus, galena was excluded from the whole procedure, which is described below in detail.

First, the mini-columns were washed with 0.01 M HCl and Milli-Q to remove traces of Pb from the column. Approximately 200 µL of Sr-Spec™ cation exchange resin (the amount of Sr-Spec™ cation exchange resin depends on the density of the mixture of the Sr-Spec™ cation exchange resin and 0.01 M HNO_3) was filled in the column. The resin in the column was washed with 3 mL of 0.01 M HCl to remove traces of Pb from the resin. The resin was conditioned with two reservoirs of 1 M HNO_3 before sample solutions were loaded into the column. Sample solutions (0.5 mL) were loaded into the conditioned resin. Five reservoirs of 1 M HNO_3 were used to wash out the matrix constituents of sulfide samples, whereas concurrently, Pb was retained on the resin. Finally, the stripping of Pb was conducted with 2 mL of 0.01 M HCl and it was dried on a hotplate at 100 °C. After drying the stripped solution, we added 2–3 drops of 6 M HCl and 7 M HNO_3 and dried them again to remove possible organic materials.

The Pb-purified samples were mixed with 1.5 mL of 0.5 M nitric acid for mass spectrometry. Except for galena, none of the other sulfide phases was diluted to measure Pb isotope composition as they had sufficient Pb concentration for a single analysis only. As mentioned, galena (PbS) was not required to be purified for resin chromatography and only required dilution after the complete dissolution for analysis using MC-ICP-MS. All dilutions were conducted using 0.5 M HNO_3.

2.3.3.3. MC-ICP-MS

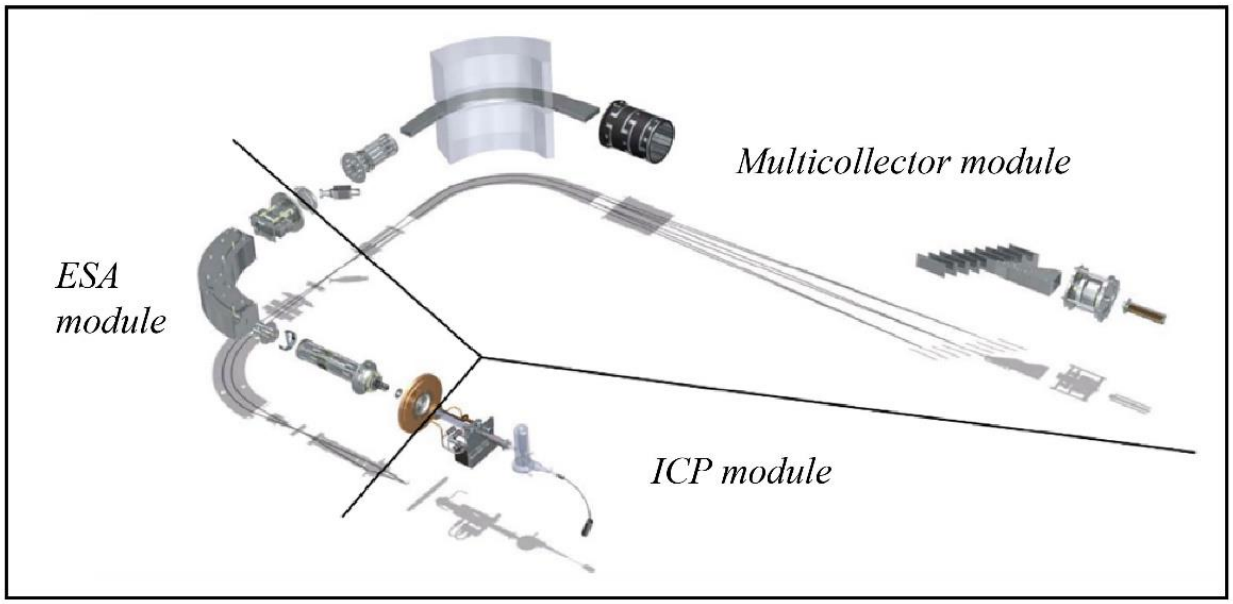

Figure 2.11. Neptune components and functions of each module (modified from Scientific, T. F., 2009).

As shown in Figure 2.11, the Neptune ICP-MS is included in three main modules. The sample solutions were introduced and ionised in plasma, which has temperatures greater than 8000 °C in the ICP module of the instrument. Then, the ions were focussed and accelerated using the transfer lens system and electrostatic analyser (ESA). Finally, the ions were separated based on the ion energy and mass in a magnetic sector and detected by Faraday cups or ion counting detectors. The analyses were conducted on a Neptune Plus™ MC-ICP-MS at the Institut für Geologie, University of Bern.

For thermal ionization mass spectrometry (TIMS), the largest mass fractionation occurs while the samples loaded on a filament surface are evaporated and ionized because lighter isotopes are more volatile than heavier isotopes which have stronger bonds (Urey, 1947). This indicates that factors such as the chemical properties of ions, the number of samples, filaments, and ionisation temperatures play a key role in mass discrimination of TIMS. According to the procedure of ICP-MS briefly explained above, all elements are ionised in ICP-MS. Therefore, the ionisation efficiency was almost 100%. However, large isotope fractionation arises because the lighter ions are inefficiently focussed and accelerated into the mass analyser.

Among the four Pb isotopes, only ^{204}Pb is a non-radiogenic Pb, whereas the other three, ^{206}Pb, ^{207}Pb, and ^{208}Pb, are radiogenic isotopes formed from U and Th. This means that the instrumental mass fractionation cannot be corrected with the observed fractionation of a natural invariant ratio such as Sr (e.g. ^{86}Sr/^{88}Sr = 0.1194). Thus, to monitor the mass fractionation while we analysed the Pb isotope composition of our samples, we employed external normalisation to thallium (Tl), which has been studied and tested by several researchers (Longerish et al., 1987; 1993; Hirata, 1996; Belshaw et al., 1998; Rehkämper and Halliday, 1998; White et al., 2000; Rehkämper and Mezger, 2000). Thallium (Tl) is a suitable element as it has a mass similar to Pb and its two isotopes, ^{203}Tl and ^{205}Tl, do not interfere with any of the Pb isotopes. In addition, ICP-MS depends on the mass of the ion and not on the chemical properties of the ions. Thus, we determined the mass bias by considering Tl as an internal isotope standard; the constant ratio of Tl isotopes was obtained from the National Institute of Standards and Technology (NIST) Standard Reference Materials (SRM) 997. Thus, we placed a few ng of Tl (NIST SRM 997) in the eluted Pb solution, which is sufficient for measurable intensities of Pb ion beams, for approximately 9 min (for 60 cycles).

Each measurement of both standards and samples comprised of four blocks of 15 cycles, consisting of 8.389 s integrations with 3 s idle time. The sample solutions were introduced into an argon source through a nebuliser, which converted the liquid samples into a fine mist, and then were passed through the inlet system of either the spray chamber or the Aridus desolvating system. A spray chamber was used for the samples having sufficient Pb concentrations with standard sample and skimmer cones. The samples with lower Pb concentrations were analysed using an Aridus inlet system equipped with sensitive cones (Jet sampler and X skimmer cones) to optimise the sensitivity of the measurement. This enabled the analysis of samples with low Pb concentrations at high precision. The nebuliser used here produced an uptake rate of approximately 150 µl/min.

Seven Faraday cups were mounted to simultaneously measure the ion currents of L3: ^{202}Hg, L2: ^{203}Tl, L1: ^{204}Pb, Centre: ^{205}Tl, H1: ^{206}Pb, H2: ^{207}Pb, and H3: ^{208}Pb. The ion beam of ^{202}Hg was monitored to correct for ^{204}Hg isobaric interference on ^{204}Pb, as trace amounts of Hg may be present in the sulfide minerals and/or the carrier argon of the plasma (Hirata and Nesbitt, 1995), assuming a ^{202}Hg/^{204}Hg ratio of 4.350370 (Berglund and Wieser, 2011). The constant ^{203}Tl/^{205}Tl ratio was applied to all measurements, assuming a reference value of 0.418922 (Berglund and

Wieser, 2011), employing the exponential law to correct the mass fractionation. We tried to maintain the Pb/Tl ratio at > 10 as the baseline of ^{204}Pb (mass 204.5) can be increased by the tail of the high ^{205}Tl ion beam and is affected by the denominator ^{204}Pb. Exceptions were present for a few measurements of samples with low Pb concentrations. Simultaneously, we spiked a sufficient amount of Tl in the sample solutions to enable us to collect the precise ^{205}Tl/^{203}Tl ratio for normalisation.

Prior to the analysis, the amplifier gain (only 10^{11} Ω amplifiers were used for all Faraday cups) should be calibrated daily as each Faraday cup was connected to a current amplifier. Baselines were measured on ± a half mass unit above each peak at the beginning of the analysis each day, for 200 cycles each with 1.05 and 30 s of pre-baseline wait time.

After plasma ignition, we had a warm up period of at least 60 min for stable HV. The torch position, gas flow (cool gas, sample gas, and auxiliary gas), RF power, zoom optics, and source lens systems were adjusted to optimise the ion beam intensities, stabilities, and shapes before data collection. Between measurements of samples and standards, the systems were cleaned by flushing with 0.5 M HNO_3 acid and Milli-Q water for 25 and 5 min, respectively, to eliminate the memory effects of the system from the previous measurement of the inlet system.

The mass intensities were processed by on-line correction, which subtracts the baseline, the contribution of interference of ^{204}Hg on ^{204}Pb, mass fractionation by ICP-MS using the identical ^{205}Tl/^{203}Tl ratio, and filtered outliers of 2σ standard deviation based on each block. This yielded precise and accurate data, as shown in Table 2.5. No blank corrections were made to the data as the total blanks for samples measured were reproducible below the nanogram level.

The NIST SRM 981 Pb solution as a standard was also analysed between every four samples to quantify the reproducibility of the Pb analyses. All the standards exhibited the same isotope composition within an error margin, indicating that further correction was not necessary. In addition, the uncertainties between the standard and samples were approximately the same, implying that the impurities in the samples were removed by chromatography, and thus the matrix elements were not affected in the measurement of the samples.

2.3.4. Sample preparation for S isotope analysis

Approximately 1 mg sulfides (nine pyrites and two sphalerites) were micro-drilled for S isotope analysis by re-using some of the micro-drilled holes in the Pb isotope analyses.

Pure sulfide powder (100–200 µg) were homogeneously mixed with 300–600 µg of vanadium-pentoxide (as a catalyst) in tin capsules. Isotope measurements were carried out via EA-IRMS using an EA Isolink elemental analyser interfaced to a Thermo Scientific Delta V Advantage gas source mass spectrometer. Reproducibility was generally greater than 0.3‰. Analytical performance was monitored using international reference materials (IAEA S1, S2, S3, and NBS 127) and internal laboratory standards (Ag_2S and CdS). S isotope analyses were conducted at Institut für Geologie und Paläontologie, Westfälische Wilhelms-Universität.

2.4. Results and Discussion

2.4.1. Mineralogy

Optical microscopy identified mineral assemblages, textures, and paragenetic sequence of all sulfide phases. Major sulfide minerals are sphalerite (Sp), galena (Gn), arsenopyrite (Apy), pyrite (Py), marcasite (Mrc) and pyrrhotite (Po) (Fig. 2.12), along with small amounts of chalcopyrite (Ccy), stannite (Stn), bournonite (Bn), and Tetrahedrite (Ttr). With these sulfide phases, we found gangue minerals, mostly quartz and carbonates (calcite, dolomite and rhodochrosite). Figure 2.12 shows representative photomicrographs of the samples from the North orebody. The textures of all samples are complex with various features such as different forms of vein infilling, replacement and brecciation.

Pyrite is the most common and abundant phase in all samples (Fig. 2.12). Pyrite occurred in a variety of shapes from euhedral to anhedral and reached 1 mm. We found four generations of pyrite in the twelve samples; one was a small-grained and euhedral cubic pyrite without any inclusions (1^{st} pyrite). This smaller euhedral pyrite was probably precipitated in the earliest stage of the Janggun mineralization, at about the same time as pyrrhotite. The most common pyrite is massive and contains many relict pyrrhotite inclusions (2^{nd} pyrite). Elongate pyrite (2^{nd} pyrite) with the typical tabular hexagonal habit of pyrrhotite in sphalerite grains was frequently observed, implying that the pyrite is the pseudomorph of pyrrhotite and that pyrite grew relatively late at the expense of pyrrhotite. The pyrite-forming retrogression of pyrrhotite suggests a later-stage increase in sulfur fugacity. Figures 2.12(E–L) illustrate the typical lamellar texture of the

replacement of pyrrhotite by pyrite and marcasite (3rd pyrite), typically produced at an even later stage and lower temperature than those of the previous two generations. Figures 2.12(E–H) display brown colored dots with/without the concentric growth of "bird's eye textures" (Ramdohr, 1969) (4th pyrite), resulting from typical alteration of pyrrhotite into a fine mixture of marcasite and pyrite and indicating low temperature conversion of pyrrhotite. The bird's eye texture can often be poorly recognized due to the very small grain size of the pyrite and marcasite and the ensuing difficult visual distinction between pyrite and marcasite. Since this observation is evidence of the most recent alteration, the fine-grained pyrite with marcasite were probably formed together during the latest-stage alteration at the lowest temperature.

Pyrrhotite was observed as small and sporadic grains, generally included in sphalerite, arsenopyrite, and pyrite in most samples, suggesting that pyrrhotite is one of the earliest phases and was (nearly) completely replaced by massive pyrite, marcasite and/or chalcopyrite in some of the samples. In only two of 12 samples, pyrrhotite occurs both as inclusions or relics within other sulfide grains, and as relatively large and subhedral or anhedral grains. The pyrrhotite grains in two samples are closely associated with galena (Fig. 2.12(K, L)), suggesting co-generations of both phases.

Marcasite is observed in two different generations, generally intergrown with anhedral pyrite (sometimes, intergrown with galena). The first stage of marcasite with 3rd pyrite occurs in the texture of lamellar replacement at the expense of pyrrhotite. The second stage forms the fine-aggregates with/without bird's eye texture at the last precipitation of 4th pyrite in a lower temperature environment.

Arsenopyrite generally preserves euhedral (Fig. 2.12(A–D)) to subhedral (Fig. 2.12(E–H)) shapes as prismatic crystals up to 1.5 mm in length. Arsenopyrite is observed with minor corrosion of the edges and fractures. The fractured arsenopyrite grains commonly host veins of other sulfide phases and carbonates or quartz, suggesting that arsenopyrite was among the first sulfides formed. However, arsenopyrite also has pyrrhotite inclusions, indicating it precipitated slightly later than pyrrhotite. It is likely that, at the beginning of mineralization of the Janggun mine, the original assemblage was mainly pyrrhotite + arsenopyrite (± euhedral 1st pyrite), which changed to 2nd pyrite + arsenopyrite (± euhedral 1st Pyrite) when pyrrhotite was later replaced. Unlike pyrrhotite, arsenopyrite was not replaced because it is far more refractory than pyrrhotite. We sometimes found fine-grained, elongate phases within a few arsenopyrite grains, defined by scanning electron

microscope, and Fe oxides and K-Al silicates like muscovite. The Fe-oxides are probably magnetite because of the reducing environment of the Janggun mineralization.

Chalcopyrite commonly occurs as a form of inclusions in sphalerite grains known as "chalcopyrite disease" (Barton and Bethke, 1987). Some chalcopyrite grains form interstitial phases up to 300 μm in length in minute cavities or between the sulfides and gangue minerals. In some samples, chalcopyrite shows the typical lamellar shaped texture, the same texture observed in 3rd pyrite + marcasite, indicating that chalcopyrite has also replaced pyrrhotite. Also, chalcopyrite aggregates and grains are closely associated with late-stage galena, stannite, and bournonite precipitates (Fig. 2.12(I)).

Sphalerite is commonly associated with arsenopyrite, pyrite, galena, and chalcopyrite in all samples and is often fractured. The most interesting characteristic of sphalerite is that sphalerite carries many inclusions, visually ranging from a few to 30 μm (Fig. 2.12). The inclusions were mainly chalcopyrite and pyrrhotite, and sometimes stannite (Fig. 2.12(I)). We found chalcopyrite inclusions in two textural patterns. The first one is the random distribution of chalcopyrite inclusions in sphalerite grains, which probably results from co-precipitation of both phases or replacement of sphalerite by chalcopyrite (Wiggins and Craig, 1980; Hutchinson and Scott, 1981; Barton and Bethke, 1987; Eldridge et al., 1988; Sugaki et al., 1987; Bortnikov et al., 1991). These two mechanisms are more likely than copper exsolution as the hydrothermal fluids cool down (Schneiderhohn, 1922; Ramdohr, 1924), since the temperature of the Janggun mineralization is not high enough to exsolve much copper. The second pattern of chalcopyrite distribution is a vein-filling texture through fractures and cracks within sphalerite, indicating secondary infiltration of copper-rich fluids. Intermorphic pyrrhotite inclusions and dots in sphalerite were often observed, which may indicate that sphalerite that has inclusions of pyrrhotite formed in the same period as pyrrhotite was mineralized.

Galena was observed in all samples (like sphalerite and pyrite) in variable amounts. Galena occurs from euhedral to irregular shapes and various sizes in different samples up to 1 mm (Fig. 2.12). In particular, galena in the two pyrrhotite-bearing samples is closely associated (and sometimes intergrown) with pyrrhotite (Fig. 2.12(K–L)). Galena is generally present with chalcopyrite and occasionally with bournonite in the other samples. The lamellar replacement texture, frequently observed with 3rd pyrite + marcasite as well as sometimes in chalcopyrite, is also observed in galena.

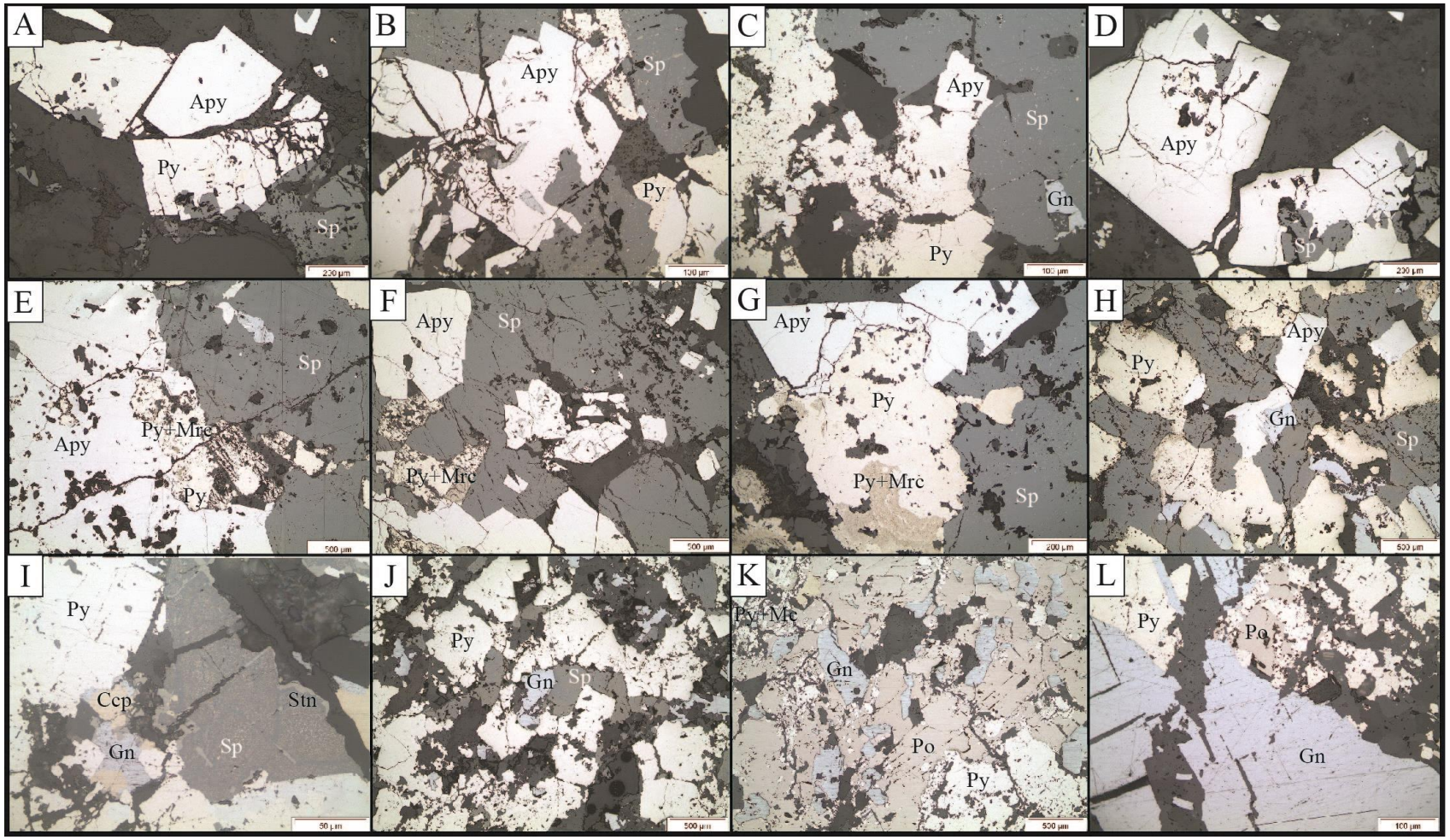

Figure 2.12. Representative reflected-light photomicrographs, illustrating mineral phases and textures in the Pb-Zn ores from the Janggun mine. Each photomicrograph represents one sample from the North orebody (A = N439; B = N441; C = N443; D = N478; E = N408; F = N416; G = N451; H = N454; I = N435; J = N472; K = N420; L = N433). (A) to (D) illustrate euhedral arsenopyrite and euhedral to subhedral pyrite. Arsenopyrite and pyrite are closely associated and have many fractures which allowed the in filtration of other sulfides and gangue minerals. (E) to (H) show euhedral to subhedral arsenopyrite, different generations of pyrite wi th marcasite. Pyrite and marcasite occurs like brown aggregates with well to poorly developed “birds eye” texture. Arsenopyrite is more

strongly deformed and brecciated. Sphalerite is widespread in the samples and galena occurs with irregular shapes associated with sphalerite. (I) and (J) display euhedral to subhedral pyrite with sphalerite and galena. Especially the photomicrograph (I) shows the sphalerite with the evidence of exsolution as well as introduction of stannite along the cracks and edges of sphalerite. Chalcopyrite occurs closely associated with galena. (K) and (L) show pyrrhotite grains which were not observed in other samples and mineral assemblages (Table 2). Pyrrhotite is closely related with galena, pyrrhotite and galena have irregular shapes and pyrrhotite is abundantly replaced by pyrite, marcasite, or chalcopyrite. (Abbreviations: Py = pyrite; Apy = arsenopyrite; Sp = sphalerite; Gn = galena; Mrc = marcasite; Po = pyrrhotite; Ccp = chalcopyrite; Stn = stannite)

The 12 samples from the North orebody can be subdivided into four groups depending on the occurrence of specific minerals as well as similar textural characteristics described in Table 2.3. The first and second groups contain arsenopyrite as a major sulfide mineral, whereas the third and fourth assemblage groups barely contain arsenopyrite, if at all. A further distinction was made based on the presence of last stage of 4th pyrite + marcasite which resulted from the lowest temperature alteration; only groups 2 and 4 contain pyrite + marcasite showing alteration as brown dots with bird's eye textures. In summary, the groups contain the following assemblages (Table 2.3): (1) arsenopyrite, pyrite, sphalerite, galena; (2) arsenopyrite, pyrite, sphalerite, galena, marcasite; (3) pyrite, sphalerite, galena; (4) pyrite, sphalerite, galena, pyrrhotite, marcasite. The group 4 only contains pyrrhotite. A small amount of chalcopyrite, bournonite and stannite has been observed in all samples as inclusions in sphalerite and/or related to galena. In the North orebody, the mineral assemblages that include arsenopyrite are more common than those without it.

Table 2.3. Mineral assemblages of the sample based on the mineral observation collected from the North orebody in the Janggun mine.

	Mineral assemblage	Sample number			
1	Arsenopyrite + Pyrite + Sphalerite + Galena	N439	N441	N443	N478
2	Arsenopyrite + Pyrite + Sphalerite + Galena + Marcasite	N408	N416	N451	N454
3	Pyrite + Sphalerite + Galena	N435	N472		
4	Pyrite + Sphalerite + Galena + Pyrrhotite + Marcasite	N420	N433		

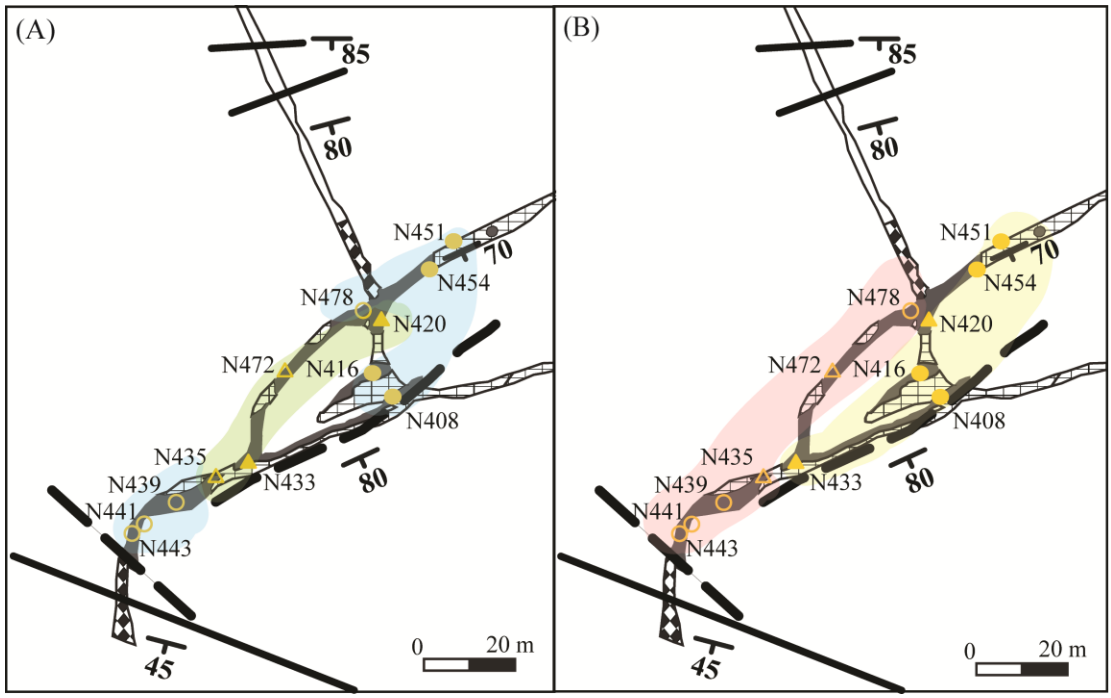

Figure 2.13. Underground map (modified from Lee et al., 1990) of the sampling locations; (A) preservation of early-stage arsenopyrite: present (blue) or absent (green); (B) distribution of last-stage alteration: pyrite-marcasite present (yellow) or absent (pink).

The spatial relation based on the criteria that divide the mineral assemblage groups above is shown in Figure 2.13, illustrating that arsenopyrite is not observed in the middle part whereas samples from both edges contain arsenopyrite (Fig. 2.13(A)). The second criterion, occurrence of 4th pyrite + marcasite, (Fig. 2.13(B)) divides the sampling region into southeast and northwest. The textural features and mineral assemblage of the one studied sample from the South orebody is similar to group 4 of the North orebody, whereby pyrrhotite occurs more frequently with presence of stannite, bournonite and sometimes tetrahedrite.

The complex structural and textural relationships between different generations of sulfides appear to contradict a simple genesis, whereby each phase would have a single place in the paragenetic sequence. The intergrowth relations instead suggest a multi-stage ore-forming process, since the formation temperature for the Janggun deposit ranges from 200 to 350°C (Imai and Lee 1980; Lee et al. 1990). We propose pyrrhotite was precipitated in the earliest stage, along with the first stage of small-grained euhedral pyrite and small amount of galena (Fig. 2.14). Sphalerite and arsenopyrite are closely intergrown and started forming later than pyrrhotite but overlapped at the

end of pyrrhotite formation. Sphalerite and arsenopyrite growth were prolonged after pyrrhotite stopped growing. Sphalerite often occurs as tabular hexagonal intergrowth with pyrite pseudomorphs after pyrrhotite, indicating sphalerite was formed earlier than the massive 2nd pyrite; the 2nd pyrite also contains abundant pyrrhotite inclusions, suggesting the pyrite replaced the pyrrhotite. We also observed pyrite, marcasite, chalcopyrite, and galena with the typical lamellar replacement texture of pyrrhotite. These different characteristics of pyrite occurrences suggest that the pyrite grew in three distinct stages during the main ore mineralization (Fig. 2.14). Generally, massive 2nd stage pyrite replaced most of pyrrhotite in the samples from the Janggun mine. Galena was also clearly formed in two stages, one associated with pyrrhotite replacement, and the predominant one associated with chalcopyrite, bournonite, and stannite. Chalcopyrite, bournonite and stannite were the last phases of the main formation period of the Janggun mine.

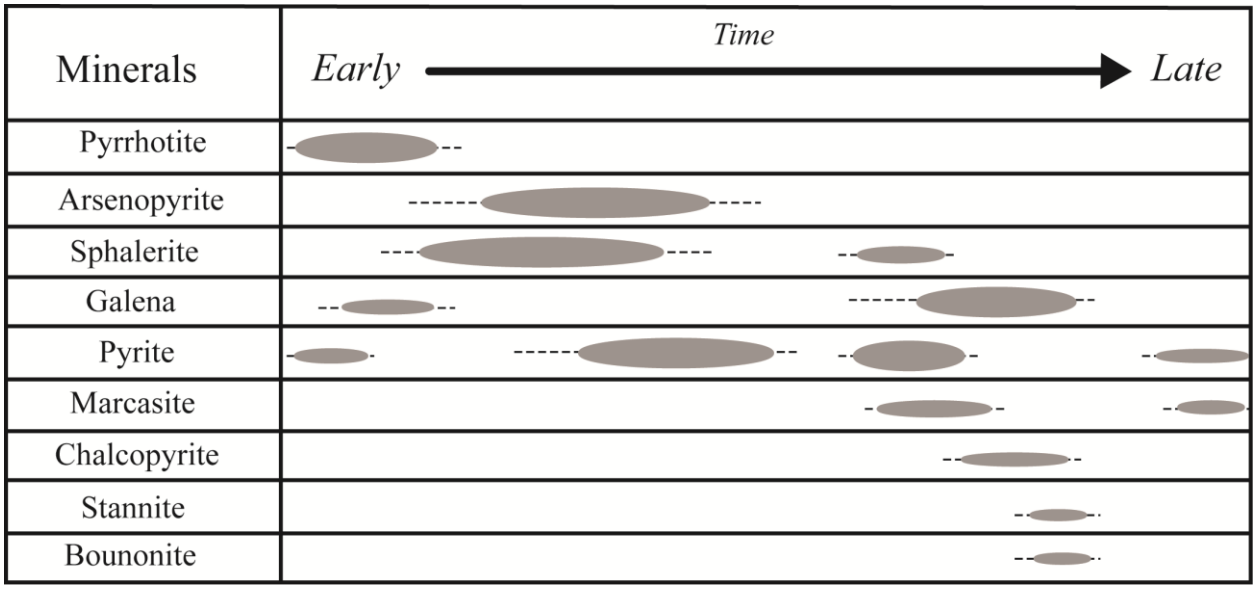

Figure 2.14. Paragenetic sequence of all sulphide phases investigated in the study from the main adit level (591m) of the North orebody in the Janggun deposit, showing successive mineral generations.

Lastly, after the main period of the Janggun mineralization, low-temperature alteration led to the growth of 4th pyrite + marcasite in fine aggregates with/without the concentric growth of bird's eye texture, especially in the samples from the NE as shown in Figure 2.13(B). Since the paragenetic sequence does not agree with the general sulfide formation sequence based on the

temperature, it may reflect that the separate fluid events might be involved in the Janggun mineralization.

2.4.2. Mineral chemistry

The principal sulfides in the Janggun mine pyrite, sphalerite, galena, arsenopyrite, chalcopyrite, and pyrrhotite were measured by EPMA to define chemical compositions, since there may be correlations between EPMA and Pb isotope analysis. Particularly, EPMA focused on the six samples (five from the north orebody and one from the south orebody), in which different phases were collected for Pb isotopic compositions. Twelve elements (S, Cu, Fe, Zn, Mn, As, Pb, Cd, Ag, Ni, Co, and Sb) were chosen to investigate compositional variations. Not all of these elements were above detection limit in a given mineral. Results are given in Table 2.4.

The totals of the element concentrations measured by EPMA range from 97.6 to 104.1 wt.%. These anomalous results are mineral-specific: sphalerite has an overall average total of 103.1 wt.%, and galena has an average total of 99.3 wt.%, whereas all others average around 100 wt%. Even if the sphalerite concentrations are offset by a small calibration bias, the relative concentration variations of each element within the same phase can be reliably quantified.

2.4.2.1. Sphalerite

Sphalerite accommodates Fe, Zn, Mn, and also Cd and Cu as trace elements. No direct relationship between the compositional variations and mineral assemblages (1) - (4) was observed. In particular, Cu concentration in sphalerite analyzed in this study shows a variation by over two orders of magnitude, from 0.03 to 8.8 wt.% (Table 2.4).

Sphalerite shows a negative correlation between Cu and Fe (Fig. 2.15). A reference line with a slope of -1, showing in Figure 2.15(A) represents a substitution of Fe^{2+} by Cu^{2+}, i.e. the presence of Cu-rich inclusions which could explain the data points with Cu $\geq$ 4 wt.%. This correlation breaks down for Cu < 0.6 wt.%, requiring a different mineral inclusion. Figure 2.15(C) also shows a marked difference between the five points with Cu $\geq$ 4 wt.% and all others; the latter form an alignment with a negative slope around -0.5.

By means of a Zn/Fe vs. Cu/Fe common denominator diagram, we explored the possibility that the high Cu concentrations are due to chalcopyrite is addressed in Figure 2.15(B). We

observed numerous small inclusions in sphalerite under the reflecting microscope and thus sub-µm inclusions could have escaped visual detection and been detected by electron probe, even though we tried to avoid them for selection of spots for EPMA.

The three most Cu-rich sphalerite data points lie on the segment connecting the stoichiometric compositions of sphalerite and chalcopyrite, following the trend described by Keith et al. (2014) for "chalcopyrite disease", i.e. the patchy substitution of sphalerite by secondary chalcopyrite, following the reaction $ZnS+FeS+Cu^{2+} \rightarrow CuFeS_2+Zn^{2+}$. The other points deviate from the chalcopyrite disease trend, and show a positive correlation between Zn/Fe and Cu/Fe (Fig. 2.15(B)). The diagram also shows the stoichiometry of additional Cu-bearing phases from the South-A orebody (stannite and tetrahedrite). It demonstrates that the high Cu concentration is not explained by minute inclusions of stannite and tetrahedrite (Fig. 2.15(B)), which lie completely off-trend. The most likely explanation is based on the observations summarized in Figure 2.14: there are at least two different generations of sphalerite. One is Fe-poor and affected by "chalcopyrite disease", another (that with a larger number of data points in Figs. 2.15(A, B)) is Fe-rich and nearly Cu-free. Grains that consist of a patchy mosaic of both generations display the Fe-Cu anticorrelation shown in Figure 2.15(A).

The substitution of Cu for Fe in the sphalerite structure is unlikely. If Cu were present as Cu^+, it could be incorporated into sphalerite via the coupled substitution $2Zn^{2+} \leftrightarrow Cu^+ + In^{3+}$ or Sb^{3+} (Johan, 1988; Cook et al., 2009), which probably also applies to the Fe-Cu substitution that we observe. However, no positive correlation of Cu with Sb and no high Sb concentrations were measured. Similarly, there is circumstantial evidence that indium substitution was not a major factor, even if we did not measure the In concentration directly. Since the sum ([In]+[Sb]) should be equal to the increase in [Cu], the total of the measured elements shown in Table 2.4 would be incomplete and should fall short of 100 % if a significant amount of In had been missed. Moreover, the "incomplete" total should negatively correlate with [Zn]. On the contrary, the sphalerite total always exceeds 100 % and does not correlate with [Zn] (Table 2.4).

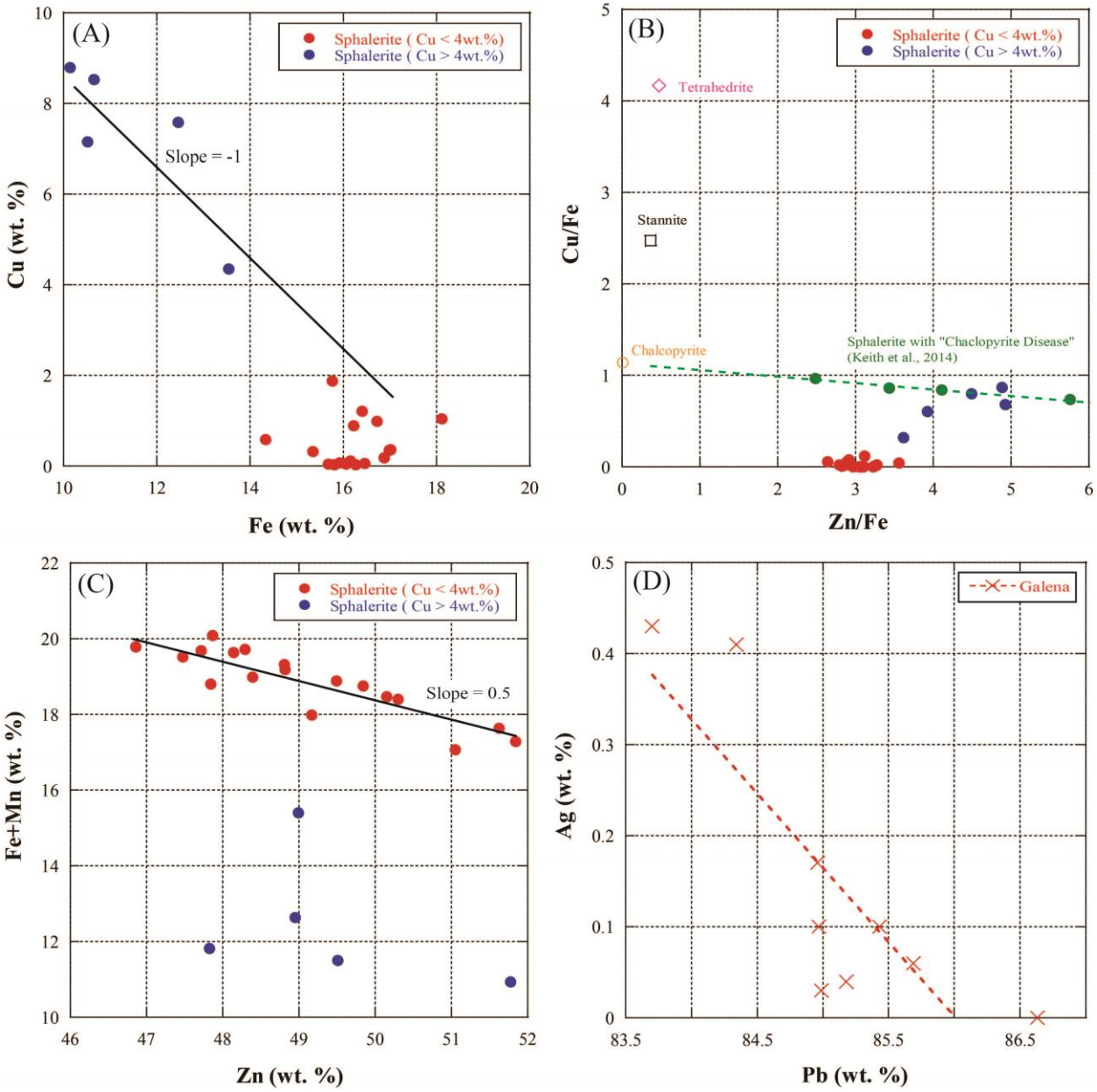

Figure 2.15. Element concentrations and ratios in sphalerite (A)–(C) and galena (D). (A) Fe vs. Cu concentrations. In the high Cu sphalerite, Fe and Cu are negatively correlated, indicating a nearly stoichiometric substitution (black line); in the low Cu sphalerite the Fe variations are not matched by Cu. (B) Zn/Fe vs. Cu/Fe ratios. The stoichiometry of chalcopyrite, stannite and tetrahedrite is also shown; two generations of sphalerite are recognized (see also Fig. 2.14): a Fe-poor one affected by "chalcopyrite disease", and a Fe-rich, nearly Cu-free one. (C) Zn vs. Fe+Mn concentrations. A negative correlation in the Low-Cu sphalerite indicates the substitution (Fe^{2+}, Mn^{2+}) ↔ Zn^{2+}; (D) Ag vs. Pb in galena show a very scattered negative trend, whose slope is inconsistent with a substitution reaction Ag_2S of PbS (Unit = wt. %).

Fe and Mn are major elements in sphalerite, and (Fe+Mn) is negatively correlated with Zn (Fig. 2.15C), as expected for the substitution (Fe^{2+}, Mn^{2+}) ↔ Zn^{2+}. This substitution is favoured by the similar size and identical charge of these three elements. Cd concentrations in sphalerite are relatively constant across the samples, ranging from 0.19 to 0.27 wt.% with no difference based on the Cu concentrations of sphalerites (Table 2.4). A weak negative correlation between Cd and Mn might suggest the possibility of substitution of Zn^{2+} by either Mn^{2+} or Cd^{2+}.

Figure 2.16 shows the histograms of five elements (Fe, Mn, Zn, Pb, and Sb) in sphalerite, pyrite, and galena. The concentrations of these elements in sphalerite are not unimodal, confirming that there are at least two or three compositionally distinct generations of sphalerite, as the range of concentrations is much larger than the analytical uncertainty on the individual measurement by EPMA.

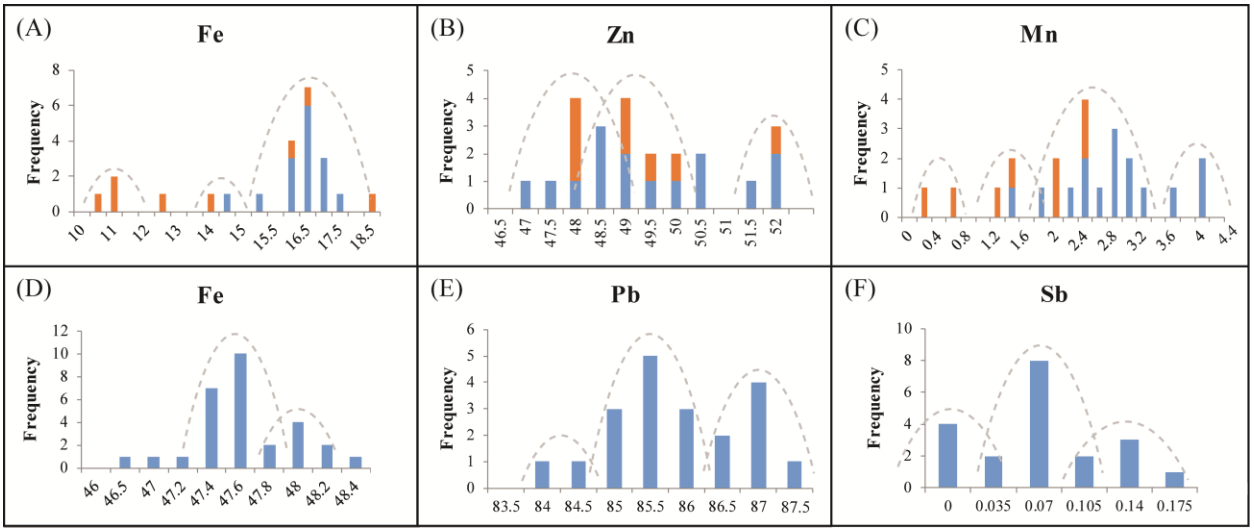

Figure 2.16. Histograms of element concentrations. (A)–(C) Sphalerite; (D) Pyrite; (E) –(F) Galena. The distribution of concentrations is multi-modal. Dashed lines illustrate possible modes (Unit = wt. %).

2.4.2.2. Pyrite

Pyrite shows very limited variation of the Fe:S ratio (Table 2.4). The minor and trace elements (Zn, Ni, Cu, As, Ag, and Sb) were not detected in all grains. Especially Co and Ni, which commonly substitute for Fe, are around detection limit in pyrite from the study area; therefore, the inter-element relationships are not significantly resolved. Only Fe concentrations of pyrite were

plotted in a histogram (Fig. 2.16(D)). As the histogram suggests bimodality, it confirms the observation shown in Figure 2.14 that there are several generations of pyrite.

2.4.2.3. Galena

The result of galena (Table 2.4 and Fig. 2.15(D)) shows that Cd, Sb Zn, Fe, Ni, Co, and Cu were detectable in some grains. Ag concentrations, which were above detection limit in two samples (N433 and N435), show a very scattered negative correlation with Pb concentrations (Fig. 2.15(D)), indicating that its slope is not consistent with a substitution reaction of PbS by Ag_2S in the structure of galena crystal. The average grade of Ag in the Janggun mine is 100 g/ton (Imai and Lee, 1980), but Ag is mostly hosted in the South orebody and deficient in the North orebody which is consistent with the low content of Ag observed in the galena here. In addition, S and Sb show a weak anticorrelation indicative of substitution for S by Sb (Table 2.4). No other significant correlation trend was observed. Like sphalerite and pyrite, Pb and Sb concentration of galena are plotted in histograms (Fig. 2.16(E, F)). The columns of Pb and Sb contents confirm the petrographic observation of different generations of galena (Fig. 2.14), as previously stated for sphalerite and pyrite. For arsenopyrite, chalcopyrite, pyrrhotite, only few analyses were acquired and are presented in Table 2.4 for completeness's sake.

Table 2.4. Electron microprobe analyses of sphalerite, pyrite, galena, arsenopyrite, chalcopyrite, and pyrrhotite (unit: wt.%)

1. Sphalerite

Sample No.	S	Fe	Zn	Cd	Mn	Cu	As	Pb	Ag	Ni	Co	Sb	Total
N416	34.03	16.26	49.49	0.23	2.62	0.03	0.02	b.d.	b.d.	b.d.	b.d.	b.d.	102.68
	34.16	15.81	48.29	0.22	3.91	0.03	b.d	b.d.	b.d.	b.d.	0.01	b.d.	102.43
	33.90	15.68	48.14	0.19	3.96	0.04	b.d.	b.d.	b.d.	b.d.	b.d.	b.d.	101.91
	33.99	16.46	48.81	0.22	2.85	0.05	0.03	b.d.	b.d.	0.02	b.d.	b.d.	102.43
	33.84	16.07	49.84	0.21	2.69	0.05	0.08	b.d.	b.d.	b.d.	b.d.	b.d.	102.78
	33.51	16.16	50.15	0.23	2.31	0.12	b.d.	b.d.	b.d.	0.02	b.d.	b.d.	102.49
	34.50	15.35	50.30	0.20	3.05	0.31	b.d.	b.d.	b.d.	b.d.	b.d.	b.d.	103.72
	34.75	14.33	51.05	0.24	2.74	0.58	0.02	b.d.	b.d.	b.d.	b.d.	b.d.	103.72
	34.38	16.41	47.84	0.21	2.39	1.21	b.d.	b.d.	b.d.	b.d.	b.d.	b.d.	102.44
N433	33.97	16.06	51.84	0.27	1.23	0.05	b.d.	b.d.	b.d.	b.d.	b.d.	b.d.	103.42
	34.21	15.77	49.17	0.22	2.21	1.87	0.01	b.d.	b.d.	b.d.	b.d.	b.d.	103.46
	34.16	13.55	48.99	0.23	1.85	4.35	b.d.	b.d.	b.d.	0.01	b.d.	b.d.	103.14
	33.97	10.52	51.78	0.24	0.42	7.16	b.d.	b.d.	b.d.	b.d.	0.01	b.d.	104.09
	34.14	12.46	48.95	0.20	0.18	7.58	b.d.	b.d.	0.01	b.d.	b.d.	0.01	103.53
N435	34.61	10.65	47.83	0.19	1.17	8.53	b.d.	b.d.	0.02	b.d.	b.d.	b.d.	103.00
	34.95	16.99	47.48	0.23	2.52	0.35	b.d.	b.d.	b.d.	b.d.	b.d.	b.d.	102.52
	35.26	16.88	47.72	0.22	2.81	0.19	b.d.	b.d.	b.d.	0.02	b.d.	b.d.	103.10
	35.36	16.22	46.86	0.24	3.56	0.90	b.d.	b.d.	b.d.	0.03	b.d.	b.d.	103.17
N441	33.57	10.14	49.51	0.21	1.36	8.79	0.03	b.d.	0.01	b.d.	b.d.	b.d.	103.63
	33.98	16.72	48.39	0.25	2.27	0.99	0.02	b.d.	b.d.	b.d.	b.d.	b.d.	102.62
	34.04	17.01	48.82	0.23	2.17	0.37	0.05	b.d.	b.d.	b.d.	b.d.	b.d.	102.68
N478	34.75	18.11	47.87	0.21	1.98	1.05	0.02	b.d.	b.d.	b.d.	b.d.	b.d.	103.99
	34.52	15.92	51.63	0.23	1.72	0.06	b.d.	b.d.	b.d.	b.d.	b.d.	b.d.	104.09

2. Pyrite *(Continuous)*

Sample No.	S	Fe	Zn	Cd	Mn	Cu	As	Pb	Ag	Ni	Co	Sb	Total
N416	53.39	47.85	0.09	b.d.	b.d.	b.d.	b.d.	b.d.	0.01	0.01	b.d.	b.d.	101.34
	53.55	48.03	0.00	b.d.	b.d.	0.01	b.d.	b.d.	0.01	0.01	b.d.	b.d.	101.61
	52.78	46.11	0.02	b.d.	b.d.	b.d.	0.02	b.d.	b.d.	b.d.	b.d.	b.d.	98.93
	51.87	46.76	b.d.	b.d.	b.d.	b.d.	0.08	b.d.	0.01	b.d.	b.d.	b.d.	98.71
N433	53.26	47.68	0.01	b.d.	b.d.	b.d.	b.d.	b.d.	0.01	0.01	b.d.	0.01	100.97
	53.02	47.29	b.d.	b.d.	b.d.	b.d.	0.01	b.d.	0.01	0.01	b.d.	b.d.	100.35
	53.22	47.49	b.d.	b.d.	b.d.	0.02	b.d.	b.d.	0.01	0.01	b.d.	b.d.	100.74
	52.93	47.25	0.01	b.d.	b.d.	b.d.	b.d.	b.d.	b.d.	b.d.	b.d.	b.d.	100.19
N435	53.42	47.95	0.04	b.d.	b.d.	b.d.	b.d.	b.d.	b.d.	b.d.	b.d.	b.d.	101.41
	54.30	47.85	b.d.	b.d.	b.d.	b.d.	0.01	b.d.	b.d.	b.d.	b.d.	b.d.	102.16
	53.97	48.34	0.05	b.d.	b.d.	b.d.	0.01	b.d.	0.01	0.01	b.d.	b.d.	102.38
	54.49	47.93	b.d.	b.d.	b.d.	0.05	0.01	b.d.	b.d.	0.01	b.d.	b.d.	102.49
	54.55	48.08	b.d.	b.d.	b.d.	0.01	0.01	b.d.	0.01	b.d.	b.d.	b.d.	102.65
	54.60	47.59	0.03	b.d.	b.d.	b.d.	b.d.	b.d.	0.01	b.d.	b.d.	b.d.	102.23
	54.39	47.39	b.d.	b.d.	b.d.	0.01	0.02	b.d.	b.d.	0.01	b.d.	b.d.	101.82
	53.64	47.35	b.d.	b.d.	b.d.	b.d.	0.01	b.d.	b.d.	0.02	b.d.	b.d.	101.01
	54.13	47.58	b.d.	b.d.	b.d.	0.02	0.02	b.d.	b.d.	b.d.	b.d.	b.d.	101.76
	54.49	47.49	b.d.	b.d.	b.d.	b.d.	0.04	b.d.	b.d.	b.d.	b.d.	0.01	102.03
	54.57	47.01	b.d.	b.d.	b.d.	0.03	b.d.	b.d.	0.04	0.01	b.d.	b.d.	101.65
N441	52.81	47.57	0.09	b.d.	b.d.	0.03	0.03	b.d.	b.d.	b.d.	b.d.	0.17	100.70
	52.96	47.42	b.d.	b.d.	b.d.	0.02	0.01	b.d.	b.d.	b.d.	b.d.	b.d.	100.41
	52.26	47.43	0.01	b.d.	b.d.	b.d.	0.04	b.d.	b.d.	b.d.	b.d.	b.d.	99.74
N478	53.13	47.38	0.01	b.d.	b.d.	0.02	b.d.	b.d.	b.d.	b.d.	b.d.	0.01	100.55
	52.57	47.42	b.d.	0.01	b.d.	b.d.	0.01	b.d.	b.d.	b.d.	b.d.	b.d.	100.01
	53.76	47.65	0.01	b.d.	b.d.	b.d.	0.01	b.d.	0.01	b.d.	b.d.	0.02	101.45
	52.81	47.45	b.d.	b.d.	b.d.	0.02	b.d.	b.d.	b.d.	b.d.	b.d.	b.d.	100.28
	53.06	47.33	0.01	b.d.	b.d.	0.04	b.d.	b.d.	0.02	0.02	b.d.	b.d.	100.48
	53.26	47.52	0.00	b.d.	b.d.	b.d.	b.d.	b.d.	0.01	b.d.	b.d.	b.d.	100.79
	52.93	47.21	0.02	b.d.	b.d.	b.d.	b.d.	b.d.	0.01	b.d.	b.d.	0.09	100.26

3. Galena *(Continuous)*

Sample No.	S	Fe	Zn	Cd	Mn	Cu	As	Pb	Ag	Ni	Co	Sb	Total
N416	13.46	b.d.	0.06	0.13	b.d.	0.08	b.d.	86.57	b.d.	0.01	0.01	0.10	100.41
	13.13	b.d.	b.d.	0.13	0.01	b.d.	b.d.	86.93	b.d.	b.d.	0.01	0.06	100.27
	13.05	b.d.	0.05	0.11	b.d.	0.01	b.d.	85.31	b.d.	b.d.	b.d.	0.06	98.60
	13.06	0.01	b.d.	0.16	b.d.	b.d.	b.d.	85.61	b.d.	0.03	0.02	0.04	98.92
	12.80	b.d.	b.d.	0.18	b.d.	b.d.	b.d.	85.43	b.d.	b.d.	b.d.	0.11	98.52
	12.93	b.d.	0.06	0.11	b.d.	0.05	b.d.	85.67	b.d.	b.d.	b.d.	0.16	98.99
	13.32	0.03	0.08	0.12	b.d.	0.02	b.d.	85.50	b.d.	b.d.	b.d.	0.13	99.21
N433	13.26	0.01	b.d.	0.14	b.d.	0.05	b.d.	83.70	0.43	b.d.	0.02	b.d.	97.61
	13.63	0.01	0.04	0.16	b.d.	b.d.	b.d.	84.34	0.41	b.d.	b.d.	b.d.	98.59
	13.33	0.06	b.d.	0.17	b.d.	b.d.	b.d.	85.43	0.10	b.d.	b.d.	b.d.	99.09
	13.34	0.03	0.02	0.14	b.d.	b.d.	b.d.	84.96	0.17	0.03	b.d.	0.03	98.71
	13.33	b.d.	b.d.	0.13	b.d.	b.d.	b.d.	86.63	b.d.	b.d.	b.d.	0.06	100.15
N435	13.56	0.02	0.06	0.13	b.d.	0.04	b.d.	84.99	0.03	0.01	b.d.	0.05	98.88
	13.53	b.d.	0.02	0.16	b.d.	0.01	b.d.	84.97	0.10	0.01	b.d.	0.08	98.87
	13.49	b.d.	0.04	0.18	0.01	0.01	b.d.	85.69	0.06	b.d.	0.01	0.07	99.56
	13.66	0.02	0.02	0.17	b.d.	b.d.	b.d.	85.18	0.04	0.01	0.01	0.05	99.15
N441	13.05	0.02	0.04	0.16	b.d.	0.03	b.d.	87.01	b.d.	0.01	0.01	0.04	100.36
	13.14	0.01	b.d.	0.13	b.d.	b.d.	b.d.	86.15	b.d.	b.d.	b.d.	b.d.	99.43
N478	13.39	0.00	0.02	0.14	b.d.	b.d.	b.d.	86.65	b.d.	b.d.	b.d.	0.13	100.32
	13.39	0.04	0.04	0.15	0.01	0.14	b.d.	86.38	b.d.	b.d.	0.01	0.01	100.17

4. Arsenopyrite, chalcopyrite, and pyrrhotite in order *(Continuous)*

Sample No.	S	Fe	Zn	Cd	Mn	Cu	As	Pb	Ag	Ni	Co	Sb	Total
N416	20.61	35.64	b.d.	b.d.	0.01	b.d.	45.70	b.d.	b.d.	b.d.	b.d.	0.06	102.01
	21.34	36.10	b.d.	b.d.	0.01	0.01	45.03	b.d.	b.d.	0.01	b.d.	0.02	102.52
	21.02	34.31	0.07	b.d.	b.d.	b.d.	45.39	b.d.	b.d.	b.d.	0.03	0.01	100.83
	21.34	34.51	0.02	b.d.	b.d.	b.d.	44.71	b.d.	0.02	b.d.	b.d.	0.06	100.65
	21.05	34.87	0.05	b.d.	0.01	b.d.	45.17	b.d.	0.02	0.01	0.06	0.04	101.28
	20.93	34.51	b.d.	b.d.	b.d.	b.d.	45.31	b.d.	b.d.	0.03	b.d.	0.05	100.83
	21.05	34.94	0.02	b.d.	b.d.	0.02	45.19	b.d.	b.d.	b.d.	b.d.	0.04	101.26
	20.57	34.47	0.01	b.d.	0.01	b.d.	45.60	b.d.	b.d.	b.d.	b.d.	b.d.	100.66
N441	20.79	35.60	b.d.	b.d.	b.d.	0.01	45.18	b.d.	b.d.	0.07	b.d.	0.10	101.75
	20.36	35.71	b.d.	0.02	b.d.	0.03	45.74	b.d.	b.d.	b.d.	b.d.	0.06	101.92
	20.87	35.76	b.d.	b.d.	b.d.	b.d.	45.00	b.d.	b.d.	0.02	b.d.	0.02	101.67
	20.44	35.54	0.02	b.d.	b.d.	b.d.	45.87	b.d.	b.d.	b.d.	b.d.	0.06	101.93
N478	21.16	36.38	b.d.	b.d.	0.01	0.03	44.76	b.d.	b.d.	0.01	b.d.	0.02	102.38

Sample No.	S	Fe	Cu	Zn	Mn	As	Pb	Ni	Co	Ag	Cd	Sb	Total
N433	35.15	30.96	34.79	0.19	0.01	0.01	b.d.	b.d.	b.d.	b.d.	b.d.	b.d.	101.12
	35.05	30.72	35.12	0.02	b.d.	b.d.	b.d.	b.d.	b.d.	b.d.	b.d.	b.d.	100.91
	35.13	30.02	33.90	1.66	b.d.	0.02	b.d.	b.d.	b.d.	b.d.	0.01	b.d.	100.73
	35.17	30.54	34.91	b.d.	b.d.	b.d.	b.d.	b.d.	b.d.	b.d.	b.d.	b.d.	100.62
N435	35.73	30.66	34.95	b.d.	0.02	b.d.	b.d.	b.d.	b.d.	0.01	b.d.	b.d.	101.37
	35.75	28.94	33.46	0.04	0.06	0.01	b.d.	b.d.	b.d.	0.01	0.01	b.d.	98.27
	36.02	31.55	34.71	b.d.	0.08	b.d.	b.d.	b.d.	b.d.	b.d.	b.d.	b.d.	102.36
	35.81	30.01	34.78	0.62	b.d.	0.02	b.d.	b.d.	b.d.	0.02	0.01	b.d.	101.27
	35.43	29.87	34.63	0.19	0.01	b.d.	b.d.	b.d.	b.d.	0.27	b.d.	b.d.	100.40
N441	34.46	30.57	35.08	0.13	b.d.	0.03	b.d.	b.d.	b.d.	0.02	b.d.	b.d.	100.29
	34.37	30.53	34.84	0.56	0.01	b.d.	b.d.	b.d.	b.d.	0.01	b.d.	b.d.	100.31
N478	35.08	30.45	34.65	0.62	0.01	b.d.	b.d.	b.d.	b.d.	0.02	b.d.	b.d.	100.83
	35.13	30.20	35.03	0.17	b.d.	b.d.	b.d.	b.d.	b.d.	0.01	b.d.	b.d.	100.54

Sample No.	S	Fe	Zn	Cd	Mn	Cu	As	Pb	Ag	Ni	Co	Sb	Total
N433	39.28	61.14	0.02	b.d.	b.d.	0.02	b.d.	b.d.	0.01	0.01	b.d.	b.d.	100.49
	39.50	60.86	0.03	b.d.	b.d.	b.d.	b.d.	b.d.	b.d.	b.d.	b.d.	b.d.	100.39
	39.83	61.32	b.d.	b.d.	b.d.	b.d.	b.d.	b.d.	0.02	b.d.	b.d.	b.d.	101.17
N435 (inclusions)	39.72	62.18	0.01	b.d.	b.d.	0.01	0.02	b.d.	b.d.	0.01	b.d.	b.d.	101.96
	39.52	61.77	b.d.	b.d.	0.01	b.d.	0.04	b.d.	b.d.	b.d.	b.d.	b.d.	101.34

2.4.3. Pb isotopic compositions

A total of 109 Pb isotopic compositions measurements on sulfide minerals and whole rocks were performed by MC-ICP-MS (68 from the 12 samples in the North orebody, 13 from the one sample in the South A orebody, and 28 samples of country rocks). Galena (39 grains) was micro-drilled in two to three microstructurally well-characterized locations from all samples. Also, pyrite (17) and sphalerite (15) from six samples were measured as well as arsenopyrite (6) from four samples and pyrrhotite (4) from two samples, in order to define the possible heterogeneities between different sulfide phases in the same sample.

Results are given in Table 2.5 and Figures 2.17–2.19. The absolute uncertainties for individual Pb isotope analyses are given at the 95% confidence level. The Pb isotope data of sphalerite and pyrite have higher uncertainties because those phases contain less Pb than other sulfides. Increasing the sample size to reduce the analytical uncertainty would cause an increase of the systematic uncertainty, because the very small scale of intergrowths would cause admixture of different generations of the same mineral and/or of different minerals.

2.4.3.1. Pb isotopic compositions of samples from the North orebody

The results (Figs. 2.17–2.19) are plotted in common-denominator isotope diagrams, whose axes are two of the three independent Pb isotope ratios with a common denominator ($^{206}Pb/^{204}Pb$, $^{207}Pb/^{204}Pb$, and $^{208}Pb/^{204}Pb$). The figures displays the Pb results of all sulfides separated by mineral phases (Fig. 2.17), sample locations (Fig. 2.18), and assemblages (Fig. 2.19). The Pb isotopic compositions of the North orebody do not show a single, well-defined composition, and are fairly scattered. $^{206}Pb/^{204}Pb$ ranges from 18.334 to 18.879, $^{207}Pb/^{204}Pb$ = 15.667 to 15.692, and $^{208}Pb/^{204}Pb$ = 38.682 to 38.899 (Table 2.5), well over 100 times the analytical uncertainty. The Pb isotopic compositions do not correlate with sample identity, as the different minerals in most individual rock samples span a much broader field than the distance between medians of the different samples. The heterogeneities are observed both between the different samples (at the 10-20 m scale) and within individual polished sections (at the 2 cm scale).

Generally, sphalerite, pyrite, and pyrrhotite have more heterogeneous Pb isotopic compositions whereas those of arsenopyrite and galena are more clustered (Fig. 2.17). For pyrite, the $^{206}Pb/^{204}Pb$ ratios range from 18.386 to 18.661, while $^{207}Pb/^{204}Pb$ is nearly constant, ranging

from 15.668 to 15.676. The $^{206}Pb/^{204}Pb$ ratios of sphalerite range between 18.416 and 18.879, having the widest isotopic heterogeneity of all Janggun sulfides. Pyrrhotite was only measured in rock N433; the two analyzed samples of one polished section have unradiogenic compositions ($^{206}Pb/^{204}Pb$ between 18.334 and 18.417). For arsenopyrite, only four samples from three rocks (N416, N441, N478) were analyzed; their $^{206}Pb/^{204}Pb$ ranges between 18.421 and 18.462. The case of galena is remarkable, in that its Pb isotopic composition is more clustered than that of any other mineral (36 analyses all between 18.385 and 18.433). However, it must not be overlooked that this spread is about 50 times larger than the individual measurement uncertainties, which means that also galena is strongly heterogeneous.

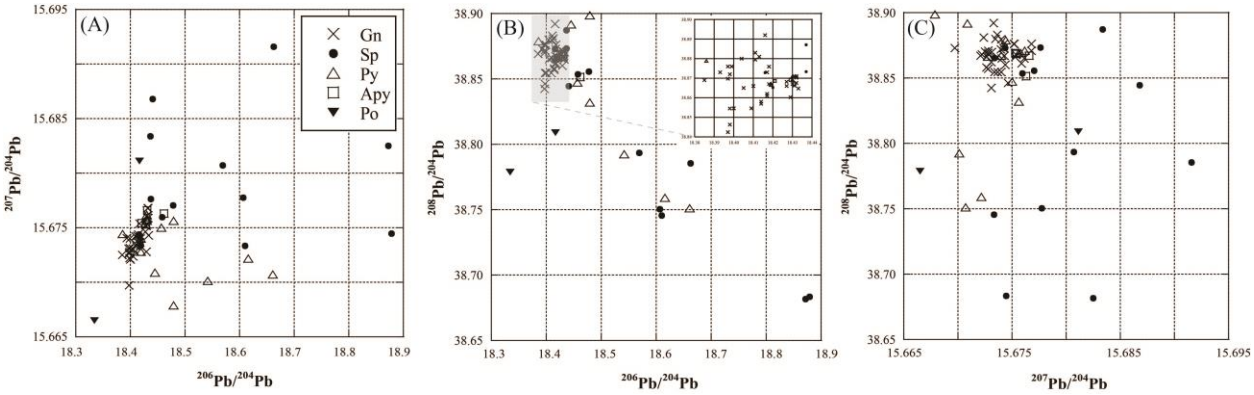

Figure 2.17. Pb isotope correlation diagrams for the samples of the North orebody. (A): $^{207}Pb/^{204}Pb$ vs. $^{206}Pb/^{204}Pb$; (B): $^{208}Pb/^{204}Pb$ vs. $^{206}Pb/^{204}Pb$; (C) $^{207}Pb/^{204}Pb$ vs. $^{208}Pb/^{204}Pb$. Symbols highlight different sulfide phases, showing the heterogeneity of all sulfides (in particular, sphalerite and pyrite being most heterogeneous). The inset in (B) is a zoom of the galena cluster field (galena uncertainties smaller than symbols), indicating the galena samples are not homogeneous.

1) Regularities

A search for regularities is far from simple. It is true that arrays are visible in Figure 2.17–2.19. Especially in the $^{208}Pb/^{204}Pb$ vs. $^{206}Pb/^{204}Pb$ diagram (Figs. 2.17–2.19(B)) about 15 data points (mostly pyrite and sphalerite) appear to lie on a negative correlation trend. The radiogenic Pb isotopes would not be produced in situ in the Janggun deposit, as neither U nor Th are likely to be carried by S-bearing fluids. Therefore, the observed scatter reflects different leaching episodes of the country rock or different host rocks by the S-bearing fluids. The distribution of points allows constraining the number of such fluid circulation episodes. We shall address the following questions: (1) to what extent does the prominent trend of $^{206}Pb/^{204}Pb$ vs. $^{208}Pb/^{204}Pb$ (Figs. 2.17–

2.19(B)) find support in $^{206}Pb/^{204}Pb$ vs. $^{207}Pb/^{204}Pb$ (Figs. 2.17–2.19(A))? (2) how many end-members are required to account for the data distribution? (3) do the inferred end-members display some regularity, which would correlate with the microscopic grouping into four assemblages that reflect variable alteration and relict phases?

The negative linear trend of $^{206}Pb/^{204}Pb$ vs. $^{208}Pb/^{204}Pb$ (Figs. 2.17–2.19(B)) could, in principle, be due to mixing two Pb sources: one source with a low time-integrated ^{208}Pb production (i.e., Pb derived from a country rock with low Th concentration and/or a low age) and at the same time a high time-integrated ^{206}Pb production; a second source with higher time-integrated ^{208}Pb production and a lower time-integrated ^{206}Pb production. If this were the case, one would expect the $^{207}Pb/^{206}Pb$ ratio (Figs. 2.17–2.19(C)) to follow a similarly regular correlation trend. However, Figures 2.17–2.19(A) show no single trend. Moreover, the points that are arrayed in Figures 2.17–2.19(B) are scattered around the diagram in Figures 2.17–2.19(A). The $^{207}Pb/^{206}Pb$ ratio gives the average age of the crust that was leached by the S-bearing fluids; this age is variable, without a connection to sample location (Fig. 2.18). A possible link to the sulfide phase (Fig. 2.17) is addressed in the next subsection.

2) Number of end-members

The minimum polygon that is required to enclose any dispersed point distribution is the triangle, which requires at least three end-members. As pointed out by Villa (2001, his Fig. 2), the number of apparent end-members of a three-dimensional point cloud, such as that of the present data, may be reduced by the projection onto a two-dimensional graph. The way to ascertain this effect is to check if the extreme points in one projection plane remain the extreme points in a different projection plane. The present data suggest three end-members in the $^{206}Pb/^{204}Pb$ - $^{208}Pb/^{204}Pb$ projection (Figs. 2.17-2.19(B)): one at the lower right (sphalerite N433 and N478), one at the lower left (pyrrhotite N433) and one at the top centre (pyrite N478). Apart from the fact that two samples account for all three apparent end-members (we will return to this point in section of 'Connection with petrography'), not all of these three points are extremes in the $^{206}Pb/^{204}Pb$ - $^{207}Pb/^{204}Pb$ projection (Figs. 2.17–2.19(A)). Pyrrhotite N433 remains a vertex point, but the two sphalerite at high $^{206}Pb/^{204}Pb$ are no longer overlapping (which means that at least one of them requires the admixture of an additional end-member), and the vertex at the top center now appears to be sphalerite N435.

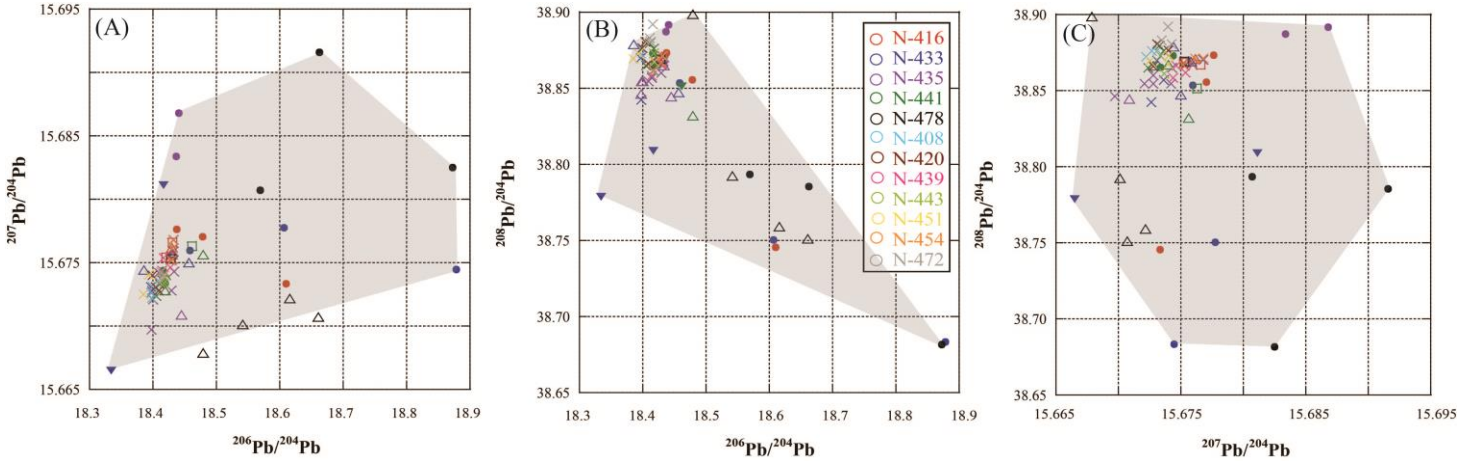

Figure 2.18. Pb isotope correlation diagrams for the samples of the North orebody. (A): $^{207}Pb/^{204}Pb$ vs. $^{206}Pb/^{204}Pb$; (B): $^{208}Pb/^{204}Pb$ vs. $^{206}Pb/^{204}Pb$; (C) $^{207}Pb/^{204}Pb$ vs. $^{208}Pb/^{204}Pb$. Symbols highlight different samples, showing that the end-members (the vertices of the polygonal shadows) are different in different projections of Pb isotopic diagrams.

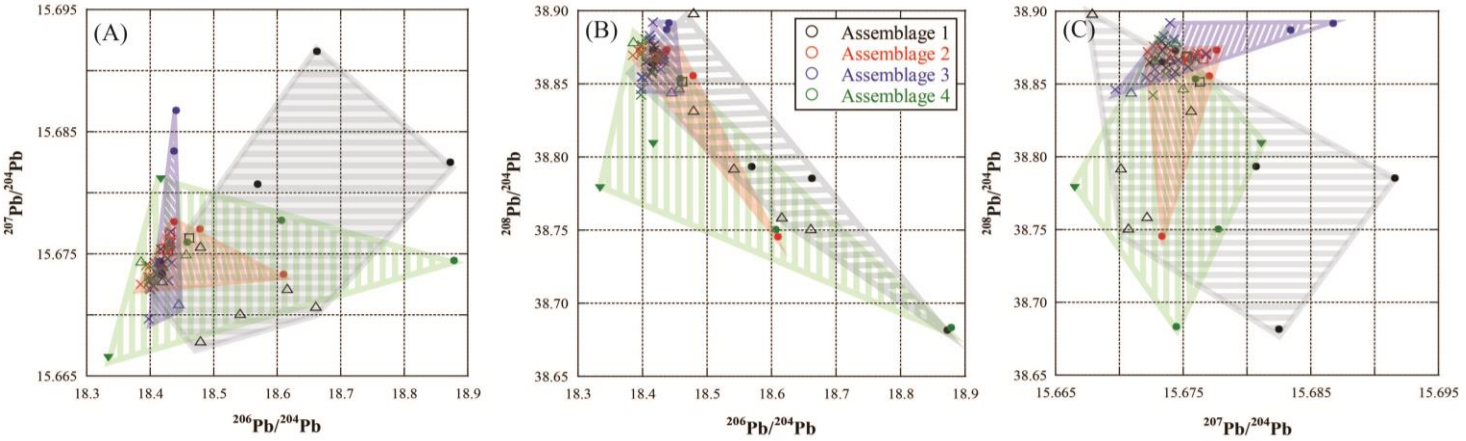

Figure 2.19. Pb isotope correlation diagrams for the samples of the North orebody. (A): $^{207}Pb/^{204}Pb$ vs. $^{206}Pb/^{204}Pb$; (B): $^{208}Pb/^{204}Pb$ vs. $^{206}Pb/^{204}Pb$; (C) $^{207}Pb/^{204}Pb$ vs. $^{208}Pb/^{204}Pb$. Symbols highlight the different mineral assemblages listed in Table 2, showing that all assemblages overlap without a clear regularity.

In the $^{207}Pb/^{204}Pb$ - $^{208}Pb/^{204}Pb$ projection (Figs. 2.17–2.19(C)) the points are distributed in a hexagon and forcing the data into a minimum triangle would require end-members that are far away from all measured points. What is more remarkable is that two sphalerite samples from the same 2x4 cm polished section, N478, are contiguous vertices of the hexagon - one cannot derive from the other by admixing any of the remaining points. In summary, at least seven or eight end-members are inferred from the three orthogonal projections. Each end-member represents a separate fluid event, as is evident from the isotopic diversity.

3) Connections with petrography

As mentioned in the mineralogy paragraph, the samples can be classified in four assemblages characterized by different sulfide mineral occurrences, abundances, and textures (Table 2.3), which result from substitution reactions, i.e. fluid events. At the very least two fluid events are necessary: one consuming pyrrhotite and another creating marcasite at a later stage, in a different spatial localization. If this inventory were approximately complete, one would observe some relation of the isotopic data to the mineral assemblage. Instead, Figure 2.19 show no regularity if samples are broken down according to the assemblages. For example, Group 1 (the most "pristine") is shifted off-center, extending over almost the entire isotopic variation range but without ever coinciding with one of the vertices discussed in section of 'Number of end-members'. This dispersion forces the conclusion that in the early stages of the formation of the Janggun deposit there was a large number of separate fluid percolation events. At the end of this period, the mineral assemblage that we classified as most pristine was able to survive, carrying with it a very substantial genetic heterogeneity. More radiogenic $^{206}Pb/^{204}Pb$ values of in samples belonging to assemblages 1 and 3 (Table 2.3) point to a greater involvement of older (and/or U-rich) crust in the generation of the early fluids.

Galena carries a very high Pb concentration. If it had been present since the beginning of mineralization, it would have buffered the isotopic composition of all fluids that came into contact with it, resulting in a star-like trend of data points that depart radially from the "galena point" towards the point representing each incoming fluid. In broad terms, this is observed; however, galena itself is heterogeneous at the 50 sigma level. Two generations of galena are described by petrography, but this is clearly an oversimplification, as the scattered distribution of galena (Inset in Fig. 2.17(B)) requires at the very least three galena-forming fluid events (see section 'Number

of end-members'). Moreover, galena rarely belongs to the earliest assemblages. At most one among the galena generations does belong to the earliest assemblages (it is only observed in the sample which have pyrrhotite, N-420 and N-433) (Fig. 2.12).

The final fluid event, which created the fine aggregates with/without bird's eye texture of pyrite + marcasite-bearing assemblages 2, resulted in less heterogeneous isotope ratios in comparison with the assemblages 1, 3 and 4. However, if one assumes that there existed one well-defined pyrite+marcasite-forming fluid, it follows that samples belonging to assemblage 2 (N408, N416, N451, N454) must have constant Pb isotopic compositions, which is not observed (Fig. 2.19). Totsuka et al., (2019) shows that Pb isotopic compositions observed is not related to the mineral assemblage and texture/morphology of galena phases, and suggests the Pb isotopic compositions record those of hydrothermal fluids when the galena grains were mineralized. They also found that two different sites of Pb isotopic compositions are all mixed and heterogeneous, suggesting that Pb signature is controlled by the fluids circulated a long distance rather than the sediments immediate proximity. We also observed the Pb isotopic compositions heterogeneity of our sulfide are not associated with mineralogy (texture, paragenesis, and assemblages), suggesting they are primary. The fact that we have a sequence of textural-age relationships among sulfides indicates that some assemblages were more modified than others, but as the alteration occurred over several pulses, we do not observe a match between the assemblages and Pb isotopic compositions (Fig. 2.19).

2.4.3.2. Comparison between the North orebody and the South A orebody

One sample from the South A orebody was also measured to compare its Pb isotopic composition with the North orebody. A total of 13 sulfide analyses from this one sample are shown in Table 2.5 and Figure 2.20. The comparison shows a general proximity, but the differences are very well resolved, both within the one South A orebody sample and between the latter and the 12 samples from the North orebody. In the $^{207}Pb/^{204}Pb$ vs. $^{206}Pb/^{204}Pb$ diagram (Fig. 2.20(A)), the sulfides from the South A sample are aligned mid-way between the "galena field" of Figure 2.17–2.19(A) and sphalerite N478. However, in the $^{208}Pb/^{204}Pb$ vs. $^{206}Pb/^{204}Pb$ diagram (Fig. 2.20(B)) the South A minerals lie outside any minimum polygon inferred from Figure 2.20(A) and appear to suggest a (disturbed) collinearity with pyrite N478.

Table 2.5. Lead isotopic composition of sulfides from the North and South orebodies. Individual errors represent within run uncertainties at the 95% confidence level

1. North orebody

# sample	# mineral	$^{206}Pb/^{204}Pb$	StdErr (2σ)	$^{207}Pb/^{204}Pb$	StdErr (2σ)	$^{208}Pb/^{204}Pb$	StdErr (2σ)	$^{207}Pb/^{206}Pb$	StdErr (2σ)	$^{208}Pb/^{206}Pb$	StdErr (2σ)
	Sphalerite	**18.437**	0.001	**15.678**	0.001	**38.873**	0.003	**0.85031**	0.00002	**2.10839**	0.00008
	Sphalerite	**18.610**	0.011	**15.673**	0.010	**38.746**	0.026	**0.84224**	0.00006	**2.08210**	0.00015
	Sphalerite	**18.478**	0.002	**15.677**	0.002	**38.855**	0.006	**0.84843**	0.00006	**2.10275**	0.00017
	Pyrite	**18.430**	0.001	**15.676**	0.001	**38.871**	0.002	**0.85058**	0.00001	**2.10916**	0.00005
N416	Pyrite	**18.430**	0.001	**15.676**	0.001	**38.869**	0.002	**0.85053**	0.00001	**2.10896**	0.00005
	Arsenopyrite	**18.431**	0.001	**15.677**	0.001	**38.867**	0.002	**0.85058**	0.00003	**2.10882**	0.00006
	Arsenopyrite	**18.421**	0.001	**15.675**	0.001	**38.869**	0.003	**0.85097**	0.00002	**2.11005**	0.00006
	Galena	**18.431**	0.001	**15.675**	0.001	**38.866**	0.003	**0.85050**	0.00002	**2.10881**	0.00007
	Galena	**18.427**	0.001	**15.675**	0.001	**38.868**	0.003	**0.85066**	0.00002	**2.10929**	0.00006
	Sphalerite	**18.458**	0.002	**15.676**	0.002	**38.853**	0.005	**0.84927**	0.00002	**2.10495**	0.00011
	Sphalerite	**18.879**	0.007	**15.674**	0.006	**38.683**	0.014	**0.83038**	0.00006	**2.04928**	0.00016
	Sphalerite	**18.607**	0.007	**15.678**	0.006	**38.750**	0.015	**0.84260**	0.00006	**2.08241**	0.00013
	Pyrite	**18.386**	0.001	**15.674**	0.001	**38.879**	0.002	**0.85250**	0.00001	**2.11458**	0.00004
	Pyrite	**18.457**	0.002	**15.675**	0.002	**38.847**	0.005	**0.84930**	0.00003	**2.10482**	0.00011
N433	Pyrite	**18.430**	0.001	**15.676**	0.001	**38.869**	0.002	**0.85056**	0.00001	**2.10901**	0.00005
	Pyrrhotite	**18.417**	0.009	**15.681**	0.008	**38.809**	0.019	**0.85129**	0.00013	**2.10671**	0.00030
	Pyrrhotite	**18.334**	0.001	**15.667**	0.001	**38.779**	0.003	**0.85447**	0.00001	**2.11505**	0.00006
	Galena	**18.397**	0.001	**15.673**	0.001	**38.870**	0.003	**0.85195**	0.00002	**2.11287**	0.00006
	Galena	**18.397**	0.002	**15.673**	0.001	**38.842**	0.006	**0.85189**	0.00002	**2.11136**	0.00006
	Galena	**18.414**	0.001	**15.674**	0.001	**38.857**	0.002	**0.85118**	0.00001	**2.11020**	0.00006
	Sphalerite	**18.437**	0.001	**15.683**	0.001	**38.887**	0.003	**0.85065**	0.00002	**2.10924**	0.00009
	Sphalerite	**18.441**	0.002	**15.687**	0.002	**38.892**	0.005	**0.85065**	0.00002	**2.10896**	0.00009
	Pyrite	**18.445**	0.002	**15.671**	0.001	**38.844**	0.004	**0.84962**	0.00002	**2.10600**	0.00009
	Galena	**18.409**	0.002	**15.674**	0.001	**38.855**	0.004	**0.85145**	0.00002	**2.11067**	0.00008
	Galena	**18.432**	0.001	**15.676**	0.001	**38.868**	0.003	**0.85045**	0.00002	**2.10865**	0.00006
N435	Galena	**18.429**	0.001	**15.673**	0.001	**38.860**	0.004	**0.85046**	0.00002	**2.10869**	0.00007
	Galena	**18.400**	0.001	**15.672**	0.001	**38.855**	0.003	**0.85175**	0.00002	**2.11169**	0.00006
	Galena	**18.398**	0.001	**15.673**	0.001	**38.855**	0.003	**0.85185**	0.00002	**2.11184**	0.00008
	Galena	**18.398**	0.001	**15.670**	0.002	**38.846**	0.005	**0.85171**	0.00003	**2.11147**	0.00011
	Galena	**18.432**	0.001	**15.677**	0.001	**38.870**	0.003	**0.85051**	0.00002	**2.10878**	0.00008
	Galena	**18.433**	0.001	**15.674**	0.001	**38.865**	0.003	**0.85034**	0.00002	**2.10845**	0.00006

# sample	# mineral	$^{206}Pb/^{204}Pb$	StdErr (2σ)	$^{207}Pb/^{204}Pb$	StdErr (2σ)	$^{208}Pb/^{204}Pb$	StdErr (2σ)	$^{207}Pb/^{206}Pb$	StdErr (2σ)	$^{208}Pb/^{206}Pb$	StdErr (2σ)
N441	Sphalerite	**18.420**	0.001	**15.673**	0.001	**38.865**	0.002	**0.85091**	0.00001	**2.10999**	0.00005
	Sphalerite	**18.416**	0.001	**15.674**	0.001	**38.873**	0.002	**0.85113**	0.00002	**2.11084**	0.00006
	Pyrite	**18.479**	0.002	**15.676**	0.001	**38.832**	0.005	**0.84829**	0.00004	**2.10143**	0.00016
	Pyrite	**18.419**	0.001	**15.674**	0.001	**38.867**	0.002	**0.85094**	0.00001	**2.11015**	0.00005
	Pyrite	**18.419**	0.001	**15.673**	0.001	**38.866**	0.002	**0.85092**	0.00001	**2.11018**	0.00006
	Arsenopyrite	**18.462**	0.001	**15.676**	0.002	**38.852**	0.005	**0.84913**	0.00003	**2.10447**	0.00009
	Galena	**18.411**	0.001	**15.673**	0.001	**38.879**	0.002	**0.85132**	0.00001	**2.11179**	0.00005
	Galena	**18.405**	0.001	**15.672**	0.001	**38.865**	0.002	**0.85152**	0.00002	**2.11167**	0.00006
	Galena	**18.418**	0.001	**15.674**	0.001	**38.876**	0.003	**0.85101**	0.00001	**2.11081**	0.00006
N478	Sphalerite	**18.872**	0.014	**15.683**	0.012	**38.681**	0.032	**0.83096**	0.00009	**2.04935**	0.00040
	Sphalerite	**18.663**	0.007	**15.692**	0.006	**38.786**	0.017	**0.84079**	0.00009	**2.07822**	0.00041
	Sphalerite	**18.569**	0.005	**15.681**	0.005	**38.793**	0.017	**0.84442**	0.00007	**2.08914**	0.00043
	Pyrite	**18.616**	0.005	**15.672**	0.005	**38.759**	0.012	**0.84188**	0.00005	**2.08207**	0.00021
	Pyrite	**18.479**	0.002	**15.668**	0.002	**38.899**	0.005	**0.84788**	0.00003	**2.10500**	0.00011
	Pyrite	**18.542**	0.003	**15.670**	0.003	**38.793**	0.007	**0.84512**	0.00005	**2.09217**	0.00012
	Pyrite	**18.661**	0.005	**15.671**	0.003	**38.751**	0.009	**0.83982**	0.00004	**2.07660**	0.00018
	Arsenopyrite	**18.429**	0.001	**15.675**	0.001	**38.869**	0.004	**0.85060**	0.00002	**2.10917**	0.00007
N408	Galena	**18.397**	0.001	**15.673**	0.001	**38.876**	0.002	**0.85190**	0.00001	**2.11313**	0.00005
	Galena	**18.398**	0.001	**15.672**	0.001	**38.872**	0.003	**0.85184**	0.00002	**2.11283**	0.00007
	Galena	**18.399**	0.001	**15.673**	0.001	**38.876**	0.003	**0.85186**	0.00002	**2.11299**	0.00006
N420	Galena	**18.404**	0.001	**15.673**	0.001	**38.880**	0.002	**0.85161**	0.00001	**2.11260**	0.00005
	Galena	**18.410**	0.001	**15.673**	0.001	**38.866**	0.002	**0.85134**	0.00001	**2.11115**	0.00005
	Galena	**18.399**	0.001	**15.674**	0.001	**38.876**	0.002	**0.85190**	0.00002	**2.11298**	0.00005
N439	Galena	**18.417**	0.001	**15.675**	0.001	**38.862**	0.002	**0.85116**	0.00002	**2.11014**	0.00006
	Galena	**18.414**	0.001	**15.674**	0.001	**38.858**	0.002	**0.85123**	0.00002	**2.11028**	0.00005
	Galena	**18.427**	0.001	**15.675**	0.001	**38.866**	0.002	**0.85062**	0.00002	**2.10915**	0.00005
N443	Galena	**18.417**	0.001	**15.673**	0.001	**38.873**	0.003	**0.85102**	0.00002	**2.11070**	0.00006
	Galena	**18.417**	0.001	**15.674**	0.001	**38.861**	0.002	**0.85104**	0.00001	**2.11006**	0.00006
N451	Galena	**18.385**	0.001	**15.672**	0.001	**38.869**	0.003	**0.85247**	0.00002	**2.11420**	0.00007
	Galena	**18.393**	0.001	**15.674**	0.001	**38.873**	0.003	**0.85216**	0.00002	**2.11342**	0.00007
	Galena	**18.418**	0.001	**15.674**	0.001	**38.867**	0.003	**0.85103**	0.00002	**2.11030**	0.00006
N454	Galena	**18.431**	0.001	**15.676**	0.001	**38.871**	0.002	**0.85055**	0.00002	**2.10902**	0.00005
	Galena	**18.432**	0.001	**15.677**	0.001	**38.871**	0.002	**0.85053**	0.00001	**2.10893**	0.00005
	Galena	**18.430**	0.001	**15.675**	0.001	**38.867**	0.002	**0.85053**	0.00002	**2.10890**	0.00004
N472	Galena	**18.416**	0.001	**15.674**	0.001	**38.892**	0.003	**0.85111**	0.00001	**2.11186**	0.00006
	Galena	**18.413**	0.001	**15.674**	0.001	**38.881**	0.002	**0.85127**	0.00002	**2.11164**	0.00006
	Galena	**18.411**	0.001	**15.673**	0.001	**38.883**	0.003	**0.85132**	0.00002	**2.11197**	0.00006

2. South orebody

# sample	# mineral	$^{206}Pb/^{204}Pb$	StdErr (2σ)	$^{207}Pb/^{204}Pb$	StdErr (2σ)	$^{208}Pb/^{204}Pb$	StdErr (2σ)	$^{207}Pb/^{206}Pb$	StdErr (2σ)	$^{208}Pb/^{206}Pb$	StdErr (2σ)
S150	Pyrite	**18.529**	0.001	**15.683**	0.001	**38.938**	0.003	**0.84644**	0.00001	**2.10153**	0.00007
	Pyrite	**18.567**	0.002	**15.683**	0.002	**38.919**	0.005	**0.84471**	0.00003	**2.09619**	0.00010
	Mrc+Py	**18.532**	0.001	**15.684**	0.001	**38.930**	0.007	**0.84631**	0.00003	**2.10072**	0.00029
	Mrc+Py	**18.530**	0.001	**15.681**	0.001	**38.929**	0.003	**0.84628**	0.00002	**2.10092**	0.00008
	Arsenopyrite	**18.532**	0.001	**15.682**	0.001	**38.930**	0.003	**0.84615**	0.00002	**2.10061**	0.00007
	Arsenopyrite	**18.539**	0.003	**15.683**	0.001	**38.934**	0.007	**0.84601**	0.00008	**2.10009**	0.00027
	Sphalerite	**18.539**	0.001	**15.683**	0.001	**38.935**	0.003	**0.84596**	0.00002	**2.10018**	0.00008
	Sphalerite	**18.556**	0.001	**15.686**	0.001	**38.942**	0.004	**0.84534**	0.00002	**2.09858**	0.00008
	Po+Mrc	**18.525**	0.001	**15.682**	0.001	**38.934**	0.002	**0.84653**	0.00001	**2.10172**	0.00006
	Po+Mrc+Gn	**18.523**	0.001	**15.680**	0.001	**38.928**	0.003	**0.84649**	0.00002	**2.10156**	0.00005
	Galena	**18.532**	0.001	**15.682**	0.001	**38.930**	0.002	**0.84618**	0.00002	**2.10066**	0.00007
	Galena	**18.519**	0.001	**15.680**	0.001	**38.927**	0.003	**0.84666**	0.00002	**2.10198**	0.00006
	Galena	**18.519**	0.001	**15.679**	0.001	**38.926**	0.002	**0.84667**	0.00002	**2.10201**	0.00006

At first sight, the North orebody sample apparently related to the South orebody sample is the same, N478. However, the Pb isotopic compositions of its sulfides are in massive mutual disequilibrium and neither pyrite N478 nor sphalerite N478 (Fig. 2.17–2.19) remain credible end-members in the other diagrams of Figure 2.20. Evidently, fluid pulses of different chemical and isotopic compositions circulated at different times in different places.

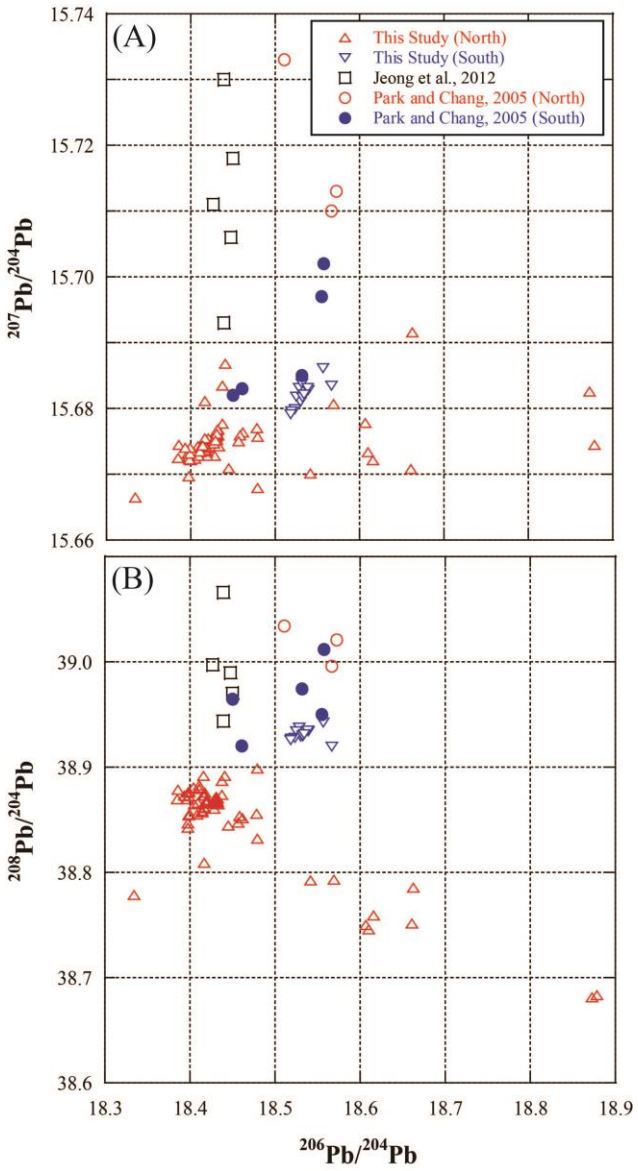

Figure 2.20. Comparison of Pb isotopic compositions between the North and South orebodies analyzed here, and from literature (Park and Chang, 2005; Jeong et al., 2005). (A) $^{207}Pb/^{204}Pb$ vs. $^{206}Pb/^{204}Pb$; (B) $^{208}Pb/^{204}Pb$ vs. $^{206}Pb/^{204}Pb$. Pb isotopic compositions between different orebodies show a general proximity, but the differences are very well resolved. The literature results and the present ones are vaguely similar, but fall into clearly distinct compositional fields. Polygonal shadows represent the fields of the data measured in this study.

2.4.3.3. Comparison with literature data

Figure 2.20 includes two literature data sets of the Janggun mine from Park and Chang (2005) and Jeong et al. (2012) together with the data obtained here. Park and Chang (2005) reported the Pb data from the North (N=3) and South (N=5) orebodies separately, whereas Jeong et al. (2012) reported five measurements without indicating their sampling localities within the mine. No attempt was made to correct the literature data in Figure 2.20 for fractionation using NIST SRM 981.

The literature data are vaguely similar to the present ones, but fall into clearly distinct compositional fields. Especially the $^{207}Pb/^{204}Pb$ ratio has a much higher variation range (Fig. 2.20(A)) than that of the samples reported here. The literature data also show substantially higher $^{208}Pb/^{204}Pb$ ratios (Fig. 2.20(B)), whereas the spread in $^{206}Pb/^{204}Pb$ is smaller (possibly due to the smaller number of analyzed samples). Two of the South orebody samples of Park and Chang (2005) appear similar to the five data-points of Jeong et al. (2012), whereas the remaining six samples of Park and Chang (2005) do not overlap with them and also suggest a difference between the fields of the North and South orebody in the $^{207}Pb/^{204}Pb$ vs $^{206}Pb/^{204}Pb$ diagram (Fig. 2.20(A)), but not in the $^{208}Pb/^{204}Pb$ vs $^{206}Pb/^{204}Pb$ diagram (Fig. 2.20(B)). The number of analyses being small, it would be premature to identify end-members from them, but it is quite clear that the literature samples require yet more end-members in addition (and/or partial substitution) to those required by Figures 2.17–2.19.

The Pb isotope data obtained here are plotted in the Pb evolution model (Kramers and Tolstikhin, 1997). The uranogenic diagram in Figure 2.21(A) shows that our data lie between Young Upper Crust (YUC) and Old Upper Crust (OUC), representing young juvenile source of recent age and old reworked (Precambrian) basement, respectively. This result, which is common to many ore deposits worldwide, is explained by the fact that even in a magmatic halo near the apex of a pluton the fluids are never monogenetically derived from the magma but always interact with the country rocks. The apparent age of the old basement is not uniquely constrained by the diagram, as it depends on the assumption whether the Late Jurassic granite near Janggun ore mineralization that exsolved the sulfidic fluids had a purely crustal or a purely mantle origin, or an intermediate one. In the former case, the galena average would be produced by an admixture of the magmatic signature ($^{206}Pb/^{204}Pb \approx 18.63$) with that of old basement having $^{206}Pb/^{204}Pb \approx 17.7$,

i.e. an age of c. 1.3 Ga. In the latter case, the mantle signature would be $^{206}Pb/^{204}Pb \approx 18.21$, requiring admixture with a 0.7 Ga old basement. An intermediate Jurassic magma would require an OUC contaminant of intermediate age. In the $^{208}Pb/^{204}Pb$ vs. $^{206}Pb/^{204}Pb$ diagram (Fig. 2.21(B)) the Pb isotopic compositions observed here lie above YUC, suggesting that the local fluid source of the study area is different from the average continental crust, reflecting a higher time-integrated ^{208}Pb contribution from Th.

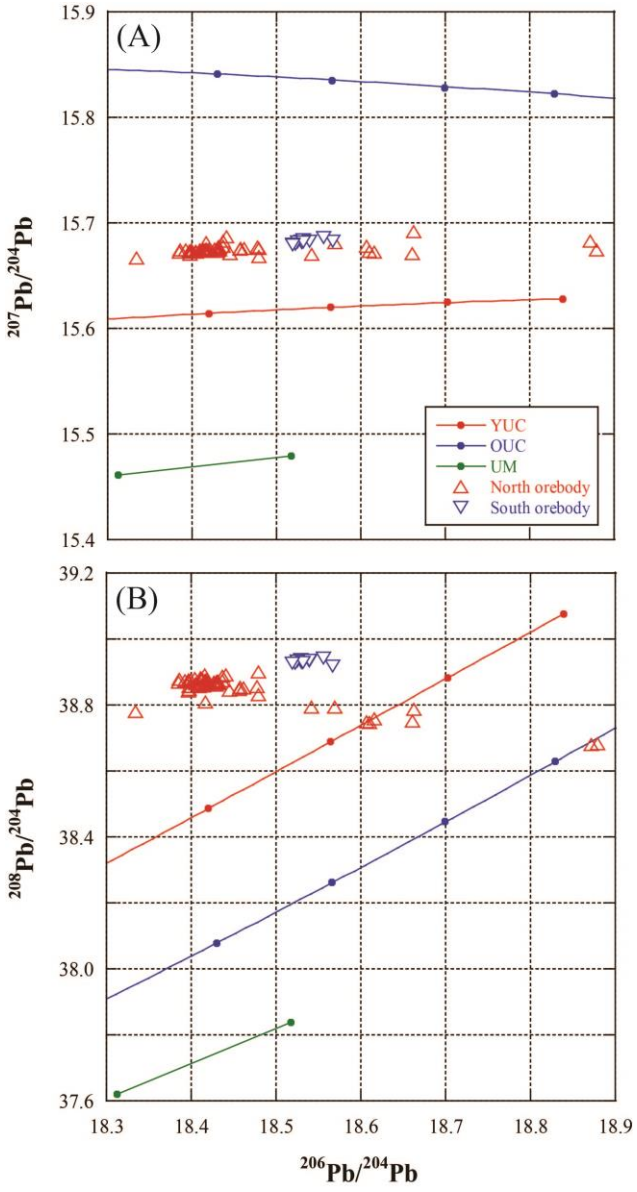

Figure 2.21. Pb isotope correlation diagrams for sulfides from the two orebodies plotted in Pb evolution model (Kramers and Tolstikhin, 1997). The tick marks represent 0.1 Ga intervals. The blue line represents the modelled evolution of the Old Upper Crust (OUC) between ca. 0.45 and

0.85 Ga before present. The red line illustrates the modelled evolution of the Young Upper Crust (YUC) in the last 0.35 Ga. The green line represents the Upper Mantle (UM) in the last 100 Ma. (A) $^{207}Pb/^{204}Pb$ vs. $^{206}Pb/^{204}Pb$; the data lie between YUC and OUC, representing young juvenile source and old reworked basement; (B) $^{208}Pb/^{204}Pb$ vs. $^{206}Pb/^{204}Pb$; the data lie above YUC, suggesting that the local fluid source of the study area is different from the average continental crust.

2.4.4. S isotopic compositions

As pyrite samples show the largest variations in Pb isotopic composition, it was deemed important to define the sulfur isotopic composition of the same grains to provide complementary information to the Pb isotope analyses. As described in the Analytical Methods section, nine pyrite samples from four different rocks were obtained by micro-drilling in the same place as the samples previously micro-drilled for Pb analyses. In addition to pyrite, the sulfur isotopic composition of two sphalerite samples from two of the four rocks micro-drilled for pyrite was also analyzed. Results are given in Table 2.6 with standard deviation.

Table 2.6. Sulfur isotope composition of pyrite and sphalerite from the North orebody (unit: ‰)

# sample	# mineral	$\delta^{34}S$	Std (2σ)
N441	Pyrite	5.7	0.111
	Pyrite	5.2	0.033
N433	Pyrite	6.0	0.079
	Pyrite	6.2	0.035
	Sphalerite	4.6	0.197
N416	Pyrite	5.6	0.021
	Pyrite	5.3	0.062
N478	Pyrite	6.1	0.045
	Pyrite	6.0	0.072
	Pyrite	4.4	0.130
	Sphalerite	5.3	0.073

Kim and Nakai (1980), Lee (1985), and Kim (1986) have performed sulfur isotope analyses on a total of 38 sulfide minerals from the Janggun mine as shown in Figure 2.22. $\delta^{34}S$ values of Kim and Nakai (1980) range from +3 to +4.6 ‰; Lee (1985) = -0.5 to +3.2 ‰, and Kim (1986) = -0.3 to +5.2 ‰.

The $\delta^{34}S$ values of sphalerite obtained here marginally overlap with the $\delta^{34}S$ range from the literature, extending it to higher values. However, the present $\delta^{34}S$ values of pyrite range

between (+4.4 ± 0.1) ‰ and (+6.2 ± 0.1) ‰, higher than those from the literatures (Fig. 2.21). This may be either a standardization bias (neither of the 1980s papers details the used reference materials) or a real difference. The latter is not surprising, as even larger $\delta^{34}S$ variation within individual deposits had already been reported (e.g. Bell et al., 2015; Esteban-Arispe et al., 2016). In our case this may indicate that our samples were more affected by fluid enriched in ^{34}S from sediment components. Since the sample locations in the literatures are not the identical with those in the present study, we conclude that the sulfur isotope compositions are as broadly variable in space as are the Pb isotopic compositions. We propose that both isotopic systems were controlled by similar processes, such as different mixing proportions of a large number of different sources for the dissolved load in multiple generations of the ore-bearing fluids, which resulted in the observed multiple (replacive) generations of sulfides listed in Figure 2.14.

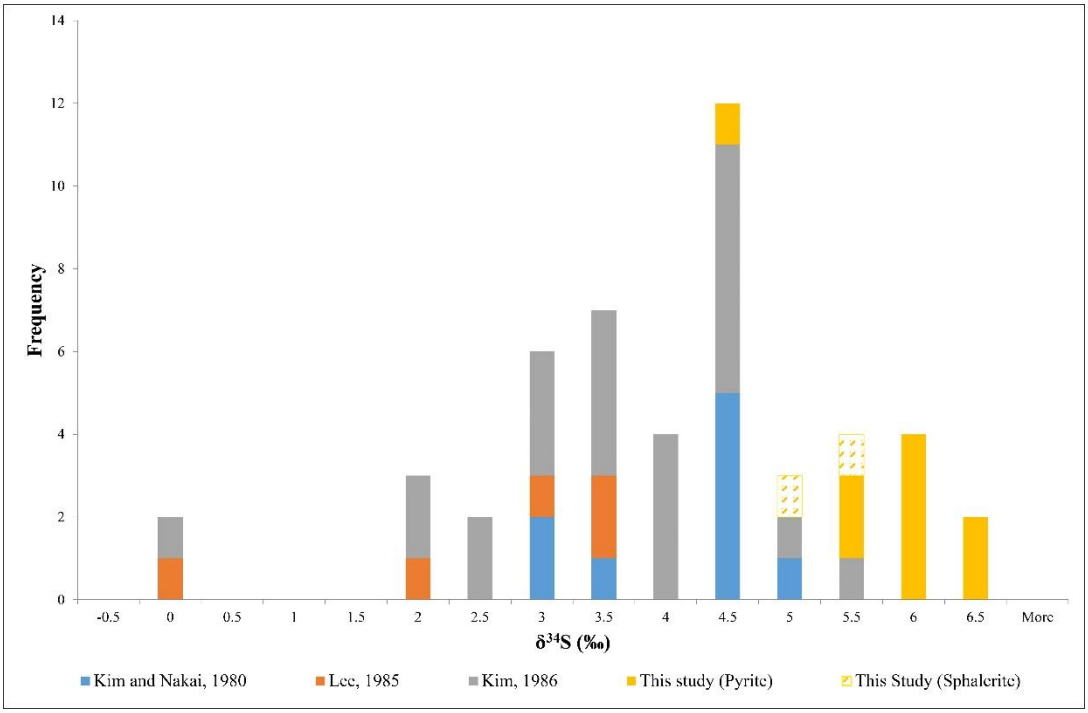

Figure 2.22. Sulfur isotopic composition of Janggun sulfides (given as $\delta^{34}S$ relative to VPDB). The results obtained in this work, (yellow bars) are offset from those obtained on samples from other locations in the mine (Kim and Nakai, 1980; Lee, 1985; Kim, 1986), and show a similar spread.

This genetic model is supported by the observations that pyrite in sample N478 shows discrepant $\delta^{34}S$ values at the cm scale, namely 4.4±0.1 ‰, 6.0±0.1 ‰, and 6.1±0.1 ‰ (Table 2.6). Seal (2006) proposed that sulfur isotope compositions of individual grains or even growth zones can differ from the bulk composition due to Rayleigh fractionation, depending on when the grain formed in the mineralization sequence. An additional, probably vastly predominant cause of isotopic heterogeneity, viz. several variable fluid circulation events, is supported by the Pb isotopic compositions and trace element data.

Equilibrium temperatures of mineralization were calculated from the sulfur isotopic compositions of pairs of coexisting sulfide minerals by Kim and Nakai (1980), Lee (1985), and Kim (1986); they ranged from 421 to 445 °C, 341 to 375 °C, and 288 to 343 °C, respectively. Taking into account our observations of very small-scale chemical and isotopic disequilibrium in the Janggun sulfides, equilibrium isotopic thermometry appears questionable. Indeed, fluid inclusions in quartz give much lower temperatures for the hydrothermal event, 200-350 °C (Lee, 1985).

Kim and Nakai (1980) proposed that ^{34}S enrichment follows a general equilibrium trend for sulfide minerals: pyrite > sphalerite > pyrrhotite > chalcopyrite > galena. However, the present results do not conform to this prediction. Even though the number of sphalerite samples was small, the $\delta^{34}S$ of one pyrite in sample N478 is lower than that of the sphalerite, reinforcing the clear evidence of disequilibrium in Janggun.

The combination of Pb and S isotope variations reveal the complexity of the genesis of the Janggun deposit. By analogy with present-day active hydrothermal systems in the upper crust (e.g., Larderello: Farina et al., 2018; Bulle et al., 2020), a km-size deposit with a multitude of ore types, such as the Janggun field, resulted from a long-lasting, polyphase fluid circulation history. On the basis of petrographic observations of replacement textures and of Pb isotope systematics, we had identified a minimum number of end-members, each of which can be referred to a separate fluid circulation event that had leached different segments of the surrounding country rocks. The criteria for the identification of an end-member were that the respective data-point must lie at the end of an array of other data-points, and that it remains at the end of an array in an independent plot. This second criterion can be generalized to also include the arrays formed in diagrams that involve sulfur isotope systematics (Fig. 2.23) and trace elements (Fig. 3.3)

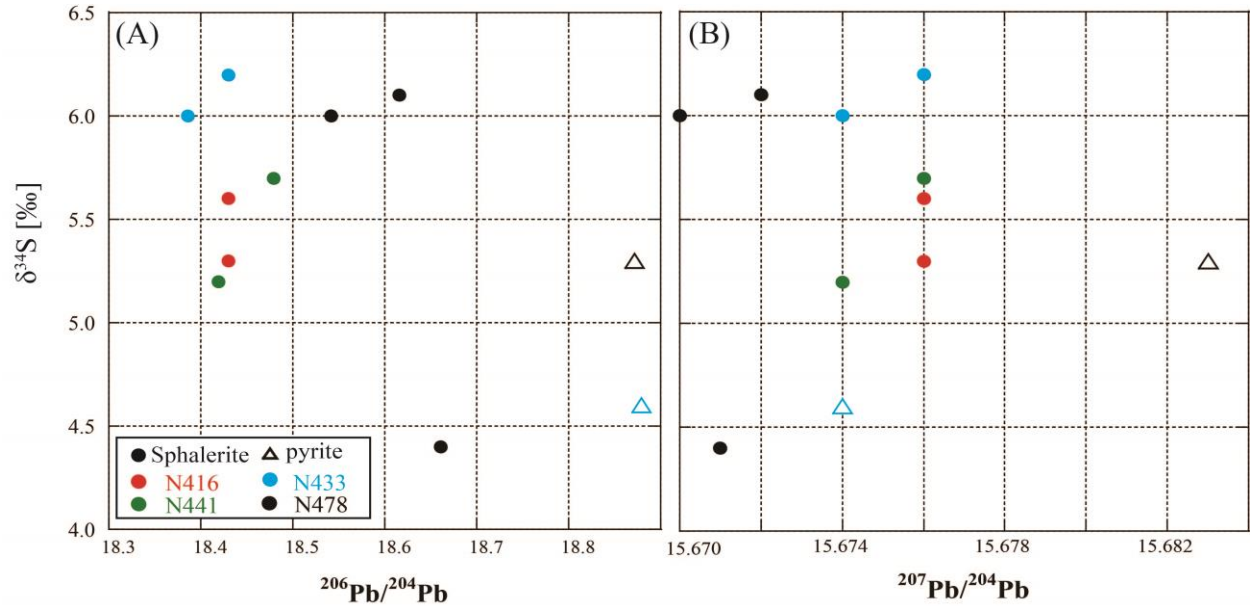

Figure 2.23. Comparison of S and Pb isotopic compositions. (A) $^{206}Pb/^{204}Pb$ vs. $\delta^{34}S$; (B) $^{207}Pb/^{204}Pb$ vs. $\delta^{34}S$ in sphalerite (circle) and pyrite (triangle), showing no systematic trend is visible.

2.5. Conclusions

1. The sulfide minerals of one level of one individual orebody of the Janggun mine were analyzed by multiple techniques.
2. The petrogenetic sequence is quite complex, as each sulfide mineral occurs in several texturally distinct generations.
3. Four characteristically distinct phase assemblages are recognized in different domains of the 100 m profile.
4. At the 10 m scale, Pb isotopic variations exceed analytical uncertainties by up to two orders of magnitude.
5. The same variation range of Pb isotopic compositions is observed at the cm scale within individual thin sections.
6. The available literature data from other locations in the Janggun mine show Pb isotopic compositions close to, but resolvably distinct from, our North Orebody data. Some of them extend trends present in our data.

7. The common-denominator Pb isotope correlation diagrams require at the very least seven isotopically well distinct fluid circulation episodes: at different times, at different temperature, and above all with different fluid circulation pathways.
8. Sulfur isotopic compositions also are heterogeneous at the cm scale and at the 10 m scale, and an overall accordance of our data to literature data from different areas of the Janggun mine.

Chapter 3

Study of Pb isotopic compositions and Whole-rock trace element geochemistry of the country rocks from the Janggun deposit in South Korea

3.1. Samples and Analytical Methods

3.1.1. Sample collection

The total of 13 samples of country rocks were collected immediately surrounding the Janggun mine (shown in Figs. 3.1 and 3.2: 5 samples of Chunyang granite, 2 samples of granophyre, 1 samples of andesic-dyke and 5 samples of Janggun limestone). There samples were measured for Pb isotopic compositions (PbIC) and trace element concentrations. Five samples of the Chunyang granite were selected, representing the petrographic observations of low and high degrees of alteration.

3.1.2. Sample preparation: Leachate fractions of country rocks

We prepared at least one leachate (L) and the corresponding residue (R), for a total of 28 analyses, including Chunyang granite (10), granophyre (4), dyke (2), and Janggun limestone (12) with 13 country rock samples. Firstly, we crushed the samples to make powder samples for effective leaching in quartz mortar.

The powdered rocks (ca. 1 – 2.5 gram) of granite, granophyre, and dyke (8 samples) were leached in 6 M HNO_3 overnight on a hotplate at 120°C in closed Savillex PFA vials. The five carbonate samples were pre-leached with cold 0.01M HCl for 30 minutes. This was performed to intend to reveal the cation pool more easily mobilized by the hydrothermal fluids. After the leaching step, leachate solutions were moved into other beakers. The remaining materials of the granite, granophyre and dyke were dissolved in hot concentrated 40% HF + 14M HNO_3.

While we tried to dissolve the remaining materials, white solids (e.g. fluorite) were found in the residue solution of granite, granophyre, and dyke samples. Thus we used 6.4M HCl acid to dissolve this phases. In the case of the remaining carbonate materials, 1M HCl acid was used to dissolve and a few drops of Piranha solution (a mixture of ammonium hydroxide (NH_4OH)) and hydrogen peroxide (H_2O_2)) were also treated to remove all organic residues. Subsequently, the leachates and residues solutions divided into two portions, respectively and were dried down on a hotplate at 100°C overnight. A half portion was for resin chromatography for Pb isotope analysis and the other half was used for trace element analyses.

3.1.3. Pb isotope analysis

After we gained the acid-leachate Pb fractions of 13 country rock powder (ca. 1 – 2.5g), Pb purification of the leachate and residue samples was perfumed. Dowex® 1 X 8 (100 – 200 mesh) was used in anion-exchange chromatography for Pb separation of country rocks. The procedure we applied here are following. First, we took up the samples with 2mL 3M HCl on a hotplate at 80°C. After we filled the resin in the column, we have steps to pre-clean the resin with 1 reservoir of Milli-Q and 1 reservoir of 6M HCl. Then we conditioned the resin with a half of reservoir with 3M HCl, followed by loading the sample solution. The loaded resin in the column was washed out to eliminate the matrix elements with a half reservoir 3M HCl, and twice of a half reservoir of 1M HBr. The sorbed Pb was collected by a half reservoir of 6M HCl. A few drops of 7M HNO_3 was added in the pure Pb fraction, whereby it forms bubbles to break up HBr. Thus, after adding drops of 7M HNO_3, we carefully shook the beakers to free these bubbles. The solution was evaporated on a hotplate at 100°C. After the dryness, we again added 2-3 drops of 6M HCl and 7M HNO_3 and dry down again to destroy organic residues and to convert the sample to the nitrate form. Finally, the sample was taken up in 1.5mL of 0.5M nitric acid for mass spectrometer.

The analyses were performed on a Neptune Plus™ MC-ICP-MS at Institut für Geologie, University of Bern. Details were described in the chapter 2 (section 2.3.3.3).

3.2.4. Trace elements analysis

The measurement for 14 trace elements (Mn, Co, Ni, Cu, Zn, Ga, As, Mo, Ag, Cd, Sb, Tl, Pb, Bi) were performed by Agilent 7700 ICP-MS at Geographisches Institut, University of Bern. As mentioned in section 2.3.3, a half portion of leachate and residue fractions of 13 country rocks were used to measure trace elements. First of all, the samples are diluted based on the references for the concentration of the granite, dyke, granophyre and limestone to protect the detectors of ICP-MS. Two gas modes are employed here, one is no introduction of gas and another is He introduction in reaction site to check and reduce interference of the element of interest. For example, to analyze arsenic (As) concentration, we measure mass 75 which ^{40}Ar (carrier gas) + ^{35}Cl (possible in the sample solution) can be detected as ^{75}As, and then if we used He gas mode, we can avoid this interference for As concentration. Thus, comparing the results between two

different gas modes are necessary to gain the desirable data. In general, these two gas modes are useful for the elements which have atomic mass less than 100.

Two internal standards were chosen, ^{103}Rh and ^{115}In, and analyze continuously together with the samples. The internal standard plays a role in having behavior similar to the line of the analyte and then in correct the instrument fractionation. Some of elements, such as Mn, Zn, Pb in some samples are too high to measure all together with other elements with good precision, i.e., they exceed the calibrated concentration ranges. We Prepared 4 standard solutions with different dilution factors, ranging between 0.102 ppb and 209.44 with multi element standard solution (Using mixture of two standard solutions; KD multi-elements solution IV and Multi-element ICP-STD solution), and thus for some samples, the further dilution was performed. Normally, the calibration range for the elements are less than 500 ppb. As well as the 28 samples, the rinsing steps, including flushing Mili-Q, 1% HNO_3, and Mili-Q in the system, are assigned in the auto sampler between samples to prevent cross-contamination (memory effects) of the system. The 2.5-3 mL solutions were needed for 4 minutes' measurement per samples for the 14 elements.

3.3. Results and Discussion

3.3.1. Pb isotopic compositions

Thirteen whole rock samples of Chunyang granite, granophyre, dyke, and Janggun limestone were analyzed, for a total of 28 leachates (L) and residues (R) measurements. The results of all leachates and residues are given in Table 3.1 and Figure 3.1 and show that the less radiogenic lead was released in the leachates, whereas the residues generally have more radiogenic compositions. Table 3.1 also includes the semi-quantitatively reconstituted unleached rock obtained by summing L+R in the (admittedly simplified) assumption that the intensity of the mass spectrometer signal was linearly proportional to the absolute Pb concentration in the L and R solutions.

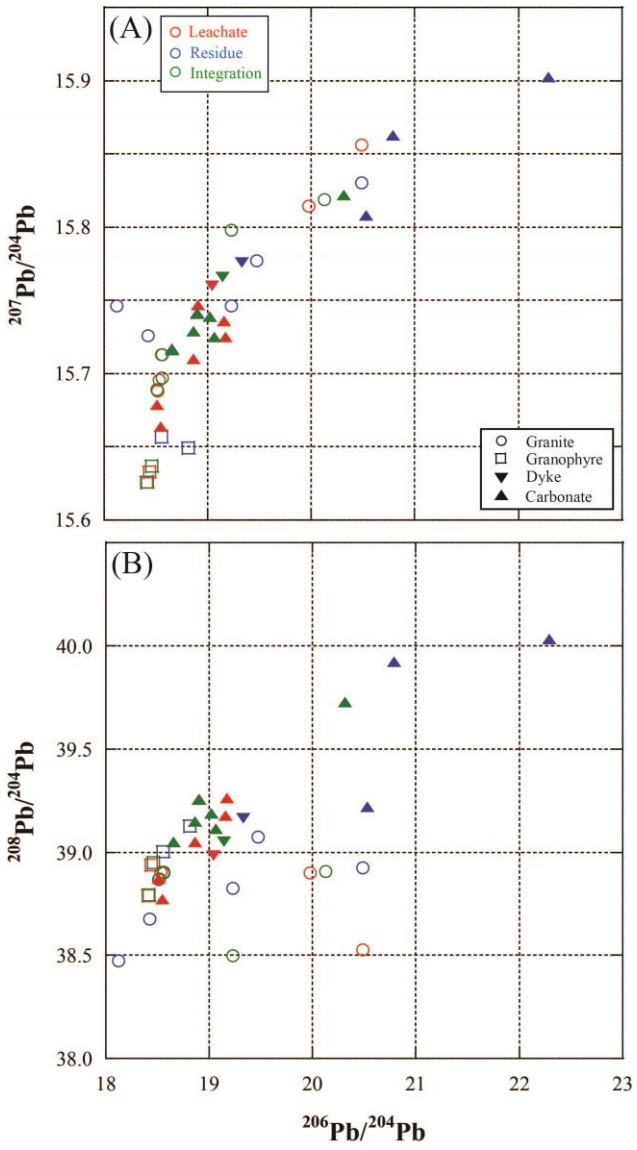

Figure 3.1. Results of leaching experiments on country rocks (Chunyang granite, granophyre, Janggun limestone, and dyke). (A) $^{207}Pb/^{204}Pb$ vs. $^{206}Pb/^{204}Pb$; (B) $^{208}Pb/^{204}Pb$ vs. $^{206}Pb/^{204}Pb$ with different colored symbols highlighting leachates (red), residues (blue), and calculated bulk rock(green).

As shown in Figure 3.1, granite leachates have lowest values for $^{206}Pb/^{204}Pb$ and $^{208}Pb/^{204}Pb$. In particular, the least altered granite shows more radiogenic $^{206}Pb/^{204}Pb$ and $^{208}Pb/^{204}Pb$ ratios, whereas the most altered granite yielded less radiogenic Pb isotope ratios, similar to those of the neighboring granophyre. On the other hand, the $^{206}Pb/^{204}Pb$ vs. $^{208}Pb/^{204}Pb$ diagram does not correspond to the petrologic observation, as high thorogenic lead is contained in the least and most

altered granite, whereas granite showing intermediate uranogenic Pb isotope ratios has low thorogenic lead. This requires that the Chunyang granite comprises at least three distinct Pb sources. The two granophyre samples show the lowest values of $^{207}Pb/^{204}Pb$. Pb isotopic compositions of dyke fall in middle of the range spanned by the other country rocks in both graphs. Janggun limestone, the host rock of Janggun mine, shows most radiogenic Pb isotopic compositions. In order to explain these high ratios, it is necessary to postulate the involvement of old basement rocks. The Precambrian Weonnam Group was reported in the literature (Cheong et al., 2000; Park and Chang, 2005) to have widely varying $^{206}Pb/^{204}Pb$ = 16.77 to 30.303, $^{207}Pb/^{204}Pb$ = 15.563 to 17.215, and $^{208}Pb/^{204}Pb$ = 35.673 to 42.951. As shown in Figure 3.2(A, C), the Pb isotopic compositions of leachates and residues obtained here correspond well to Pb isotopic compositions of the Weonnam Group, confirming that the very radiogenic Pb isotopic compositions of the limestone results from sedimentary or hydrothermal incorporation of Precambrian Pb from Weonnam Group.

Figure 3.2 presents Pb isotopic compositions of sulfide minerals together with those of four proximal country rocks. The clearest conclusion is that the Pb isotopic compositions of all sulfide minerals can be explained as mixture of these lead sources, as the field that includes all Janggun minerals is entirely surrounded by the fields of the country rocks. The different combinations of leachate solutions, each drawing its variable Pb budget from the country rocks, account for the observed Pb isotopic compositions heterogeneities. For example, Pb isotopic compositions of galena can be produced by mixture of Pb derived from granophyre and from granite; sphalerite and pyrite samples, whose Pb isotopic compositions show the widest isotopic spread, is best explained by mixing Pb deriving from granophyre, Janggun limestone, and granite. Especially, the integrated Pb isotopic compositions of one granite sample is exactly located in the end of the negative $^{208}Pb/^{206}Pb$ trend of sphalerite and pyrite. Thus, the Pb isotopic compositions confirms that the basement rock provides several of the far-field end-members inferred from Figures 2.17–2.19.

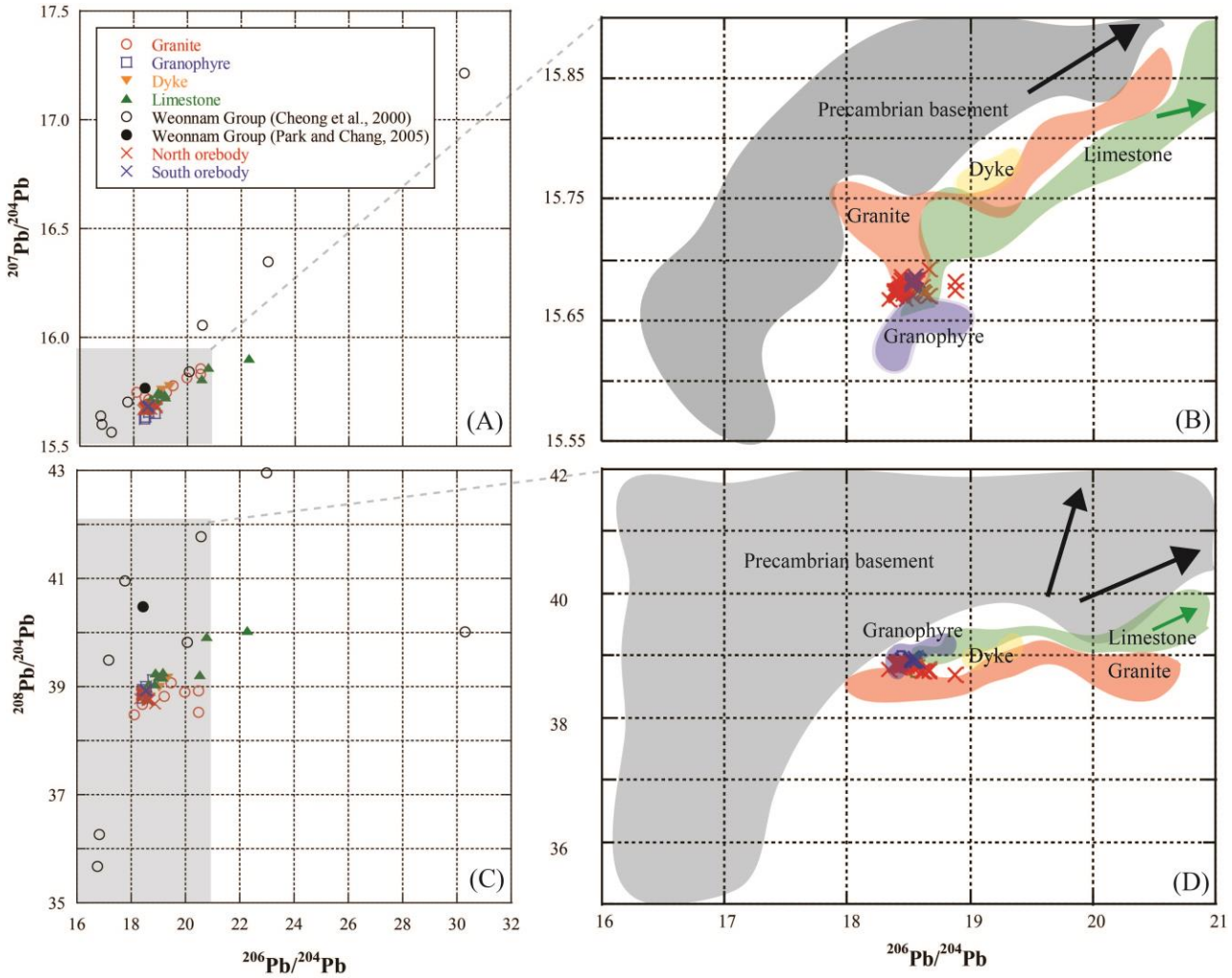

Figure 3.2. Pb isotope correlation diagrams for some country rocks near the Janggun mine. (A)–(B) $^{207}Pb/^{204}Pb$ vs. $^{206}Pb/^{204}Pb$; (C)–(D) $^{208}Pb/^{204}Pb$ vs. $^{206}Pb/^{204}Pb$. The Weonnam Group data are bulk analyses from literature (Cheong et al., 2000; Park and Chang, 2005). The gray areas in (A) and (C) are magnified in (B) and (D). In (B) and (D), the colored fields represent the country rocks. In all diagrams, all Janggun sulfides (red and blue crosses for North and South orebody, respectively) fall between the fields of the country rocks, i.e., it is possible to derive all of the sulfides by suitable mixtures of fluids having leached two or more country rocks.

Table 3.1. Lead isotopic composition of country rocks of the Janggun mine. Individual errors represent within run uncertainties at the 95% confidence level

Type of samples	# sample		$^{206}Pb/^{204}Pb$	StdErr (2σ)	$^{207}Pb/^{204}Pb$	StdErr (2σ)	$^{208}Pb/^{204}Pb$	StdErr (2σ)	$^{207}Pb/^{206}Pb$	StdErr (2σ)	$^{208}Pb/^{206}Pb$	StdErr (2σ)
Granite	1	Leachate	**18.516**	0.001	**15.688**	0.001	**38.872**	0.002	**0.84729**	0.00001	**2.09942**	0.00004
		Residue	**18.426**	0.001	**15.726**	0.001	**38.674**	0.003	**0.85346**	0.00001	**2.09888**	0.00006
		Integration	**18.514**		**15.689**		**38.868**		**0.84742**		**2.09940**	
	9	Leachate	**19.975**	0.001	**15.814**	0.001	**38.901**	0.002	**0.79172**	0.00001	**1.94749**	0.00005
		Residue	**20.487**	0.002	**15.830**	0.002	**38.924**	0.005	**0.77271**	0.00002	**1.89997**	0.00009
		Integration	**20.125**		**15.819**		**38.907**		**0.78614**		**1.93355**	
	10	Leachate	**18.555**	0.001	**15.713**	0.001	**38.900**	0.002	**0.84686**	0.00001	**2.09654**	0.00005
		Residue	**19.470**	0.001	**15.777**	0.001	**39.072**	0.002	**0.81033**	0.00001	**2.00677**	0.00007
		Integration	**18.560**		**15.713**		**38.901**		**0.84665**		**2.09602**	
	13	Leachate	**20.488**	0.001	**15.856**	0.001	**38.526**	0.002	**0.77391**	0.00001	**1.88038**	0.00006
		Residue	**18.120**	0.001	**15.746**	0.001	**38.473**	0.002	**0.86900**	0.00002	**2.12332**	0.00007
		Integration	**19.229**		**15.798**		**38.498**		**0.82445**		**2.00949**	
	18	Leachate	**18.533**	0.001	**15.695**	0.001	**38.903**	0.002	**0.84691**	0.00001	**2.09917**	0.00005
		Residue	**19.226**	0.001	**15.746**	0.001	**38.823**	0.003	**0.81903**	0.00001	**2.01932**	0.00007
		Integration	**18.560**		**15.697**		**38.900**		**0.84582**		**2.09605**	
Granophyre	16	Leachate	**18.412**	0.001	**15.626**	0.001	**38.789**	0.002	**0.84869**	0.00001	**2.10672**	0.00004
		Residue	**18.810**	0.001	**15.649**	0.001	**39.127**	0.004	**0.83195**	0.00002	**2.08010**	0.00009
		Integration	**18.416**		**15.626**		**38.792**		**0.84853**		**2.10646**	
	17	Leachate	**18.439**	0.001	**15.633**	0.001	**38.939**	0.003	**0.84785**	0.00001	**2.11180**	0.00007
		Residue	**18.555**	0.001	**15.657**	0.001	**39.003**	0.002	**0.84376**	0.00002	**2.10191**	0.00007
		Integration	**18.458**		**15.637**		**38.949**		**0.84718**		**2.11017**	
Dkye	11	Leachate	**19.043**	0.001	**15.760**	0.001	**38.985**	0.003	**0.82760**	0.00002	**2.04724**	0.00010
		Residue	**19.327**	0.001	**15.776**	0.001	**39.165**	0.003	**0.81625**	0.00001	**2.02637**	0.00006
		Integration	**19.145**		**15.766**		**39.050**		**0.82351**		**2.03971**	
Limestone/ Dolomite	2	Leachate	**19.173**	0.004	**15.725**	0.003	**39.261**	0.008	**0.82009**	0.00007	**2.04769**	0.00013
		Residue	**20.790**	0.001	**15.862**	0.001	**39.920**	0.004	**0.76299**	0.00002	**1.92013**	0.00009
		Integration	**20.314**		**15.822**		**39.726**		**0.77978**		**1.95762**	
	3-1	Residue	**18.896**	0.001	**15.741**	0.001	**39.253**	0.002	**0.83302**	0.00001	**2.07725**	0.00005
		Integration	**18.896**		**15.741**		**39.253**		**0.83302**		**2.07725**	
	3-2	Leachate 1	**18.544**	0.004	**15.664**	0.003	**38.773**	0.008	**0.84466**	0.00003	**2.09077**	0.00011
		Leachate 2	**18.908**	0.001	**15.747**	0.001	**39.255**	0.004	**0.83281**	0.00002	**2.07609**	0.00010
		Residue	**22.286**	0.003	**15.902**	0.002	**40.030**	0.006	**0.71355**	0.00003	**1.79623**	0.00009
		Integration	**18.865**		**15.729**		**39.149**		**0.83407**		**2.07587**	
	7	Residue	**19.022**	0.001	**15.739**	0.001	**39.187**	0.003	**0.82741**	0.00002	**2.06014**	0.00007
		Integration	**19.022**		**15.739**		**39.187**		**0.82741**		**2.06014**	
	14	Leachate	**18.508**	0.002	**15.679**	0.002	**38.871**	0.005	**0.84710**	0.00003	**2.10017**	0.00011
		Residue	**18.656**	0.001	**15.717**	0.001	**39.049**	0.002	**0.84245**	0.00001	**2.09311**	0.00004
		Integration	**18.654**		**15.716**		**39.046**		**0.84252**		**2.09322**	
	15	Leachate 1	**19.155**	0.001	**15.736**	0.001	**39.175**	0.003	**0.82152**	0.00002	**2.04517**	0.00007
		Leachate 2	**18.864**	0.001	**15.710**	0.001	**39.046**	0.002	**0.83279**	0.00001	**2.06979**	0.00005
		Residue	**20.531**	0.001	**15.808**	0.001	**39.217**	0.003	**0.76993**	0.00002	**1.91007**	0.00007
		Integration	**19.061**		**15.725**		**39.110**		**0.82523**		**2.05236**	

3.3.2. Trace elements

Since the major element compositions of sulfide minerals show no correlation with Pb isotope compositions, we measured trace elements of country rocks (Table 3.2) by ICP-MS to provide a better mean of recognizing different sources of the circulating fluids. This approach must be pursued with caution, as the two-stage partition of trace elements (from the country rock into the sulfide-bearing fluid, and then from the fluid into the sulfide minerals) forbid a simplified argumentation based on concentrations. However, the use of element ratios between pairs of geochemically similar elements (e.g. Co/Ni) circumvents the difficulty of estimating the composite partition coefficients.

Figure 3.3 explores the correlations between some of element ratios and the Pb isotopic compositions of granite samples. We also included the trace element ratios in the reconstituted unleached granite whole rocks, in order to find if these elements behave differently owing to their partition into more soluble and less soluble minerals. The Co/Ni ratios show a clear negative correlation and Cu/Ag and Zn/Cd ratios a good positive one, with Pb isotopic compositions (Fig. 3.3). We interpret this as a suggestion that the more radiogenic Pb signature is contained in country rocks having low Co/Ni, and high Cu/Ag and Zn/Cd, such as granite, whereas the dyke has the opposite trace element and Pb isotopic compositions signature. These same three ratios barely show any correlation with $^{208}Pb/^{204}Pb$. Figure 3.3 also shows that the reconstituted unleached whole rocks have the same general correlation trends between trace elements and Pb isotopic compositions as the leachates and residues. This indicates that, even if there are resolvable differences between the trace element signatures of leachates and residues, the inter-sample diversity is much greater than the intra-sample variability.

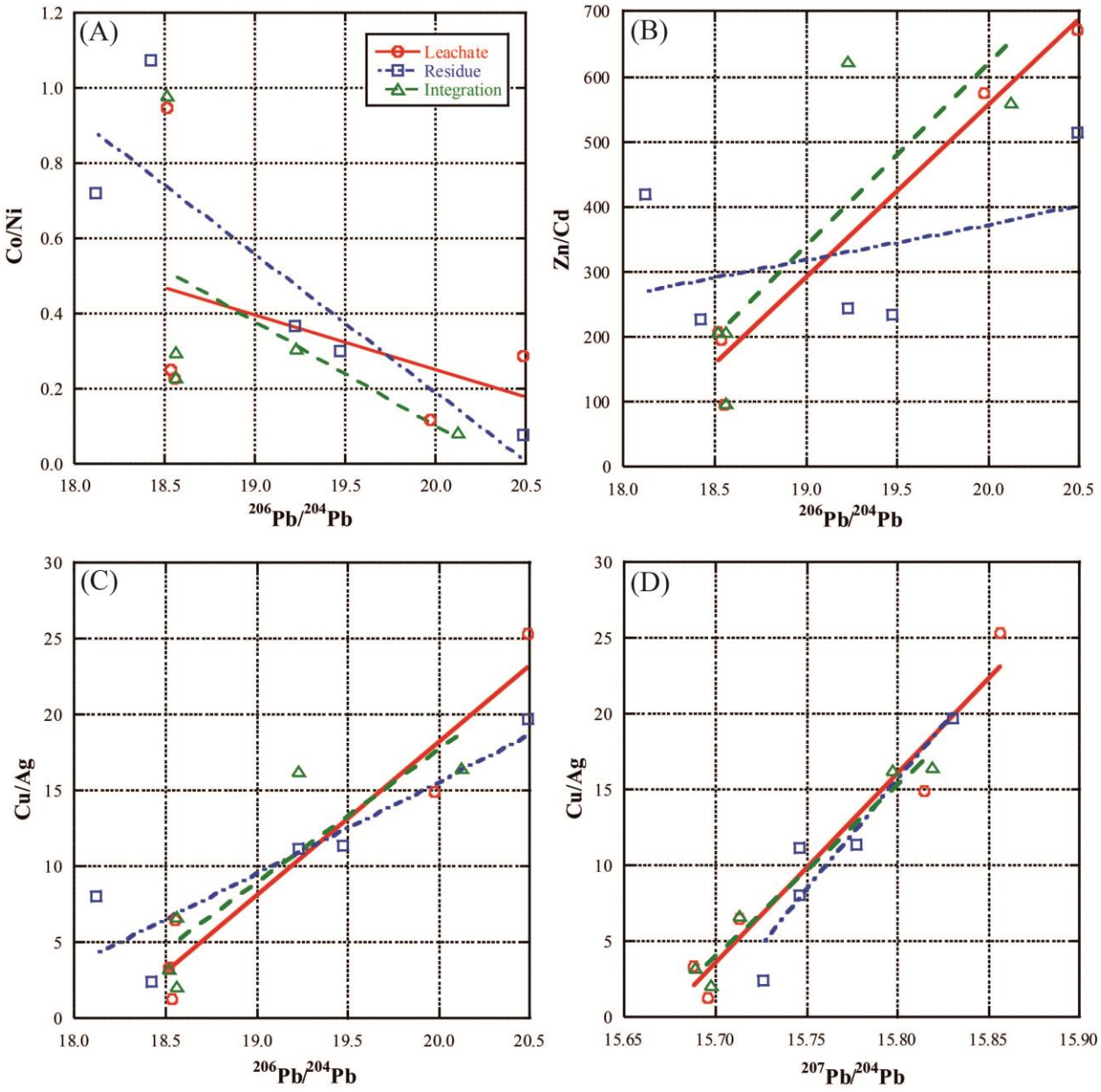

Figure 3.3. Correlations between the Pb isotopic composition and selected trace element ratios in the granite leachate-residue pairs. (A) Co/Ni vs. $^{206}Pb/^{204}Pb$; (B) Zn/Cd vs. $^{206}Pb/^{204}Pb$; (C) Cu/Ag vs. $^{206}Pb/^{204}Pb$; (D) Cu/Ag vs. $^{207}Pb/^{204}Pb$. The existence of a correlation trend suggests that a significant part of the Pb is hosted in two distinct phases, with additional phase(s) contributing smaller but well detectable amounts of Pb. The dominant carrier of radiogenic Pb (with $^{206}Pb/^{204}Pb \geq 20.5$) has a low Co/Ni ratio and high Cu/Ag and Zn/Cd ratios; the less radiogenic Pb (with $^{206}Pb/^{204}Pb \leq 18.1$) derives from a phase having the opposite trace element signature.

Table 3.2. Chemical compositions of country rock samples (Unit: nanogram for leachates and residues; microgram per gram for integrated values; abbreviation of b.d. = below detection limit)

Type of sample	Sample		55 Mn	55 Mn	59 Co	59 Co	60 Ni	60 Ni	63 Cu	63 Cu	66 Zn	66 Zn	71 Ga	71 Ga
	# sample	detection limit	<0.005	<0.006	<0.001	<0.001	<0.009	<0.015	<0.004	<0.004	<0.022	<0.071	<0.004	<0.003
Granite	1	Leachate	339557.62	347771.34	1491.49	1537.67	1711.21	1624.47	2395.03	2446.65	1325779.12	1309358.16	4475.58	6920.17
		Residue	59900.26	67896.78	584.78	659.32	544.42	613.84	335.74	263.55	27835.00	29894.88	16351.26	18597.84
		Integration	263.11	273.78	1.37	1.45	1.49	1.47	1.80	1.79	891.57	882.11	13.72	16.81
	9	Leachate	2368116.57	2457560.17	154.61	18.86	1143.99	161.78	710.43	725.54	408559.34	404477.30	3946.80	4915.57
		Residue	450862.64	467207.88	113.35	59.11	909.53	756.25	448.65	433.31	93906.39	96267.68	49622.80	54070.16
		Integration	1387.22	1439.28	0.13	0.04	1.01	0.45	0.57	0.57	247.26	246.42	26.36	29.03
	10	Leachate	740666.85	750933.55	619.91	606.03	2888.91	2671.65	2248.41	2217.71	45021.33	45084.68	2048.67	4753.89
		Residue	24812.57	26587.09	44.35	46.06	150.67	154.11	175.19	149.46	1998.20	1968.47	7029.62	7553.39
		Integration	592.73	602.05	0.51	0.50	2.35	2.19	1.88	1.83	36.41	36.43	7.03	9.53
	13	Leachate	199303.86	203456.24	356.14	360.98	1311.57	1254.77	457.48	468.83	35185.01	35247.33	554.68	783.19
		Residue	21218.95	22922.03	47.07	45.10	73.08	62.66	160.60	19.76	5245.00	5472.40	11275.92	12336.23
		Integration	223.61	229.55	0.41	0.41	1.40	1.34	0.63	0.50	41.00	41.29	12.00	13.30
	18	Leachate	309437.14	311741.87	179.16	103.89	1087.20	414.38	526.05	513.43	51095.19	50928.85	669.56	964.89
		Residue	62108.55	66710.05	103.36	98.75	295.30	268.50	378.97	356.42	20247.14	20094.31	7437.51	8071.78
		Integration	397.61	405.00	0.30	0.22	1.48	0.73	0.97	0.93	76.35	76.01	8.68	9.67
Granophyre		Leachate	134562.19	136990.08	258.90	260.16	1797.18	1884.17	992.32	938.98	32195.99	32008.43	2262.03	9642.73
	16	Residue	6405.05	6741.17	1.56	1.39	10.16	10.23	74.07	36.06	5794.76	5936.39	3168.00	3549.01
		Integration	324.64	331.01	0.60	0.60	4.16	4.36	2.46	2.25	87.49	87.39	12.51	30.38
	17	Leachate	17523.99	17117.00	155.87	156.88	805.87	795.86	2283.72	2177.44	12872.55	12827.19	1202.75	4757.65
		Residue	104417.14	108147.25	9.69	9.58	37.39	36.73	503.43	329.41	49382.32	50862.18	14255.25	16087.39
		Integration	129.40	132.93	0.18	0.18	0.89	0.88	2.96	2.66	66.06	67.59	16.40	22.12
Dyke		Leachate	321241.36	324458.19	9330.81	9382.62	392021.19	395715.82	9221.01	9075.61	49322.25	49146.42	6983.20	7295.94
	11	Residue	808938.87	836966.86	27997.83	27901.88	91388.96	89298.86	50071.61	47223.14	62853.38	59532.58	8261.39	8835.46
		Integration	590.88	607.21	19.52	19.49	252.73	253.57	31.00	29.43	58.65	56.82	7.97	8.43
Limestone/ Dolomite		Leachate 1	736.40	686.89	7.30	7.35	25.77	28.60	41.42	34.37	644.17	529.26	b.d.	b.d.
	2	Leachate 2	133717.87	145673.70	1162.48	1000.22	3840.28	2596.59	1049.04	984.00	7470.89	7443.73	931.02	1138.36
		Residue	757.00	754.38	37.32	35.50	119.96	112.13	325.93	318.57	114.39	107.73	34.50	33.31
		Integration	157.44	171.30	1.41	1.21	4.64	3.19	1.65	1.56	9.58	9.41	1.12	1.36
	3-1	Leachate 1	178.71	182.36	2.80	2.63	11.13	9.15	1.67	1.84	28.31	27.47	0.06	b.d.
		Leachate 2	390786.54	409599.12	777.37	617.61	4364.79	2848.49	2983.87	2879.21	23906.03	24527.75	64.05	181.34
		Residue	963.01	949.73	6.45	5.87	25.85	22.80	145.33	143.63	88.95	85.06	43.29	43.13
		Integration	776.70	813.96	1.56	1.24	8.72	5.71	6.20	5.99	47.61	48.83	0.21	0.44
	3-2	Leachate 1	2878.71	2862.83	19.83	18.20	39.22	34.79	2514.85	2555.45	3710.38	3539.38	b.d.	b.d.
		Leachate 2	354634.35	372200.14	616.53	380.42	3114.85	915.92	575.13	595.21	13742.39	15017.63	68.46	248.66
		Leachate 3	1985.09	2001.87	11.35	9.58	45.98	36.29	114.46	114.57	140.83	135.50	32.36	34.48
		Residue	1157.74	1208.91	8.54	8.35	20.02	16.69	52.34	37.68	380.35	339.99	784.06	857.35
		Integration	397.53	416.95	0.72	0.46	3.55	1.11	3.59	3.64	19.81	20.98	0.98	1.26
	7	Leachate 1	12823.34	12639.02	3.41	3.21	14.91	12.31	2.02	1.75	256.07	242.46	0.44	b.d.
		Leachate 2	9802280.31	10470298.14	471.69	380.94	1516.65	719.91	79.77	74.88	11291.68	11569.87	293.09	234.85
		Residue	47275.96	47413.05	331.35	331.95	53.87	49.51	2.71	3.02	90.04	83.91	39.89	39.04
		Integration	14515.88	15499.03	1.19	1.05	2.33	1.15	0.12	0.12	17.13	17.51	0.49	0.40
	14	Leachate 1	105198.11	106071.31	13.77	14.42	23.39	23.15	15.11	15.17	621.17	619.32	b.d.	b.d.
		Leachate 2	9854195.34	10295811.26	121.77	33.35	1049.50	329.72	85.52	91.73	7954.47	8584.05	229.84	213.80
		Residue	41777.35	40519.33	44.63	42.79	41.05	37.07	1.77	1.12	95.18	84.94	17.03	16.65
		Integration	13802.33	14411.26	0.25	0.12	1.54	0.54	0.14	0.15	11.97	12.82	0.34	0.32
	15	Leachate 1	14422.98	14137.73	2.76	2.26	7.53	5.60	b.d.	1.54	208.31	194.54	1.07	0.82
		Leachate 2	9338497.18	9999104.59	384.46	240.56	2064.96	820.95	201.74	190.48	5484.08	5322.23	392.58	601.05
		Leachate 3	495267.49	526858.47	2503.20	2535.62	4795.43	4737.41	377.19	367.78	2739.43	2728.77	4685.66	5126.58
		Residue	42992.13	45608.21	205.73	205.09	374.15	397.35	104.25	36.47	522.98	310.36	1266.47	1513.95
		Integration	5685.73	6084.96	1.78	1.72	4.16	3.43	0.39	0.34	5.15	4.92	3.65	4.16

Type of sample	Sample		75 As	75 As	95 Mo	95 Mo	107 Ag	107 Ag	111 Cd	111 Cd	121 Sb	121 Sb	205 Tl	208 Pb	209 Bi
	# sample	detection limit	<0.011	<0.018	<0.004	<0.007	<0.002	<0.005	<0.002	<0.003	<0.003	<0.004	<0.011	<0.003	<0.001
Granite	1	Leachate	1581.01	1546.00	65.24	71.19	699.42	735.45	6385.50	6557.72	5552.06	5653.62	384.37	440756.0	673.23
		Residue	2421.25	2936.17	10.83	7.45	134.79	137.76	122.21	141.16	1144.88	1299.71	1419.20	9263.45	38.95
		Integration	2.64	2.95	0.05	0.05	0.55	0.58	4.29	4.41	4.41	4.58	1.19	296.41	0.47
	9	Leachate	1482.79	894.50	30.26	b.d.	47.69	51.20	712.35	754.92	4154.92	4193.77	1063.02	1806.47	108.97
		Residue	37598.02	39796.07	14.95	4.78	22.70	13.92	182.99	180.95	2065.11	2193.72	7412.41	749.95	40.09
		Integration	19.23	20.02	0.02	0.00	0.03	0.03	0.44	0.46	3.06	3.14	4.17	1.26	0.07
	10	Leachate	5748.53	5677.96	560.98	553.18	344.13	363.08	469.32	463.60	1342.02	1363.90	191.20	73244.08	660.40
		Residue	12930.56	14504.26	27.39	23.26	15.41	8.21	8.48	3.62	1606.29	1747.28	455.04	423.73	7.30
		Integration	14.46	15.63	0.46	0.45	0.28	0.29	0.37	0.36	2.28	2.41	0.50	57.04	0.52
	13	Leachate	2998.51	2969.88	25.02	20.88	18.03	23.22	52.38	48.10	718.99	739.32	b.d.	13615.18	842.36
		Residue	541.47	497.90	14.82	10.48	19.97	9.92	12.53	9.24	135.06	150.73	806.12	15443.16	19.25
		Integration	3.59	3.52	0.04	0.03	0.04	0.03	0.07	0.06	0.87	0.90	0.82	29.47	0.87
	18	Leachate	4791.52	4657.50	b.d.	b.d.	397.48	409.23	260.85	262.18	6972.65	7068.42	65.67	127501.7	355.70
		Residue	4005.56	4377.09	70.68	50.14	33.86	24.18	83.27	86.22	1541.66	1703.79	954.31	5185.77	41.27
		Integration	9.41	9.67	0.08	0.05	0.46	0.46	0.37	0.37	9.11	9.39	1.09	142.00	0.42
Granophyre	16	Leachate	1154.95	3128.36	270.13	273.92	70.21	76.50	110.04	113.40	10.63	6.54	47.89	45890.79	279.31
		Residue	83.01	99.99	21.70	19.22	92.04	18.60	41.16	12.76	10.06	10.91	133.59	446.25	3.90
		Integration	2.85	7.43	0.67	0.68	0.37	0.22	0.35	0.29	0.05	0.04	0.42	106.71	0.65
	17	Leachate	563.14	1373.55	340.21	322.82	25.37	25.24	38.52	39.33	85.29	85.50	b.d.	20917.10	169.69
		Residue	3662.26	4177.32	21.59	15.13	111.17	78.31	48.40	31.07	73.92	78.42	713.16	4122.51	12.57
		Integration	4.48	5.89	0.38	0.36	0.14	0.11	0.09	0.07	0.17	0.17	0.76	26.57	0.19
Dyke	11	Leachate	1091.42	246.55	b.d.	b.d.	80.86	81.46	149.17	168.97	6690.33	6778.98	745.08	8558.33	465.47
		Residue	13618.26	14582.02	460.65	451.59	81.48	83.72	52.07	53.56	13442.61	13900.52	1931.27	4827.44	176.68
		Integration	7.69	7.75	0.24	0.24	0.08	0.09	0.11	0.12	10.53	10.81	1.40	7.00	0.34
Limestone/ Dolomite	2	Leachate 1	10163.98	9836.16	b.d.	b.d.	53.31	50.30	b.d.	b.d.	204.24	160.74	b.d.	215.44	b.d.
		Leachate 2	4066.20	3468.46	67.55	18.03	5.54	6.45	10.34	11.85	597.24	630.34	24.55	517.51	9.90
		Residue	16.24	13.20	40.97	39.98	0.28	0.22	0.18	0.13	3.82	3.84	1.16	4.32	0.36
		Integration	16.59	15.51	0.13	0.07	0.07	0.07	0.01	0.01	0.94	0.93	0.03	0.86	0.01
	3-1	Leachate 1	b.d.	1.42	1.08	1.14	b.d.	b.d.	b.d.	0.03	11.60	10.98	b.d.	0.26	b.d.
		Leachate 2	2602.43	2528.55	232.42	233.48	4.05	4.10	66.31	66.73	3384.83	3705.17	b.d.	985.15	40.07
		Residue	8.55	6.53	48.26	47.45	0.15	0.13	0.28	0.24	17.41	16.91	16.06	3.99	0.21
		Integration	5.17	5.03	0.56	0.56	0.01	0.01	0.13	0.13	6.77	7.40	0.03	1.96	0.08
	3-2	Leachate 1	3368.13	2994.74	b.d.	b.d.	21.27	19.02	b.d.	b.d.	64.21	58.12	b.d.	273.79	b.d.
		Leachate 2	4935.42	4655.69	24.02	20.79	3.83	6.41	17.90	20.63	959.94	1119.54	b.d.	839.38	7.37
		Leachate 3	27.49	25.56	10.72	10.49	0.18	0.15	0.17	0.19	2.50	2.36	11.18	8.47	0.18
		Residue	113.91	99.68	6.45	b.d.	8.82	6.41	b.d.	b.d.	90.31	101.35	88.19	15.26	b.d.
		Integration	9.31	8.57	0.05	0.03	0.04	0.04	0.02	0.02	1.23	1.41	0.11	1.25	0.01
	7	Leachate 1	b.d.	b.d.	b.d.	1.19	b.d.	b.d.	b.d.	b.d.	3.10	2.86	b.d.	1.92	b.d.
		Leachate 2	3007.10	2737.62	147.04	54.34	26.57	27.72	4.29	4.04	651.55	719.10	61.73	640.83	3.97
		Residue	185.92	186.85	32.04	29.40	0.44	0.41	b.d.	0.18	2.41	2.47	18.61	7.29	0.25
		Integration	4.70	4.30	0.26	0.13	0.04	0.04	0.01	0.01	0.97	1.07	0.12	0.96	0.01
	14	Leachate 1	447.77	318.59	b.d.	b.d.	b.d.	b.d.	b.d.	b.d.	b.d.	b.d.	b.d.	24.77	b.d.
		Leachate 2	1203.95	928.20	100.62	15.97	14.58	14.18	6.14	6.50	244.68	279.77	b.d.	1568.73	1.33
		Residue	35.97	34.33	15.99	15.76	b.d.	0.28	b.d.	0.14	1.64	1.39	7.48	11.95	0.30
		Integration	2.33	1.77	0.16	0.04	0.02	0.02	0.01	0.01	0.34	0.39	0.01	2.22	b.d.
	15	Leachate 1	b.d.	7.28	2.55	3.41	b.d.	b.d.	b.d.	b.d.	13.08	12.54	8.96	1.98	b.d.
		Leachate 2	9141.71	9138.16	146.97	52.90	194.29	191.78	5.67	3.66	3303.47	3579.73	690.04	1708.02	9.36
		Leachate 3	17300.07	19173.08	1196.95	1215.10	693.42	684.94	4.50	2.66	122.16	130.05	2236.98	1993.93	15.23
		Residue	1572.11	1795.10	184.09	181.65	85.45	72.40	7.51	b.d.	3799.89	4118.53	543.73	158.00	b.d.
		Integration	16.10	17.31	0.88	0.84	0.56	0.55	0.01	0.00	4.16	4.51	2.00	2.22	0.01

3.4. Conclusions

1. Leaching of country rocks by circulating fluids is able to produce the observed Pb isotopic compositions and trace element patterns in the sulfide minerals, whereby different end-members identified by the Pb isotope correlation diagrams can be linked to different country rocks.
2. The changing, alternating contribution of all proximal and distal country rocks in the sulfide minerals requires a time-variability of the pathways along which the circulating fluids interacted with the basement.
3. Thus, the heterogeneous Pb isotopic compositions, sulfur isotope composition, and trace element patterns of our sulfides are primary and occurred due to successive pulses of chemically and isotopically distinct mineralizing fluids.

References

1. Ahn, K.S., Lee, H.K. (1995). Petrological and geochemical studies on guartzite from the Jangsan Quartzite Formation in the Bong-hwa-Gun, Korea. Econ. Environ. Geol., 28, 43–51.

2. Ahrens, L. H. (1955). Implications of the Rhodesia age pattern. Geochimica et Cosmochimica Acta, 8(1–2), 1–15.

3. Allègre, C. J. (1967). Methode de discussion geochronologique concordia generalisee: Applicationàla discussion desaˆges Uranìum-Thorium-Plomb discordants. Earth and Planetary Science Letters, 2(1), 57–66.

4. Arfè, G., Mondillo, N., Boni, M., Balassone, G., Joachimski, M., Mormone, A., & Di Palma, T. (2017). The karst-Hosted Mina grande nonsulfide zinc deposit, Bongará district (Amazonas region, Peru). Economic Geology, 112(5), 1089–1110.

5. Aston, F. W. (1927). Atoms and their Packing Fractions. Nature, 120(3035), 956.

6. Bachinski, D. J. (1969). Bond strength and sulfur isotopic fractionation in coexisting sulfides. Economic Geology, 64(1), 56–65.

7. Barton, P.B.Jr., Bethke, P.M. (1987). Chalcopyrite disease in sphalerite: pathology and epidemiology. Am. Mineral., 72(5–6), 451–467.

8. Basuki, N. I., Taylor, B. E., & Spooner, E. T. C. (2008). Sulfur isotope evidence for thermochemical reduction of dissolved sulfate in Mississippi Valley-type zinc-lead mineralization, Bongara area, northern Peru. Economic Geology, 103(4), 783–799.

9. Bekker, A., Holland, H. D., Wang, P. L., Rumble III, D., Stein, H. J., Hannah, J. L., ... & Beukes, N. J. (2004). Dating the rise of atmospheric oxygen. Nature 427: 117–120

10. Bell, K., Zaitsev, A.N., Spratt, J., Fröjdö, S., Rukhlov, A.S. (2015). Elemental, lead and sulfur isotopic compositions of galena from Kola carbonatites, Russia – implications for melt and mantle evolution. Mineralogical Magazine, 79, 219–241.

11. Belshaw, N. S., Freedman, P. A., O'nions, R. K., Frank, M., & Guo, Y. (1998). A new variable dispersio n double-focusing plasma mass spectrometer with performance illustrated for Pb isotopes. International Journal of Mass Spectrometry, 181(1–3), 51–58.

12. Berglund, M., & Wieser, M. E. (2011). Isotopic compositions of the elements 2009 (IUPAC Technical Report). Pure and applied chemistry, 83(2), 397–410.

13. Berner, R. A. (1985). Sulphate reduction, organic matter decomposition and pyrite formation. Philosophical Transactions of the Royal Society of London. Series A, Mathematical and Physical Sciences, 315(1531), 25–38.

14. Bortnikov, N.S., Genkin, A.D., Dobrovol'Skaya, M.G., Muravitskaya, G.N., Filimonova, A.A. (1991). The nature of chalcopyrite inclusions in sphalerite; exsolution, coprecipitation, or" disease"?. Econ. Geol., 86(5), 1070–1082.

15. Brophy, J. A. (2012). NI 43-101 Technical Report Rio Cristal Resources Corp. Bongará Zinc Project, 104.

16. Bulle, F., Rubatto, D., Ruggieri, G., Luisier, C., Villa, I.M., Baumgartner, L. (2020). Episodic hydrothermal alteration recorded by microscale oxygen isotope analysis of white mica in the Larderello-Travale Geothermal Field, Italy. Chem. Geol., 532, 119288.

17. Burnham, C. W., & Ohmoto, H. (1980). Late stage processes of felsic magmatism: Society of Mining Geologists Japan Special Issue 8.

18. Canfield, D. E. (2001). Biogeochemistry of sulfur isotopes. Reviews in mineralogy and geochemistry, 43(1), 607–636.

19. Canfield, D. E. (2004). The evolution of the Earth surface sulfur reservoir. American Journal of Science, 304(10), 839–861.

20. Canfield, D. E., & Teske, A. (1996). Late Proterozoic rise in atmospheric oxygen concentration inferred from phylogenetic and sulphur-isotope studies. Nature, 382(6587), 127.

21. Carrasco, J. J. (2006). Distal alteration in the carbonate-hosted replacement and skarn systems at Yauricocha, central Peru (Doctoral dissertation, University of British Columbia).

22. Cattell, A., Krogh, T. E., & Arndt, N. T. (1984). Conflicting Sm-Nd whole rock and U-Pb zircon ages for Archean lavas from Newton Township, Abitibi belt, Ontario. Earth and Planetary Science Letters, 70(2), 280–290.

23. Chambers, L. A. (1982). Sulfur isotope study of a modern intertidal environment, and the interpretation of ancient sulfides. Geochimica et Cosmochimica Acta, 46(5), 721–728.

24. Chambers, L. A., & Trudinger, P. A. (1979). Microbiological fractionation of stable sulfur isotopes: a review and critique. Geomicrobiology Journal, 1(3), 249–293.

25. Chang K.H. (1997) Korean peninsula. In: Encyclopedia of European and Asian Regional Geology. Encyclopedia of Earth Science. Springer, Dordrecht.

26. Chang, B. U., Chang, H. W., & Cheong, C. S. (1995a). Lead isotope study on lead-zinc ore deposits in the eastern and southern parts of the Gyeongsang basin. Economic and Environmental Geology, 28(1), 19–24.

27. Chang, H. W., Cheong, C. S., Park, H. I., & Chang, B. U. (1995b). Lead isotopic study on the Dongnam Fe-Mo skarn deposit. Economic and Environmental Geology, 28(1), 25–31.

28. Chang, H. W., Lee, M. S., Park, H. I., Kim, J. H., & Chi, J. M. (1990). Study of the Taebaeksan mineralized Area. Kosef 87-0609 report, 173–264.

29. Chang, K. H. (1985). Treatise on geology of Korea. Seoul: Minumsa, 270.

30. Chaussidon, M., Albarede, F., & Sheppard, S. M. F. (1987). Sulphur isotope heterogeneity in the mantle from ion microprobe measurements of sulphide inclusions in diamonds. Nature, 330(6145), 242.

31. Cheong, C.H. (1969) Stratigraphy and paleontology of the Samchang coalfield, Gangweondo, Korea. The Journal of the Geological Society of Korea, 26, 471–487.

32. Cheong, C.S., Kwon, S.T., Park, K.H. (2000). Pb and Nd isotopic constraints on Paleoproterozoic crustal evolution of the northeastern Yeongnam massif, South Korea. Precambrian Res., 102(3–4), 207–220.

33. Choi, S. G., Choi, B. K., Ahn, Y. H., & Kim, T. H. (2009). Re-evaluation of genetic environments of zinc-lead deposits to predict hidden skarn orebody. Economic and environmental geology, 42(4), 301–314.

34. Choi, S.-G., Ryu, I.-C., Pak, S.J., Wee, S.M., Kim, C.S. and Park, M.E. (2005) Cretaceous epithermal gold-silver mineralization and geodynamic environment, Korea. Ore Geol. Review, v. 26, p. 115–135.

35. Chough, S. K., & Sohn, Y. K. (2010). Tectonic and sedimentary evolution of a Cretaceous continental arc–backarc system in the Korean peninsula: new view. Earth-Science Reviews, 101(3–4), 225–249.

36. Chough, S. K., Kwon, S. T., Ree, J. H., & Choi, D. K. (2000). Tectonic and sedimentary evolution of the Korean peninsula: a review and new view. Earth-Science Reviews, 52(1–3), 175–235.

37. Chun, S. S., & Chough, S. K. (1992). Depositional sequences from high-concentration turbidity currents, Cretaceous Uhangri Formation (SW Korea). Sedimentary geology, 77(3–4), 225–233.

38. Chung, J. I., & Park, K. H. (2006). Pb isotopic composition of the ore deposits distributed in Jeonbuk Province. The Journal of the Petrological Society of Korea, 15(2), 81–89.

39. Claypool, G. E., Holser, W. T., Kaplan, I. R., Sakai, H., & Zak, I. (1980). The age curves of sulfur and oxygen isotopes in marine sulfate and their mutual interpretation. Chemical Geology, 28, 199–260.

40. Clayton, D. D., & Ramadurai, S. (1977). On presolar meteoritic sulphides. Nature, 265(5593), 427.

41. Cluzel, D., Cadet, J.P. and Lapierre, H. (1990) Geodynamics of the Ogcheon Belt (South Korea), in Geodynamic Evolution of the Eastern Eurasian Margin (ed. J. Angelier). Tectonophysics, 183, 41–56. 6.

42. Cluzel, D., Jolivet, L. and Cadet, J.P. (1991a) Early Middle Palaeozoic intraplate orogeny in the Ogcheon belt (South Korea). Tectonics, 10, 1130–51.

43. Cluzel, D., Lee, B.J. and Cadet, J.P. (1991b) Indosinian ductile dextral fault system and synkinematic plutonism in the south-west Ogcheon belt (South Korea). Tectonophysics, 194, 131–51.

44. Cook, N.J., Ciobanu, C.L., Pring, A., Skinner, W., Shimizu, M., Danyushevsky, L., Saini-Eidukat, B., Melcher, F. (2009). Trace and minor elements in sphalerite: A LA-ICPMS study. Geochim. Cosmochim. Acta, 73(16), 4761–4791.

45. Doe, B. R., & Delevaux, M. H. (1972). Source of lead in southeast Missouri galena ores. Economic Geology, 67(4), 409–425.

46. Doe, B. R., & Stacey, J. S. (1974). The application of lead isotopes to the problems of ore genesis and ore prospect evaluation: a review. Economic Geology, 69(6), 757–776.

47. Einaudi, M. T., Meinert, L. D., & Newberry, R. J. (1981). Skarn deposits: Econ. Geol., 75th Anniversary, 317–391.

48. Eldridge, C. S., Compston, W., Williams, I. S., Harris, J. W., & Bristow, J. W. (1991). Isotope evidence for the involvement of recycled sediments in diamond formation. Nature, 353(6345), 649.

49. Eldridge, C.S., Bourcier, W.L., Ohmoto, H., Barnes, H.L. (1988). Hydrothermal inoculation and incubation of the chalcopyrite disease in sphalerite. Econ. Geol., 83(5), 978–989.

50. Encyclopaedia Britannica, n.d. Available online: https://www.britannica.com/science

51. Energymining, n.d. Available online: http://www.energymining.sa.gov.au/minerals/invest/mineral_commodities/lead_-_zinc

52. Esteban-Arispe, I., Velasco, F., Boyce, A.J., Morales-Ruano, S., Yusta, I., Carrillo-Rosúa, J. (2016). Unconventional non-magmatic sulfur source for the Mazarrón Zn–Pb–Cu–Ag–Fe epithermal deposit (SE Spain). Ore Geology Reviews, 72, 1102–1115.

53. Farina, F., Dini, A., Davies, J. H., Ovtcharova, M., Greber, N. D., Bouvier, A. S., ... & Schaltegger, U. (2018). Zircon petrochronology reveals the timescale and mechanism of anatectic magma formation. Earth and planetary science letters, 495, 213–223.

54. Farquhar, J., & Wing, B. A. (2003). Multiple sulfur isotopes and the evolution of the atmosphere. Earth and Planetary Science Letters, 213(1-2), 1–13.

55. Farquhar, J., Bao, H., & Thiemens, M. (2000a). Atmospheric influence of Earth's earliest sulfur cycle. Science, 289(5480), 756–758.

56. Farquhar, J., Savarino, J., Jackson, T. L., & Thiemens, M. H. (2000b). Evidence of atmospheric sulphur in the martian regolith from sulphur isotopes in meteorites. Nature, 404(6773), 50.

57. Faure, G. (1977). Principles of isotope geology.

58. Franklin, J. M., Eckstrand, O. R., Sinclair, W. D., & Thorpe, R. I. (1996). Volcanic-associated massive sulphide base metals. Geology of Canadian mineral deposit types: Geological Survey of Canada, Geology of Canada Series, 8, 158–183.

59. Franklin, J. M., Gibson, H. L., Jonasson, I. R., & Galley, A. G. (2005). Volcanogenic massive sulfide deposits. Economic Geology, 100(Anniversary volume), 523–560.

60. Galley, A. G., Hannington, M. D., & Jonasson, I. R. (2007). Volcanogenic massive sulphide deposits. Mineral deposits of Canada: A synthesis of major deposit-types, district metallogeny, the evolution of geological provinces, and exploration methods: Geological Association of Canada, Mineral Deposits Division, Special Publication, 5, 141–161.

61. Gaudette, H.E. and Hurley, P.M. (1973) U-Pb zircon age of Precambrian basement gneiss of South Korea. Geol. Soc. Am. Bull., 84, 2305–6

62. Gerling, E. K. (1942). Age of the Earth according to radioactivity data. In Doklady (Proc Russian Acad Sci) (Vol. 34, pp. 259–261).

63. Goldhaber, M. B., & Kaplan, I. R. (1975). Controls and consequences of sulfate reduction rates in recent marine sediments. Soil Science, 119(1), 42–55.

64. Heald, P., Foley, N. K., & Hayba, D. O. (1987). Comparative anatomy of volcanic-hosted epithermal deposits; acid-sulfate and adularia-sericite types. Economic geology, 82(1), 1–26.

65. Hedenquist, J. W., Arribas, A., & Reynolds, T. J. (1998). Evolution of an intrusion-centered hydrothermal system; Far Southeast-Lepanto porphyry and epithermal Cu-Au deposits, Philippines. Economic Geology, 93(4), 373–404.

66. Hirata, T. (1996). Lead isotopic analyses of NIST standard reference materials using multiple collector inductively coupled plasma mass spectrometry coupled with a modified external correction method for mass discrimination effect. Analyst, 121(10), 1407–1411.

67. Hirata, T., & Nesbitt, R. W. (1995). U-Pb isotope geochronology of zircon: Evaluation of the laser probe-inductively coupled plasma mass spectrometry technique. Geochimica et cosmochimica Acta, 59(12), 2491–2500.

68. Holden, N. E., & Walker, F. W. (1972). Chart of the Nuclides. (11th ed.) Educational Relations, General Electric Co., Schenectady, N. Y.

69. Holland, H. D. (1965). Some applications of thermochemical data to problems of ore deposits;[Part] 2, Mineral assemblages and the composition of ore forming fluids. Economic Geology, 60(6), 1101–1166.

70. Holmes, A. (1946). An estimate of the age of the Earth. 680–684.

71. Holser, W. T., Kaplan, I. R., Sakai, H., & Zak, I. (1979). Isotope geochemistry of oxygen in the sedimentary sulfate cycle. Chemical Geology, 25(1–2), 1–17.

72. Hong, Y.K. (1992) Petrogenesis and evolution of Early Proterozoic granitic rocks in the northeastern Ryeongnam Massif, Korea. J. Geol. Soc. Korea, 28(6), 571–89.

73. Horwitz, E. P., Chiarizia, R., & Dietz, M. L. (1992). A novel strontium-selective extraction chromatographic resin. Solvent extraction and ion exchange, 10(2), 313–336.

74. Horwitz, E. P., Dietz, M. L., Rhoads, S., Felinto, C., Gale, N. H., & Houghton, J. (1994). A lead-selective extraction chromatographic resin and its application to the isolation of lead from geological samples. Analytica Chimica Acta, 292(3), 263–273.

75. Houtermans, F. G. (1953). Determination of the age of the earth from the isotopic composition of meteoritic lead. Il Nuovo Cimento (1943-1954), 10(12), 1623–1633.

76. Houtermans, F. G. (1946). The isotope abundances in natural lead and the age of uranium. Natural Sciences, 33 (6), 185–186.

77. Hulston, J. R., & Thode, H. G. (1965). Variations in the S^{33}, S^{34}, and S^{36} contents of meteorites and their relation to chemical and nuclear effects. Journal of Geophysical Research, 70(14), 3475–3484.

78. Hurley, P., Fairbairn, H.W., Pinson, W.H. Jr. and Lee, J.H. (1973) Middle Precambrian and older apparent age values in basement gneisses of South Korea, and relations with Southwest Japan. Geol. Soc. Am. Bull., 84, 2299–2304.

79. Huston, D. (1999). Stable isotopes and their significance for understanding the genesis of volcanic-associated massive sulfide deposits: a review. Volcanic-associated massive sulfide deposits: processes and examples in modern and ancient settings, 157–179.

80. Hutchinson, M. N., & Scott, S. D. (1981). Sphalerite geobarometry in the Cu-Fe-Zn-S system. Econ. Geol, 76(143), 53.

81. Hwang, D. H., & Reedman, A. J. (1975). A report on Samhan Janggun mine. Geol Inst Korea, Rep Geol Mineral Expl, 3, 187–216.

82. Imai, N., & Lee, H. K. (1980). Complex sulfide-sulfosalt ores from Janggun mine, ROK. Complex Sulfide Ores, 248–249.

83. Imai, N., Lee, H. K., & Machida, M. (1980). Vanadium-bearing green mica from the Jangsan Quartzite in the Janggun mine area, Republic of Korea. Clay Science, 5(5), 221–236.

84. Janecky, D. R., & Shanks, W. C. (1988). Computational modeling of chemical and sulfur isotopic reaction processes in sea-floor hydrothermal systems; chimneys, massive sulfide, and subjacent alteration zones. The Canadian Mineralogist, 26(3), 805–825.

85. Jeong, Y. J., Cheong, C. S., Shin, D., Lee, K. S., Jo, H. J., Gautam, M. K., & Lee, I. (2012). Regional variations in the lead isotopic composition of galena from southern Korea with implications for the discrimination of lead provenance. Journal of Asian Earth Sciences, 61, 116–127.

86. Johan, Z. (1988). Indium and germanium in the structure of sphalerite: an example of coupled substitution with copper. Miner. Petrol., 39(3-4), 211–229.

87. Jørgensen, B. B., Isaksen, M. F., & Jannasch, H. W. (1992). Bacterial sulfate reduction above 100 C in deep-sea hydrothermal vent sediments. Science, 258(5089), 1756–1757.

88. Kanasewich, E. R. (1962). Approximate age of tectonic activity using anomalous lead isotopes. Geophysical Journal of the Royal Astronomical Society, 7(2), 158–168.

89. Kang, J., Wille, M., Hofmann, B. A., Strauss, H., & Villa, I. M. (2020). Heterogeneous lead isotopic compositions of sulfide minerals from a hydrothermal replacement deposit (Janggun mine, South Korea). *Ore Geology Reviews*, *122*, 103527.

90. Kaplan, I. R., & Hulston, J. R. (1966). The isotopic abundance and content of sulfur in meteorites. Geochimica et Cosmochimica Acta, 30(5), 479–496.

91. Keith, M., Haase, K.M., Schwarz-Schampera, U., Klemd, R., Petersen, S. and Bach, W. (2014). Effects of temperature, sulfur, and oxygen fugacity on the composition of sphalerite from submarine hydrothermal vents. Geology, 42(8), 699–702.

92. Kesler, S. E. (1996). Appalachian Mississippi Valley-type deposits: Paleoaquifers and brine provinces. Soc Econ Geol Spec Pub, 4, 29–57.

93. Kim, J. H. (1994). Structure in the Taebaeksan zone. Structure and Metamorphism of the Ogcheon Belt: Field Trip Guidebook.

94. Kim, J. H. (1996). Mesozoic tectonics in Korea. Journal of Southeast Asian Earth Sciences, 13(3-5), 251–265.

95. Kim, J.H. (1987) Caledonian Ogcheon Orogeny of Korea with special reference to the Ogcheon uraniferous marine black slate. Unpubl. PhD. Thesis, University of Tokyo, 208

96. Kim, J.H., Kee, W.-S. (1991). Tectonic significance of the Soon-chang Shear Zone, the Hwasun Coalfield, Korea. J. Geol. Soc.Korea 27, 642–655 (in Korean with English abstract).

97. Kim, J.H., Lee, J.Y., Nam, K.H. (1994). PreJurassic thrust movement in Danyang area, Danyang coalfield, Korea. J. Geol. Soc. Korea 30, 35–40 in Korean with English abstract.

98. Kim, J.N., Ree, J.H., Kwon, S.T., Park, Y., Choi, S.J., Cheong, C.S. (2000). The Kyonggi shear zone of the central Korean peninsula: late orogenic imprint of the North and South China collision. J. Geol. 108, 469–478.

99. Kim, K. H., & Nakai, N. (1980). Sulfur isotope composition and isotopic temperatures of some base metal ore deposits (Korea R.). Journal of the Geological Society of Korea [R.](Korea R.).

100. Kim, K.H. (1986). Origin of manganese carbonates in the Janggun mine, South Korea. Econ. Environ. Geol., 19, 109–123.

101. Kim, O. J. (1971). Study on the intrusion epochs of younger granites and their bearing to orogenies in South Korea. Economic and Environmental Geology, 4(1), 1–9.

102. Kim, S. J. (1970). Mineralogy and genesis of the manganese ores from Janggun Mine, Korea. J. Geol. Soc. Korea, 6(3), 135–186.

103. Kim, S. J. (1979). The Stratabound manganese carbonate deposits of the-Janggun mine area, Korea. Monograph Series on Mineral Deposits, Schweizerbart Science publishers, Germany.

104. Kiyosu, Y. (1980). Chemical reduction and sulfur-isotope effects of sulfate by organic matter under hydrothermal conditions. Chemical Geology, 30(1–2), 47-56.

105. Kobayashi, T. (1966) Stratigraphy of the Chosen group in Korea and South Manchuria and its relations to the Cambro-Ordovician faunas of other areas. J. Faculty Sci. Univ. Tokyo, Sect. 2, 2, 209–311.

106. Kramers, J. D., & Tolstikhin, I. N. (1997). Two terrestrial lead isotope paradoxes, forward transport modelling, core formation and the history of the continental crust. Chemical Geology, 139(1–4), 75–110.

107. Krouse, H. R., & Coplen, T. B. (1997). Reporting of relative sulfur isotope-ratio data (technical report). Pure and Applied Chemistry, 69(2), 293–296.

108. Krumrei, T. V., Villa, I. M., Marks, M. A., & Markl, G. (2006). A 40Ar/39Ar and U/Pb isotopic study of the Ilímaussaq complex, South Greenland: implications for the 40K decay constant and for the duration of magmatic activity in a peralkaline complex. Chemical Geology, 227(3-4), 258–273.

109. Kwon, S.T., Lan, C.Y. (1991) Sm-Nd isotopic study of the Ogcheon amphibolite, Korea: preliminary report. J. Korean Inst. Mining Geol., 24(3), 277–85.

110. Kwon, S.T., Ree, J.H. (1997). A note on the age of the Honam Shear Zone. J. Geol. Soc. Korea 33, 183–188.

111. Kwon, S.T., Ree, J.H., Park, K.H., Jeon, E.Y. (1995). Nature of contact between the Ogcheon belt and Yeongnam massif and the Pb–Pb age of granitic gneiss in Cheondong-ri, Danyang. J.Petrol. Soc. Korea 4, 144–152.

112. Leach, D. L., Bradley, D. C., Huston, D., Pisarevsky, S. A., Taylor, R. D., & Gardoll, S. J. (2010a). Sediment-hosted lead-zinc deposits in Earth history. Economic Geology, 105(3), 593-625.

113. Leach, D. L., Taylor, R. D., Fey, D. L., Diehl, S. F., & Saltus, R. W. (2010b). A deposit model for Mississippi Valley-type lead-zinc ores. Chapter A of mineral deposit models for resource assessment: USGS, Scientific Investigations Report.

114. Lee, C. H., Lee, H. K., & Kim, S. J. (1998a). Geochemistry and mineralization age of magnesian skarn-type iron deposits of the Janggun mine, Republic of Korea. Mineralium Deposita, 33(4), 379-390.

115. Lee, C. H., Song, S., & Lee, H. K. (1996a). Mg-skarn minerals from magnetite deposits of the Janggun mine, Korea. Economic and Environmental Geology, 29(1), 11–21.

116. Lee, C.H. (1987a). Stratigraphy and depositional environments in the Ogcheon Supergroup with the special consideration on the carbonate key beds. Sci. Rep. Inst. Geosci., Univ. Tsukuba, Sec. B 8, 1–50.

117. Lee, D.S. (ed.) (1987b). Geology of Korea, Seoul, Republic of Korea: Kyohak Sa Publ. Co., 514.

118. Lee, H. K. (2015). Report: Study for characteristic lead-zinc mineralization (Yenhwa, Uljin and Janggun mine) from south-east part of Taebaegsan mineral region in Korea.

119. Lee, H. K., Ko, S. J., & Naoya, I. (1990). Genesis of the Lead-Zinc-Silver and Iron Deposits of the Janggun Mine, as Related to Their Structural Features Structural Control and Wall Rock Alteration of Ore-Formation. Economic and Environmental Geology, 23(2), 161–181.

120. Lee, H. K., Lee, C. H., & Song, S. (1996b). Ore minerals and depositional conditions of magnetite deposits from the Janggun mine, Korea. Econ Environ Geol, 29, 1–9.

121. Lee, H.K., Moon, H.S., Oh, M.S. (2007). In: Economic Mineral Deposits in Korea. ACANET, Seoul, 762.

122. Lee, K. S., & Chang, H. W. (1996). Sm-Nd isotopic and geochemical studies of the Ogcheon amphibolites from the Munkyeong-Gaeun area, Korea. J. Geol. Soc. Korea, 32(2), 172–186.

123. Lee, M.S, (1985). Sulfur and carbon isotope studies of principal metallic deposits in the metallogenic province of the Taebaeg Mt. region, Korea. J. Korea Inst. Mining Geol., 18, 247–251.

124. Lee, M.W. (1982). Petrology and geochemistry of Jeju Volcanic Island, Korea. Tohoku Univ. Sci. Rep., Ser. 3 15, 177–256.

125. Lee, S.K., Song, Y.S., Masuda, A. and Shimizu, H. (1992) La-Ce and Nd-Sm systems and REE pattern of primordial Korea. J. Geol. Soc. Korea, 28(5), 513.

126. Leggett, J. K. (1980). British Lower Palaeozoic black shales and their palaeo-oceanographic significance. Journal of the Geological Society, 137(2), 139–156.

127. Longerich, H. P., Fryer, B. J., & Strong, D. F. (1987). Trace analysis of natural alloys by inductively coupled plasma-mass spectrometry (ICP-MS): application to archeological native silverartifacts. Spectrochimica Acta Part B: Atomic Spectroscopy, 42(1–2), 101–109.

128. Longerich, H. P., Jackson, S. E., Fryer, B. J., & Strong, D. F. (1993). Machinations: The Laser Ablation Microprobe-Inductively Coupled Plasma-Mass Spectrometer. Geoscience Canada.

129. Mabuchi, H., Hirao, Y., Nishida, M. (1985). Lead isotope approach to the understanding of early Japanese bronze culture. Archaeometry, 27(2), 131–159.

130. Macfarlane, A. W., & Petersen, U. (1990). Pb isotopes of the Hualgayoc area, northern Peru; implications for metal provenance and genesis of a Cordilleran polymetallic mining district. Economic Geology, 85(7), 1303–1327.

131. MacNamara, J., & Thode, H. G. (1950). Comparison of the isotopic constitution of terrestrial and meteoritic sulfur. Physical Review, 78(3), 307.

132. Maruyama, S., Isozaki, Y., Kimura, G., & Terabayashi, M. (1997). Paleogeographic maps of the Japanese Islands: Plate tectonic synthesis from 750 Ma to the present. Island arc, 6(1), 121–142.

133. Meinert, L. D. (1992). Skarns and skarn deposits. Geoscience Canada, 19(4).

134. Mondillo, N., Arfè, G., Boni, M., Balassone, G., Boyce, A., Joachimski, M., ... & Villa, I. M. (2018). The Cristal Zinc prospect (Amazonas region, northern Peru). Part I: New insights on the sulfide mineralization in the Bongará province. Ore geology reviews, 94, 261–276.

135. Mondillo, N., Boni, M., Balassone, G., & Villa, I. M. (2014). The Yanque prospect (Peru): From polymetallic Zn-Pb mineralization to a nonsulfide deposit. Economic Geology, 109(6), 1735–1762.

136. Monster, J., Anders, E., & Thode, H. G. (1965). $^{34}S/^{32}S$ ratios for the different forms of sulphur in the Orgueil meteorite and their mode of formation. Geochimica et Cosmochimica Acta, 29(7), 773–779.

137. Morris, H. T., Cox, D. P. (1986). Descriptive model of polymetallic replacement deposits. Mineral deposit models: US Geological Survey Bulletin, 1693, 99–100.

138. Mudd, G. M., Jowitt, S. M., & Werner, T. T. (2017). The world's lead-zinc mineral resources: scarcity, data, issues and opportunities. Ore Geology Reviews, 80, 1160–1190.

139. Nielsen, H., Pilot, J., Grinenko, L. N., Grinenko, V. A., Lein, A. Y., Smith, J. W., & Pankina, R. G. (1991). Lithospheric sources of sulphur. In Stable isotopes: natural and anthropogenic sulphur in the environment.

140. Nier, A. O. (1938). Variations in the relative abundances of the isotopes of common lead from various sources. Journal of the American Chemical Society, 60(7), 1571–1576.

141. Nier, A. O., Thompson, R. W., & Murphey, B. F. (1941). The isotopic constitution of lead and the measurement of geological time. III. Physical Review, 60(2), 112–116.

142. Oh, C.W., Kim, C.S., Park, Y. (1997). The contact metamorphism due to the intrusion of the Ogcheon and Boeun granites. Journal of Petrological Society of Korea 6, 133–149. (in Korean with English Abstract).

143. Ohmoto, H. (1979). Isotopes of sulfur and carbon. Geochemistry of hydrothermal ore deposits, 509–567.

144. Ohmoto, H., & Goldhaber, M. B. (1997). Sulfur and carbon isotopes. 517–612 in: Geochemistry of Hydrothermal Ore Deposits 3rd edition (HL Barnes, editor).

145. Ohmoto, H., & Lasaga, A. C. (1982). Kinetics of reactions between aqueous sulfates and sulfides in hydrothermal systems. Geochimica et Cosmochimica Acta, 46(10), 1727–1745.

146. O'Neil, J. R. (1986). Theoretical and experimental aspects of isotopic fractionation. Reviews in Mineralogy, 16, 1–40.

147. O'Neil, J. R., Clayton, R. N., & Mayeda, T. K. (1969). Oxygen isotope fractionation in divalent metal carbonates. The Journal of Chemical Physics, 51(12), 5547–5558.

148. Ono, S., Eigenbrode, J. L., Pavlov, A. A., Kharecha, P., Rumble III, D., Kasting, J. F., & Freeman, K. H. (2003). New insights into Archean sulfur cycle from mass-independent sulfur isotope records from the Hamersley Basin, Australia. Earth and Planetary Science Letters, 213(1–2), 15–30.

149. Orr, W. L. (1974). Changes in sulfur content and isotopic ratios of sulfur during petroleum maturation--study of Big Horn basin Paleozoic oils. AAPG bulletin, 58(11), 2295–2318.

150. Paik, I. S., Chun, J.H. (1993). Laminar calcretes, calcerte pisoids and ooids, and rhizoliths from the Kyeongsang Supergroup, Korea. J. Geol. Soc. Korea, 29, 108–117 in Korean with English abstract.

151. Park, H. I., Chang, H. W., & Jin, M. S. (1988). K-Ar ages of mineral deposits in the Taebaeg Mountain district. Economic and Environmental Geology, 21(1), 57–67.

152. Park, H. I., Park, Y. R. (1990). Gold and silver mineralization in the Dongweon mine. Economic and Environmental Geology, 23(2), 183–199.

153. Park, K. H., & Chang, H. W. (2005). Pb isotopic composition of Yeonhwa and Janggun Pb-Zn ore deposits and origin of Pb: role of Precambrian crustal basement and Mesozoic igneous rocks. The Journal of the Petrological Society of Korea, 14(3), 141–148.

154. Pavlov, A. A., & Kasting, J. F. (2002). Mass-independent fractionation of sulfur isotopes in Archean sediments: strong evidence for an anoxic Archean atmosphere. Astrobiology, 2(1), 27–41.

155. Peruana, A. (2005). A Re–Evaluation of the Geology and Mineralization of the Charlotte Bongará Zinc Project, Amazonas. northern Peru: technical report. Anglo Peruana Terra SA (former Consultora Minera Anglo Peruana SA), Lima, Peru.

156. Pirajno F. (1992) Hydrothermal mineral deposits. Springer, Berlin, Heidelberg: 709.

157. Postgate, J. R. (1984). The sulphate-reducing bacteria 2nd Edn. Cambridge U. Press, London.

158. Price, F. T., & Shieh, Y. N. (1979). The distribution and isotopic composition of sulfur in coals from the Illinois Basin. Economic Geology, 74(6), 1445–1461.

159. Ramdohr, P. (1924). Beobachtungen an opaken Erzen. Arch. f. Lagerst, 34, 30.

160. Ramdohr, P. (1969). The Ore Minerals and Their Intergrowths. Pergamon, Oxford. 1174.

161. Reedman A.J., Kim D.H. (1997) Korea: South Korea. In: Encyclopedia of European and Asian Regional Geology. Encyclopedia of Earth Science. Springer, Dordrecht

162. Reedman, A. J., Um, S. H. (1975). Geology of Korea. Korean Institute of Energy resource, Seoul. Korea. 139.

163. Reedman, A.J., Fletcher, C.J.N., Evans, R.B. et al. (1973) Geological, geophysical and geochemical investigations in the Hwanggangri area, Chungcheongbukdo, Geological and Mineral Institute of Korean Rep. on Geology and Mineral Exploration, 1(2), 1–119.

164. Reedman, A.J., Park, K.H. and Evans, J.A. (1989) The age of granitoid intrusions and related mineralisation in the Chisulryoung Mountain area, south-east Korea: constraints on the age of the Chisulryoung Volcanic Formation and Yucheon Group volcanism. J. Geol. Soc. Korea, 25(1), 51–8.

165. Rees, C. E., Jenkins, W. J., & Monster, J. (1978). The sulphur isotope geochemistry of ocean water sulphate. Geochim Cosmochim Acta, 42, 377–382.

166. Rehkämper, M., & Halliday, A. N. (1998). Accuracy and long-term reproducibility of lead isotopic measurements by multiple-collector inductively coupled plasma mass spectrometry using an external method for correction of mass discrimination. International Journal of Mass Spectrometry, 181(1–3), 123–133.

167. Rehkämper, M., & Mezger, K. (2000). Investigation of matrix effects for Pb isotope ratio measurements by multiple collector ICP-MS: verification and application of optimized analytical protocols. Journal of Analytical Atomic Spectrometry, 15(11), 1451–1460.

168. Reid, C. J. (2001). Stratigraphy and mineralization of the Bongara MVT zinc-lead district, northern Peru (Doctoral dissertation, National Library of Canada= Bibliothèque nationale du Canada).

169. Ripley, E. M., & Li, C. (2003). Sulfur isotope exchange and metal enrichment in the formation of magmatic Cu-Ni-(PGE) deposits. Economic Geology, 98(3), 635–641.

170. Robb, L. (2005). Introduction to ore-forming processes (Vol. 239). Oxford: Blackwell.

171. Rosholt, J. N., & Bartel, A. J. (1969). Uranium, thorium, and lead systematics in Granite Mountains, Wyoming. Earth and Planetary Science Letters, 7(2), 141–147.

172. Rumble, D. (2005). A mineralogical and geochemical record of atmospheric photochemistry. Am Mineral, 90, 918–930.

173. Rye, R. O. (2005). A review of the stable-isotope geochemistry of sulfate minerals in selected igneous environments and related hydrothermal systems. Chemical Geology, 215(1–4), 5–36.

174. Sakai, H. (1968). Isotopic properties of sulfur compounds in hydrothermal processes. Geochemical Journal, 2(1), 29–49.

175. Sakai, H. (1980). Experimental study of the rate and isotope effect in sulfate reduction by ferrous iron oxides and silicates under hydrothermal conditions.

176. Sakai, H., Des Marais, D. J., Ueda, A., & Moore, J. G. (1984). Concentrations and isotope ratios of carbon, nitrogen and sulfur in ocean-floor basalts. Geochimica et Cosmochimica Acta, 48(12), 2433–2441.

177. Sangster, D. F. (1968). Relative sulphur isotope abundances of ancient seas and strata-bound sulphide deposits. Proc. Geol. Assoc. Canada, 19, 79–91.

178. Savarino, J., Romero, A., Cole-Dai, J., Bekki, S., & Thiemens, M. H. (2003). UV induced mass-independent sulfur isotope fractionation in stratospheric volcanic sulfate. Geophysical Research Letters, 30(21).

179. Schneiderhöhn, H. (1922). Anleitung zur mikroskopischen Bestimmung und Untersuchung von Erzen und Aufbereitungsprodukten besonders im auffallenden Licht. Selbst-verlag der Gesellschaft deutscher metallhütten-und bergleute ev, 292.

180. Schoene, B. (2014). 4.10-U–Th–Pb Geochronology. Treatise on geochemistry, 4, 341–378.

181. Scientific, T. F. (2009). NEPTUNE Hardware Manual.

182. Seal, R. R. (2003). Stable-isotope geochemistry of mine waters and related solids. Environmental aspects of mine wastes, 31, 303–334.

183. Seal, R. R. (2006). Sulfur isotope geochemistry of sulfide minerals. Rev. Mineral. Geochem, 61(1), 633–677.

184. Seal, R. R., & Wandless, G. A. (2003). Sulfur isotope evidence for seafloor mineralizing processes at the Bald Mountain and Mount Chase massive sulfide deposits, northern Maine. Economic Geology Monograph, 11, 567–587.

185. Seal, R. R., Alpers, C. N., & Rye, R. O. (2000). Stable isotope systematics of sulfate minerals. Reviews in Mineralogy and Geochemistry, 40(1), 541–602.

186. Shanks III, W. C., Bischoff, J. L., & Rosenbauer, R. J. (1981). Seawater sulfate reduction and sulfur isotope fractionation in basaltic systems: interaction of seawater with fayalite and magnetite at 200–350C. Geochimica et Cosmochimica Acta, 45(11), 1977–1995.

187. Shearer, C. K., Layne, G. D., Papike, J. J., & Spilde, M. N. (1996). Sulfur isotopic systematics in alteration assemblages in martian meteorite Allan Hills 84001. Geochimica et Cosmochimica Acta, 60(15), 2921–2926.

188. Sillitoe, R. H. (2010). Porphyry copper systems. Economic geology, 105(1), 3–41.

189. Sillitoe, R. H., Bonham Jr, H. F. (1990). Sediment-hosted gold deposits: Distal products of magmatic-hydrothermal systems. Geology, 18(2), 157–161.

190. Simmons, S. F., White, N. C., & John, D. A. (2005). Geological characteristics of epithermal precious and base metal deposits. Economic Geology, 100, 485–522.

191. Sinclair, R. J. (2009). The extractive metallurgy of lead. AusIMM.

192. Smith, J. W., & Batts, B. D. (1974). The distribution and isotopic composition of sulfur in coal. Geochimica et cosmochimica acta, 38(1), 121–133.

193. So, C. S., Yun, S. T., Chi, S. J., Koh, Y. K., & Choi, S. H. (1991). Cretaceous Epithermal Au-Ag Mineralization in the Muju-Yeongam District (Jeongju Mineralized Area), Republic of Korea: Geologic, Mineralogic, and Fluid Inclusion Studies. Korea. J. Geol. Soc. Korea, 27(5), 451–470.

194. Stacey, J. S., & Kramers, J. D. (1975). Approximation of terrestrial lead isotope evolution by a twostage model. Earth Planet Sc Lett 26: 207–221.

195. Stacey, J. S., Moore, W. J., & Rubright, R. D. (1967). Precision measurement of lead isotopes ratios: preliminary analyses from the US mine, Bingham Canyon, Utah. Earth and Planetary Science Letters, 2(5), 489–499.

196. Strauss, H. (1997). The isotopic composition of sedimentary sulfur through time. Palaeogeography, Palaeoclimatology, Palaeoecology, 132(1-4), 97–118.

197. Sugaki, A., Kitakaze, A., Kojima, S. (1987). Bulk compositions of intimate intergrowths of chalcopyrite and sphalerite and their genetic implications. Miner. Deposita, 22(1), 26–32.

198. Taylor, B. E., & Wheeler, M. C. (1994). Sulfur-and oxygen-isotope geochemistry of acid mine drainage in the western United States: field and experimental studies revisited.

199. Thode, H. G., Monster, J., & Dunford, H. B. (1961). Sulphur isotope geochemistry. Geochimica et Cosmochimica Acta, 25(3), 159–174.

200. Tomita, T. (1967) Volcanic geology of the Cenozoic alkaline petrographic province of eastern Asia. Geology and Mineral Resources of the Far East (ed. T. Ogura), 1, pp. 139–202.

201. Totsuka, S., Shimada, K., Nozaki, T., Kimura, J. I., Chang, Q., & Ishibashi, J. I. (2019). Pb isotope compositions of galena in hydrothermal deposits obtained by drillings from active hydrothermal fields in the middle Okinawa Trough determined by LA-MC-ICP-MS. Chemical Geology, 514, 90–104.

202. UNEP, 2013. In: Reuter, M.A., Hudson, C., van Schaik, A., Heiskanen, K., Meskers, C., Hagelüken, C. (Eds.), Metal Recycling: Opportunities, Limits, Infrastructure - A Report of the Working Group on the Global Metal Flows to the International Resource Panel. International Resource Panel (IRP), United Nations Environment Programme (UNEP), Paris, France.

203. Urey, H. C. (1947). The thermodynamic properties of isotopic substances. Journal of the Chemical Society (Resumed), 562–581.

204. Villa, I. M. (2009). Lead isotopic measurements in archeological objects. Archaeological and Anthropological Sciences, 1(3), 149.

205. Villa, I. M., Ruggieri, G., Puxeddu, M., & Bertini, G. (2006). Geochronology and isotope transport systematics in a subsurface granite from the Larderello–Travale geothermal system (Italy). Journal of Volcanology and Geothermal Research, 152(1–2), 20–50.

206. Villa, I.M. (2001). Radiogenic isotopes in fluid inclusions. Lithos, 55(1–4), 115–124.

207. Wasserburg, G. J. (1963). Diffusion processes in lead-uranium systems. Journal of Geophysical Research, 68(16), 4823–4846.

208. Weis, P., Driesner, T., & Heinrich, C. A. (2012). Porphyry-copper ore shells form at stable pressure-temperature fronts within dynamic fluid plumes. Science, 338(6114), 1613–1616.

209. Wetherill, G. W. (1956). Discordant uranium-lead ages, I. Eos, Transactions American Geophysical Union, 37(3), 320–326.

210. Wetherill, G. W. (1963). Discordant uranium-lead ages: 2. Disordant ages resulting from diffusion of lead and uranium. Journal of Geophysical Research, 68(10), 2957–2965.

211. White, W. M., Albarède, F., & Télouk, P. (2000). High-precision analysis of Pb isotope ratios by multi-collector ICP-MS. Chemical Geology, 167(3–4), 257–270.

212. Wiggins, L.B., Craig, J.R. (1980). Reconnaissance of the Cu-Fe-Zn-S system; sphalerite phase relationships. Econ. Geol., 75(5), 742–751.

213. Woo, K.S., Lee, K.C., Paik, K.H. (1991. Cretaceous lacustrine radial ooids in the Kyongsang Basin, Korea: paleoclimatic implications. J. Geol. Soc. Korea 27, 171–176.

214. Yang, S.Y. (1982). On the dinosaur's footprints from the Upper Cretaceous Gyeongsang Group, Korea. J. Geol. Soc. Korea 18, 138–142.

215. Yoo, B.C. (2012). Element dispersion by the wallrock alteration of Janggun Lead-Zinc-Silver deposit. Econ. Environ. Geol. 45 (6), 623–641.

216. Zientek, M. I., & Ripley, E. M. (1990). Sulfur isotope studies of the Stillwater Complex and associated rocks, Montana. Economic Geology, 85(2), 376–391.